STARS

University of Central Florida
STARS

Electronic Theses and Dissertations, 2004-2019

2005

Uv-liga Compatible Electroformed Nano-structured Materials For Micro Mechanical Systems

Bo Li
University of Central Florida

Part of the Mechanical Engineering Commons
Find similar works at: https://stars.library.ucf.edu/etd
University of Central Florida Libraries http://library.ucf.edu

This Doctoral Dissertation (Open Access) is brought to you for free and open access by STARS. It has been accepted for inclusion in Electronic Theses and Dissertations, 2004-2019 by an authorized administrator of STARS. For more information, please contact STARS@ucf.edu.

STARS Citation

Li, Bo, "Uv-liga Compatible Electroformed Nano-structured Materials For Micro Mechanical Systems" (2005). *Electronic Theses and Dissertations, 2004-2019*. 348.
https://stars.library.ucf.edu/etd/348

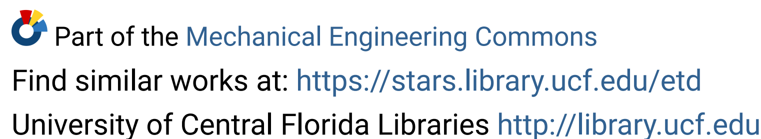

UV-LIGA COMPATIBLE ELECTROFORMED NANO-STRUCTURED MATERIALS FOR MICRO MECHANICAL SYSTEMS

by

BO LI

B.S. Beijing Institute of Petrochemical Technology, 1995
M.S. Beijing University of Chemical Technology, 1998

A dissertation submitted in partial fulfillment of the requirements
for the degree of Doctor of Philosophy
in the Department of Mechanical, Materials and Aerospace Engineering
in the College of Engineering and Computer Science
at the University of Central Florida
Orlando, Florida

Spring Term
2005

Major Professor: Quanfang Chen

© 2005 Bo Li

ABSTRACT

UV-LIGA is a microfabrication process realzed by material deposition through microfabricated molds. UV photolithography is conducted to pattern precise thick micro molds using UV light sensitive materials, mostly SU-8, and electroforming is performed to fabricate micro metallic structures defined by the micro molds. Therefore, UV-LIGA is a bottom-up in situ material-addition process. UV-LIGA has received broad attention recently than LIGA – a micro molding fabrication process using X-ray to pattern the micro molds. LIGA is an expansive and is limited in access. In comparing to LIGA, the UV-LIGA is a cost effective process, and is widely accessible and safe. Therefore, it has been extensively used for the fabrication of metallic micro-electro-mechanical-systems (MEMS). The motivation of this research was to study micro mechanical systems fabricated with nano-structured metallic materials via UV-LIGA process. Various micro mechanical systems with high-aspect-ratio and thick metallic structures have been developed and are presented in this desertation.

A novel micro mechanical valve has been developed with nano-structured nickel realized with UV-LIGA fabrication technique. Robust compact valves are crucial for space applications where payload and rubstaness are critically concerned. Two types of large flow rate robust passive micro check valve arrays have been designed, fabricated and tested for robust hydraulic actuators.

The first such micro valve developed employs nanostructured nickel as the valve flap and single-crystal silicon as the substrates to house inlet and outlet channels. The Nano-structured

nickel valve flap was fabricated using the UV-LIGA process developed and the microchannels were fabricated by deep reactive etching (DRIE) method. The valves were designed to operate under a high pressure (>10MPa), able to operate at high frequencies (>10kHz) in cooperating with the PZT actuator to produce large flow rates (>10 cc/s). The fabricated microvalves weigh 0.2 gram, after packing with a novel designated valve stopper. The tested results showed that the micro valve was able to operate at up to 14kHz. This is a great difference in comparison to traditional mechanical valves whose operations are limited to 500 Hz or less. The advantages of micro machined valves attribute to the scaling laws.

The second type of micro mechanical valves developed is a in situ assembled solid metallic (nickel) valves. Both the valve substrates for inlet and outlet channels and the valve flap, as well as the valve stopper were made by nickel through a UV-LIGA fabrication process developed. Continuous multiple micro molds fabrication and molding processes were performed. Final micro mechanical valves were received after removing the micro molds used to define the strutures. There is no any additional machining process, such as cutting or packaging. The alignment for laminated fabrication was realized under microscope, therefore it is a highly precise in situ fabrication process. Testing results show the valve has a forward flow rate of19 cc/s under a pressure difference of 90 psi. The backward flow rate of 0.023 cc/s, which is negligible (0.13%).

Nano-structured nickel has also been used to develop laminated (sandwiched) micro cryogenic heater exchanger with the UV-LIGA process. Even though nickel is apparently not a good thermal conductor at room temperature, it is a good conductor at cryogentic temerpature since its thermal conductivity increases to 1250 W/k·m at 77K. Micro patterned

SU-8 molds and electroformed nickel have been developed to realize the sandwiched heat exchanger. The SU-8 mold (200μm x 200μm x50μm) array was successfully removed after completing the nickel electroforming. The second layer of patterned SU-8 layer (200μm x 200μm x50μm, as a thermal insulating layer) was patterned and aligned on the top of the electroformed nickel structure to form the laminated (sandwiched) micro heat exchanger. The fabricated sandwiched structure can withstand cryogenic temperature (77K) without any damages (cracks or delaminations).

A study on nanocomposite for micro mechanical systems using UV-LIGA compatible electroforming process has been performed. Single-walled carbon nanotubes (SWNTs) have been proven excellent mechanical properties and thermal conductive properties, such as high strength and elastic modulus, negative coefficient of thermal expansion (CTE) and a high thermal conductivity. These properties make SWNT an excellent reinforcement in nanocomposite for various applications. However, there has been a challenge of utilizing SWNTs for engineering applications due to difficulties in quality control and handling – too small (1-2nm in diameter). A novel copper/SWNT nanocomposite has been developed during this dissertational research. The goal of this research was to develop a heat spreader for high power electronics (HPE). Semiconductors for HPE, such as AlGaN/GaN high electron mobility transistors grown on SiC dies have a typical CTE about $4\sim6\text{x}10^{-6}$/k while most metallic heat spreaders such as copper have a CTE of more than $10\text{x}10^{-6}$/k. The SWNTs were successfully dispersed in the copper matrix to form the SWNT/Cu nano composite. The tested composite density is about 7.54 g/cm^3, which indicating the SWNT volumetric fraction of 18%. SEM pictures show copper univformly coated on SWNT (worm-shaped structure).

The measured CTE of the nanocomposite is 4.7 x 10^{-6}/°C, perfectly matching that of SiC die (3.8 x 10^{-6}/°C). The thermal conductivity derived by Wiedemann-Franz law after measuring composit's electrical conductivity, is 588 W/m-K, which is 40% better than that of pure copper. These properties are extremely important for the heat spreader/exchanger to remove the heat from HPE devices (SiC dies). Meanwhile, the matched CTE will reduce the resulted stress in the interface to prevent delaminations. Therefore, the naocomposite developed will be an excellent replacement material for the CuMo currently used in high power radar, and other HPE devices under developing.

The mechanical performance and reliability of micro mechanical devices are critical for their application. In order to validate the design & simulation results, a direct (tensile) test method was developed to test the mechanical properties of the materials involved in this research, including nickel and SU-8. Micro machined specimens were fabricated and tested on a MTS Tytron Micro Force Tester with specially designed gripers. The tested fracture strength of nanostructured nickel is 900±70 MPa and of 50MPa for SU-8, resepctively which are much higher than published values.

ACKNOWLEDGMENTS

I would like to express my sincere gratitude and thanks to Dr. Quanfang Chen for his academic and finical support through out this research work. I would also like to thank my committee members, Dr. Louis Chow, Dr. Lee Chow, Dr. David W. Nicholson and Dr. Quan Wang for their suggestions and assistance during the preparation of this thesis. A sincere appreciation goes to all the members of MEMS lab for their help and meaningful contribution to this thesis. Finally, I would like to thank my parents and my wife for their encouragement and support throughout my life and education.

TABLE OF CONTENTS

LIST OF FIGURES……………….………………………………….……..…...….. xii

LIST OF TABLES………………...…………………………………..………..… xxii

CHAPTER 1 INTRODUCTION………………………………………...………….. 1

1.1 Micro-electro-mechanical-systems (MEMS)…………….……………….…...….…. 1

1.2 Microfabrication Techniques…….………………………………………………….. 3

1.3 LIGA and UV-LIGA Process……………….……………...………………..... 10

1.4 Electrochemical Deposition Rate..……………….……………..………...….... 12

1.5 Principles Governing Electroforming Process…..……..……………………….……16

1.6 Scaling Laws in MEMS………………..……………………………….……21

1.7 Objectives of the Research……………………………………-……………… 26

CHAPTER 2 ELECTROFORMED ROBUST LARGE FLOW RATE PASSIVE HYBRID MICRO CHECK VALVES ……..…………….………….……. 29

2.1 Introduction ……………………………………………………….……….. 29

2.2 Microvalve Design……………………………………………….……… 32

2.3 Finite Element Analysis……………………………………….………… 38

2.4 Fabrication…………………….……………………………………….………. 45

2.5 Test Results and Discussion…………….……………… …………………... 50

2.6 Conclusion………………………….……………………………………….…. 53

CHAPTER 3 LOW STRESS SU-8 PROCESS AND ITS APPLICATION FOR FABRICATING A NOVEL MICRO HEAT EXCHANGER…………………..... 54

3.1 Introduction……………………...……………..………………………….... 54

3.2 Development of the SU-8 Process……………………………….… ………….. 55

3.3 Design of the Micro Heat Exchanger……………………….……… ………… 61

3.4 Fabrication…………………….………………………………………………… 63

3.5 Testing……………………………………………………….………………….. 67

3.6 Discussion and Conclusions…………………………………………………….. 68

CHAPTER 4 DEVELOPMENT OF IN SITU ASSEMBLED SOLID NICKEL MICROVALVES…………...…………………………………………....................... 70

4.1 Introduction………………………………………………………….……..…. 70

4.2 Valve Design……………………………………………………………….…. 71

4.3 Stress Analysis…………………….…………………………………………... 73

4.4 Fabrication Process………………….……….……………..………………… 78

4.5 Flow Rate Measurement……………………………….……………….……. 88

4.6 Conclusion……………………….………………..……………..…………. 91

CHAPTER 5 ELECTROFORMED COPPER/SWNT NANOCOMPOSITE………...... 93

5.1 Introduction……………………………………………………….………... 93

5.2 Motivation………………………………………………………….…..…. 100

5.3 Prediction of Copper/SWNT Properties……………………….…….……… 103

5.4 Fabrication…………………………………………………………….…… 107

5.5 Characterization………………………………………………………....…… 111

5.6 Conclusion…………………………………………………………...……. 123

CHAPTER 6 MICRO MECHANICAL TEST OF MICROFABRICATED MEMS MATERIALS …………..……………..……………………………….…. 126

6.1 Introduction…………………………………..…………………….…... 126

6.2 Literature Review…….……….………………………………………….……. 128

6.3 Methodology……………………..………………………………….……. 133

6.4 Specimen Design………………………………………………….……. 137

6.5 Specimen Fabrication……………………………………………….…….. 137

6.6 Testing Setup…………………………………………………….…...… 140

6.7 Mechanical Testing Results……………………………………..…...… 141

6.8 Conclusion ………………………………………………...………...….. 145

CHAPTER 7 CONCLUSIONS…………………………..……………….……. 146

REFERENCES………………………………………………………………...… 150

LIST OF FIGURES

Figure 1.1: An electrostatic driven micromotor……………………………..……….… 2

Figure 1.2: SEM view of an 80 μm thick, 2 mm in diameter, four-ring gyroscope with meander-shaped springs …………………………………………………..……..….… 3

Figure 1.3: Sketch of a photolithography and an etching process…….……….……….… 4

Figure 1.4: Typical hot-wall LPCVD reactor.……………………..……….……….… 6

Figure 1.5: Typical setup for electrochemical deposition..………………..…..……….… 8

Figure 1.6: Typical wafer oxidation furnace..……………………..………….……….… 9

Figure 1.7: Schematic drawing of the UV-LIGA process…………………….……..… 12

Figure 1.8: Nickel electrochemical deposition rate (calculated) ………………….….….… 15

Figure 1.9: Copper electrochemical deposition rate (calculated)………………….….….… 16

Figure 1.10: Schematic drawing of the pattern scale and feature scale current distribution on a patterned electrode…………………………………………………………...….. 19

Figure 1.11: Schematic drawing of the pulse scheme……….……………….……….. 21

Figure 1.12: Typical cantilever beam studied ……….……………….………...…….. 23

Figure 1.13 Squeeze film damping …….…………………….………………...…….. 25

Figure 2.1: Sketch of compact pump and integrated microvalves……………………..... 33

Figure 2.2: Details of individual microvalve of valve array…………………………….. 34

Figure 2.3: Scheme of flow rate calculation parameters………………………………… 36

Figure 2.4: Calculated flow rate of a single micro valve…………………...…………… 37

Figure 2.5: Calculated flow rate of 84 micro valves…………………………………….. 37

Figure 2.6: First mode natural frequency of the micro valve flap………….…………… 39

Figure 2.7. Stress distribution over microvalve flap while it is fully opened…………… 41

Figure 2.8: Stress distribution of microvalve under 10 MPa pressure while closed….…. 43

Figure 2.9: Supporting area of the valve & the silicon substrate……………………..….. 44

Figure 2.10: Stress distribution of silicon substrate under 10 MPa pressure while closed.. 44

Figure 2.11: Photoresist mold (thickness 12 μm) for the flap electroforming…………… 46

Figure 2.12: Fabrication process………………………………………..…………….. 47

Figure 2.13: Array of microvalves (84) over 6-mm radius area before bonding with valve stopper……………………………………………………………………..….. 48

Figure 2.14: Microvalve arrays (84) after bonding valve stopper (top view)…………… 48

Figure 2.15: Nanostructured electroformed nickel………………………….…………… 49

Figure 2.16: Forward and backward flow rates under pressure differences…………….. 51

Figure 2.17: Repeat tests of flow rate under pressure differences applied………………. 52

Figure 3.1: Distorted SU-8 pattern and cracks ………………………….……………. 56

Figure 3.2: SU-8 pattern partially peeled off …..……………………….……………. 56

Figure 3.3: A 250 μm thick SU-8 mold for a nickel mesh like structure with 2704 squares (200 μm by 200 μm) in an area of 1.7 cm^2……………………………………………… 60

Figure 3.4: Sketch of the micro heat exchanger……………………………………… 61

Figure 3.5: Stress distribution of the micro heat exchanger………………...…………… 63

Figure 3.6: Fabrication process flow for the micro heat exchanger…………………..…. 64

Figure 3.7: Top view of nickel thermal conductive layer with thickness of 300 µm….… 66

Figure 3.8: Top view of SU-8/Nickel sandwiched structure…………………………..…. 66

Figure 3.9: Top view of the tested sandwiched structure……………………….…….. 67

Figure 4.1: A broken silicon-nickel valve…………………………………….……… 70

Figure 4.2: Robust pump and solid nickel valve………………………………………… 72

Figure 4.3: Concept sketch of the valve flap (top view)…………………..………….. 73

Figure 4.4: Stress distribution over microvalve flap while it is fully opened………..….. 74

Figure 4.5: Comparing of maximum von misses stress between silicon-nickel valve and solid nickel valve when fully opened…………………………………………….………. 75

Figure 4.6: Stress distribution over microvalve flap while it is closed……………….…. 75

Figure 4.7: Comparing of maximum von misses stress between silicon-nickel valve and solid nickel valve when closed……………………………………………………….... 76

Figure 4.8: Stress distribution of nickel substrate under 10 MPa pressure while closed... 77

Figure 4.9: Comparing of maximum von misses stress in supporting substrate between silicon-nickel valve and solid nickel valve when closed………………………………… 77

Figure 4.10: Sketch of fabrication process step (A) & (B)……………..…………..….. 79

Figure 4.11: PR molds (12 μm thick) for valve flap and micro beams…….………………. 79

Figure 4.12: Sketch of fabrication process step (C) & (D). …………...………………... 81

Figure 4.13: SU-8 molds for inlet channels…………………...………………………… 81

Figure 4.14: Sketch of fabrication process step (E) & (F)…...…………….……………. 82

Figure 4.15: Sketch of fabrication process step (G) & (H)……………………………… 83

Figure 4.16: Fabricate microvalve array……………………………………………….. 83

Figure 4.17: Finished micro flap with total thickness of 25 μm………………………… 84

Figure 4.18: Sketch of fabrication process step (I) & (J)……………………….……….. 85

Figure 4.19: Sketch of fabrication process step (K) & (L)………………………………. 85

Figure 4.20: Final released structure…………………………………….…………..... 86

Figure 4.21: Finished nickel valve………………………………………………………. 86

Figure 4.22: SEM picture of valve inlet…………………………………………………. 87

Figure 4.23: SEM picture of valve outlet……………...……………………………… 87

Figure 4.24: Scheme of flow rate measurement system……………………………..…… 88

Figure 4.25:Tested flow rate versus pressure applied of the microvalve…………...…… 89

Figure 4.26: Repeated test of forward flow rate under loading/unloading conditions…. 90

Figure 5.1: Graphene sheet illustrating chiral arrangements……………………………. 96

Figure 5.2: Armchair, Zigzag and Chiral Nanotubes……………………………………. 96

Figure 5.3: Temperature dependence of the thermal conductivity for a (10,10) carbon nanotube for temperatures below 400 K…………………………………….…………... 98

Figure 5.4: CTE of carbon nanotubes……………………………………...………. 99

Figure 5.5: Concept scheme of the heat management structure for transistor……….... 101

Figure 5.6: CTE estimation for copper/SWNT v.s. SWNT's volume fraction……...….. 104

Figure 5.7: Thermal conductivity estimation for copper/SWNT v.s. SWNT's volume fraction…………………………………………………...……………….. 105

Figure 5.8:Temperature gradient in SiC and Cu/CNT composite………..…………..… 106

Figure 5.9: Stresses in SiC and Cu/CNT composite……………………..……….….... 106

Figure 5.10: Concept scheme of electroforming for the copper/SWNT composite……. 107

Figure 5.11: SEM picture of the as-purchased purified SWNT soot………...……..… 108

Figure 5.12: SEM picture of the as-purchased purified SWNT soot dissolved by acetone 109

Figure 5.13: SWNT (1g/L) dispersed in copper bath……………………….………. 110

Figure 5.14: SEM picture of the composite surface, magnified by 1000 times..………. 112

Figure 5.15: SEM picture of the composite surface, magnified by 5000 times…..……. 113

Figure 5.16: SEM picture of the composite surface, magnified by 10000 times..…….. 113

Figure 5.17: SEM picture of the pure copper surface, magnified by 3000 times..…….. 114

Figure 5.18: Energy dispersive Spectroscopy (EDS) of the composite……….……… 114

Figure 5.19: SEM picture of the polished composite surface……………………..…… 115

Figure 5.20: Polished composite sample………………………………..…………… 115

Figure 5.21: TMA thermomechanical system……………………………..……… 117

Figure 5.22: Measured CTE of copper/SWNT composite……………………..……. 118

Figure 5.23: 4-point probe configuration………..……………………………..……. 119

Figure 5.24: Electrical conductivity of composite and copper………………...…….. 121

Figure 5.25: Thermal conductivity of composite and copper…………………….…. 123

Figure 5.26: SWNT aggregate in the composite…………………………..……… 125

Figure 6.1: One-end-fixing tensile test (ping on the left, and ring on the right)……..… 129

Figure 6.2: Out-of-plane bending test by a stylus …………………………….….… 130

Figure 6.3: Schematic diagram of a membrane test…………………………...…..… 131

Figure 6.4: Schematic diagram of a resonant test ……………………..……...…..… 132

Figure 6.5:Raman spectrum of stress-free single-crystal silicon………………………. 134

Figure 6.6: Specimen holder and testing specimens with width of 90 μm, 40 μm and 90 μm respectively.……………………………………………………………………..… 138

Figure 6.7: FEA simulation results of deformation……………………………….…. 138

Figure 6.8: SU-8 mold with thickness 75 μm for the fabrication of the testing specimens 139

Figure 6.9: SU-8 specimen with thickness 75 μm………..…………………………… 139

Figure 6.10: SEM picture of nickel specimen…….……………………………………… 140

Figure 6.11: Testing system…………………………………..……………………... 141

Figure 6.12: Electroformed nickel mechanical testing results……..……...……..…….. 142

Figure 6.13: SEM picture of the fracture section of nickel specimen………..………… 143

Figure 6.14: SU-8 mechanical testing results ……………………………..………… 144

Figure 6.15: SU-8 fracture section ……………………………………...………… 144

LIST OF TABLES

Table 3.1: Properties used for heat exchanger simulation…………………………..……. 62

Table 4.1: Operating conditions for electrochemical deposition schemes

(nickel sulfamate solution)……………………………………………………………. 80

Table 5.1: Thermal properties of SiC, CuMo and Sn-3.5Ag……………………..……. 102

Table 5.2: Properties of single-walled carbon nanotube and pure copper…………..…. 104

Table 5.3:Bulk acid copper electrolyte recipe………………………..……………… 108

Table 5.4: Electroforming conditions for the composite……………………..……… 111

Table 5.5: Density measurement of composite samples……………………..……...… 116

Table 5.6: Resistivity measurement of the composite sample……………………..…... 120

Table 5.7: Resistivity measurement of electroplated pure copper sample…………..…. 120

CHAPTER 1 INTRODUCTION

1.1 Micro-electro-mechanical-systems (MEMS)

Micro-electro-mechanical-systems (MEMS) refer to the devices that have a characteristic length of less than 1mm but more than 1μm. MEMS devices normally combine electrical and mechanical components and are mostly fabricated using integrated circuit compatible batch-processing technologies – microfabrcition process. The applications of MEMS are broadly found in aerospace, aeronautics, military, civil engineering, biomedics, automotive industry and so on [1]. In the early age of MEMS development, researches used materials and processes of microelectronics to build microscopic mechanical devices consisting of beams, pits, gears, membranes and even motors that can be deployed to move atoms or to open and close valves. The size of these mechanical elements is measured in microns, and like transistors, millions of them can be fabricated together in a single process. These devices can be classified into two categories: actuators and sensors, partial of which are listed below

Accelerometers	Micromotors
Actuators	Micropumps
Biomedical devices	Microvalves
Flowmeters	Optical devices/mirrors
Gas detectors	Resonators
Gyroscopes	Sensors
Magnetic devices	Spectrometers
Membranes	Strain gauges

Micromachines

That of the sensors is a particularly flourish field, comprising between the others:

Chemical sensors	Image sensors
Inertial sensors	Pressure sensors
Stress sensors	Thermal sensors
Tunneling sensors	Tilt sensors

Figure 1.1 shows an electrostatic driven micromotor. Figure 1.2 shows a MEMS-based electrostatic polysilicon gyroscope.

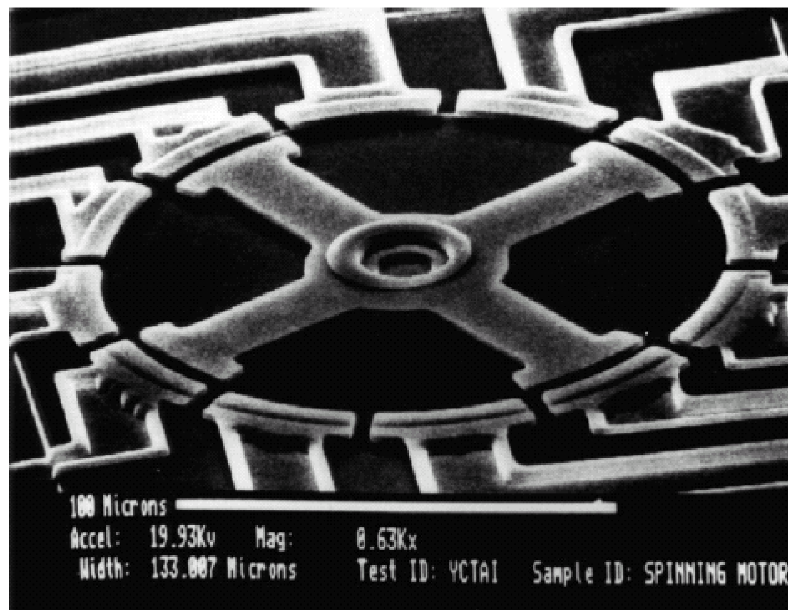

Figure 1.1: An electrostatic driven micromotor [1]

The major advantages of MEMS include: high performance (due to scaling laws and precise fabrication), low manufacturing cost (batch fabrication), low power consumption, portability,

easy maintenance and replacement, and environmental friendliness. The overall MEMS market is expected to triple, from $3.8 billion to more $11 billion, between 2000 and 2005, according to a report from Peripheral Research Corp.

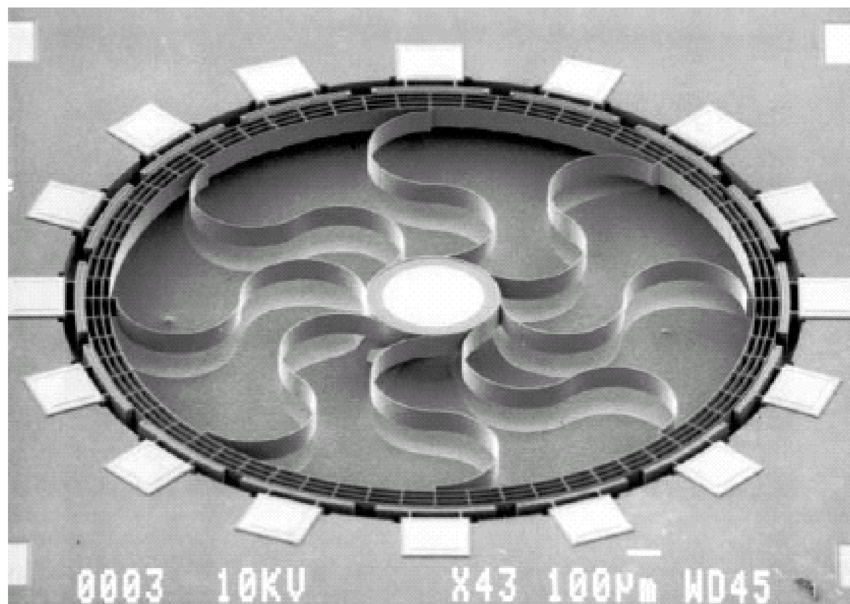

Figure 1.2: SEM view of an 80 μm thick, 2 mm in diameter, four-ring gyroscope with meander-shaped springs [1]

1.2 Microfabrication Techniques

Micro-fabrication techniques can be classified into two groups: material subtractive techniques and material additive techniques. The material subtractive techniques include dry etching and wet etching. The additive techniques include physical vapor deposition, chemical vapor deposition, electro deposition, epitaxy and thermal oxidation. Both of the two group techniques need photo lithographically defined patterns to serve as etching masks or molds.

In the MEMS fabrication, lithography is typically the transfer of a pattern to a photosensitive material by selective exposure to a radiation source such as UV light or x-Ray. A photosensitive material (e.g. photoresist) is a material that experiences a change in its physical or chemical properties when exposed to a radiation source. Usually, there are two groups of photosensitive materials, one is positive photoresist and the other is negative photoresist. As for positive material, the unexposed potion will stay after developing. The negative material is the reverse. If we selectively expose a photosensitive material to radiation (e.g. by masking some of the radiation), the pattern of the radiation on the mask is transferred to the material exposed, as the properties of the exposed and unexposed regions differ (Figure 1.3)[1].

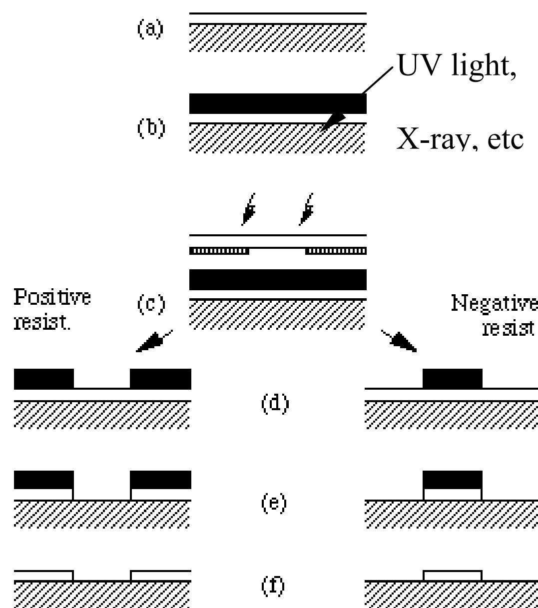

Figure 1.3: Sketch of a photolithography and an etching process. (a) deposition of target material, (b) photoresist coating, (c) UV light expose (d) developing photoresist, (e) etching, (f) stripping of photoresist

The subtractive process (e.g. etching) is employed to remove materials defined by the etching masks (e.g. patterned photoresist) to achieve the desired patterns. Generally speaking, there are two kinds of etching techniques, dry etching and wet etching. Dry etching is such a technique that a solid surface is etched by a gas or vapor, physically by ion bombardment, chemically by reactive species, or by a combination of physical and chemical mechanisms. Typically, dry etching needs to be performed in a vacuum chamber and usually plasma or an ion beam is needed to assist the etching process [1]. Wet etching employs a pool of liquids containing specific etchants to remove materials. These etching techniques are specifically designed for thin films and silicon materials. Thick metal films are difficult to etch and undercuts will occur.

The additive process is used to deposit films of materials (either thin or thick), which usually involves a chemical or physical reaction. The chemical vapor deposition, electro deposition, epitaxy and thermal oxidation are chemical processes, while the physical vapor deposition is a physical process.

Chemical Vapor Deposition (CVD) is excellent in good step coverage, and various materials can be deposited with this technology. However, some of them are less popular because of hazardous byproducts formed during processing. The quality of the materials deposited varies from process to process, however a good rule of thumb is that higher process temperature yields a material with higher quality and less defects. In this process, the substrate is placed inside a reactor to which a number of gases are supplied. The fundamental principle of the process is that a chemical reaction takes place between the source gases. The product of that

reaction is a solid material which condenses on all surfaces inside the reactor. The two most important CVD technologies in MEMS are the Low Pressure CVD (LPCVD) and Plasma Enhanced CVD (PECVD). The LPCVD process produces layers with excellent uniformity of thickness and material characteristics. The main problems with the process are the high deposition temperature (higher than 600° C) and the relatively slow deposition rate. The PECVD process can operate at lower temperatures (down to 300° C) thanks to the extra energy supplied to the gas molecules by the plasma in the reactor. However, the quality of the films tends to be inferior to processes running at higher temperatures. Secondly, most PECVD deposition systems can only deposit the material on one side of the wafers on 1 to 4 wafers at a time. LPCVD systems deposit films on both sides of at least 25 wafers a time. A schematic diagram of a typical LPCVD reactor is shown in the Figure1.4 below.

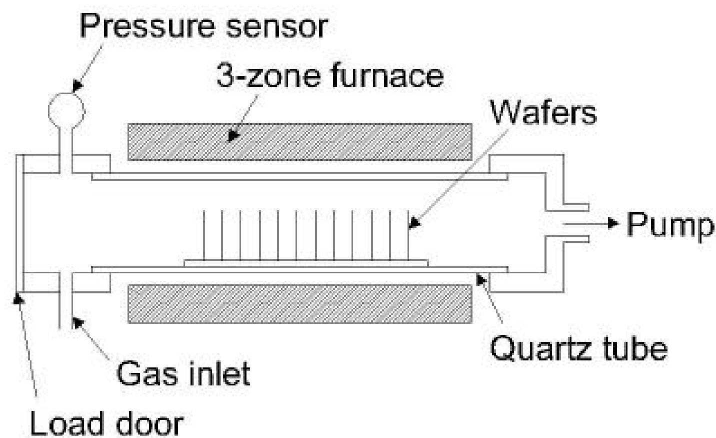

Figure 1.4: Typical hot-wall LPCVD reactor.

Electrochemical deposition is suitable to make films of metals such as copper, gold and nickel. The films can be made in any thickness from ~1μm to 1 cm. The deposition is best

controlled when used with an external electrical potential, however, it requires electrical contacts to the substrate when immersed in the liquid bath. In any process, the surface of the substrate must have an electrically conducting coating before the deposition starts. And a lapping process is usually involved after deposition. There are basically two technologies for electrodeposition: electroplating and electroless plating. In the electroplating process the substrate is placed in a liquid solution (electrolyte). When an electrical potential is applied between a conducting area on the substrate and a counter electrode in the liquid, a chemical redox process takes place resulting in the formation of a layer of material on the substrate and usually some gas generation at the counter electrode. In the electroless plating process a more complex chemical solution is used, where deposition happens spontaneously on any surface. This process is desirable since it does not require any external electrical potential and contact to the substrate during processing. Unfortunately, it is also more difficult to control with regards to film thickness and uniformity. A schematic diagram of a typical setup for electroplating is shown in the Figure 1.5.

Epitaxy is a technique to grow single crystals on the substrate and quite similar to CVD process. This process can be used to form films of silicon with thickness of ~1µm to >100µm. Some processes require high temperature of the substrate, whereas others do not require significant heating of the substrate. Some processes can even be used to perform selective deposition, depending on the surface of the substrate.

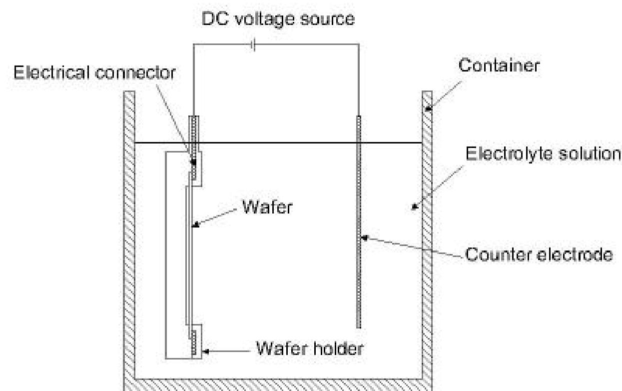

Figure 1.5: Typical setup for electrochemical deposition

Thermal oxidation is used to oxidize of the surface of the substrate in an oxygen rich atmosphere. The temperature is raised to 800° C-1100°C to speed up the process. The growth of the film is spurned by diffusion of oxygen into the substrate, which means the film growth is actually downwards into the substrate. As the thickness of the oxidized layer increases, the diffusion of oxygen to the substrate becomes more difficult leading to a parabolic relationship between film thickness and oxidation time for films thicker than ~100nm. This process is naturally limited to materials that can be oxidized, and it can only form films that are oxides of that material. This is the classical process used to form silicon dioxide on a silicon substrate. A schematic diagram of a typical wafer oxidation furnace is shown in the Figure 1.6 below.

Physical Vapor Deposition (PVD) covers a number of deposition technologies in which material is released from a source and transferred to the substrate. The two most important

technologies are evaporation and sputtering. In evaporation, the substrate is placed inside a vacuum chamber, where a block (source) of the material to be deposited is also located. The source material is then heated to the point where it starts to boil and evaporate. The vacuum is required to allow the molecules to evaporate freely in the chamber, and they subsequently condense on all surfaces. There are two popular evaporation technologies, which are e-beam evaporation and resistive evaporation each referring to the heating method. In e-beam evaporation, an electron beam is aimed at the source material causing local heating and evaporation. In resistive evaporation, a tungsten boat, containing the source material, is heated electrically with a high current to make the material evaporate. Sputtering is a technology in which the material is released from the source at much lower temperature than evaporation. The substrate is placed in a vacuum chamber with the source material, named a target, and an inert gas (such as argon) is introduced at low pressure. Gas plasma is struck using a DC or RF power source, causing the gas to become ionized. The ions are accelerated towards the surface of the target, causing atoms of the source material to break off from the target in vapor form and condense on all surfaces including the substrate. As for evaporation, the basic principle of sputtering is the same for all sputtering technologies.

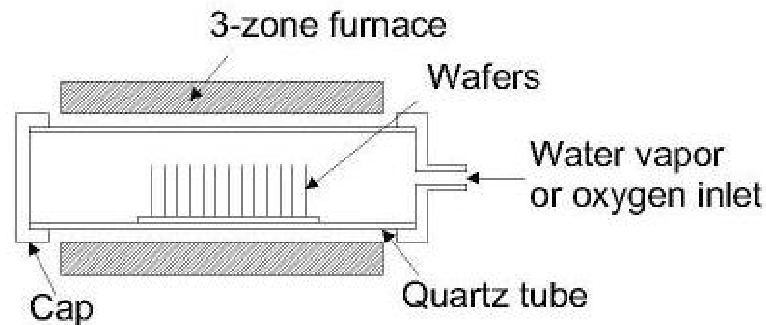

Figure 1.6: Typical wafer oxidation furnace.

1.3 LIGA and UV-LIGA Process

A new technique, named micro molding can be employed to fabricate high-aspect-ratio MEMS structures, where thick metal layers are needed. This technique requires the development of a thick mold, and metal is inserted to the mold by using the electroforming technique. The well-known molding technique for MEMS fabrication is known as LIGA [1,2], which was developed first in Germany and stands for the German "Lithography, Galvanoformung und Abformung". The first two words are the German equivalent of electro-plating-through-lithography masks and the world "Abformung" represents for LIGA standing for injection molding. LIGA is a through mask plating process using thick molds (PMMA) for high aspect ratio features, which are originally patterned by X-Ray lithography. The cost of LIGA process is high because it uses X-Ray (and therefore needs gold masks) to pattern the molds.

A newly developed micro molding technique, namely UV-LIGA [9], which uses a thick photoresist (for example SU-8) as the material for micro molds patterned by the conventional photolithography (UV light), is increasingly used for fabricating high aspect ratio MEMS structures. This process is easy to access and relatively cost-effectiveness in that it only needs simple equipment including conventional UV aligner, electrochemical cell and power supply, etc. The electrochemical deposition used in this process has a better throwing power than physical vapor deposition (PVD), which allows the production of high aspect ratioes and three dimensional structures with better precision. It is also attractive in the environmental point of view, because the waste is minimized due to the selectivity of material deposition and removal.

Subsequently, metal is electrochemically formed into the molds. Upon removal of the molds, the MEMS structures are finished. Movable three-dimensional microstructures with high aspect ratioes can be obtained by combining the UV-LIGA process with the sacrificial layer techniques.

The UV-LIGA process involves a thick layer of resist (from tens of microns to millimeters) as the molds, which can be exposed by UV light using the conventional mask aligner. Nickel (or copper) is usually used based on its mechanical strength, corrosion resistance, thermal/electrical conductivity and ease of electroplating. This process is capable of making three-dimensional features, while only two-dimensional structures can be made by the conventional surface micromachining techniques such as etching and physical vapor deposition.

Typically, the process begins with the deposition of the metallic seed layer by using the physical vapor deposition process such as thermal evaporation, sputtering or e-beam evaporation, followed by patterning of the molds by the photolithography process. Then metals are filled into the molds by electroforming, and the molds are removed after electroforming. The process flow is shown in Figure 1.7. UV-LIGA process gives the opportunity to fabricate robust MEMS devices with low cost, improved performance and reliability [3]. The UV-LIGA (electroforming) technique is also employed to fabricate composite materials. Electrochemical co-deposition of particles with metals is an effective way to make innovative composite materials.

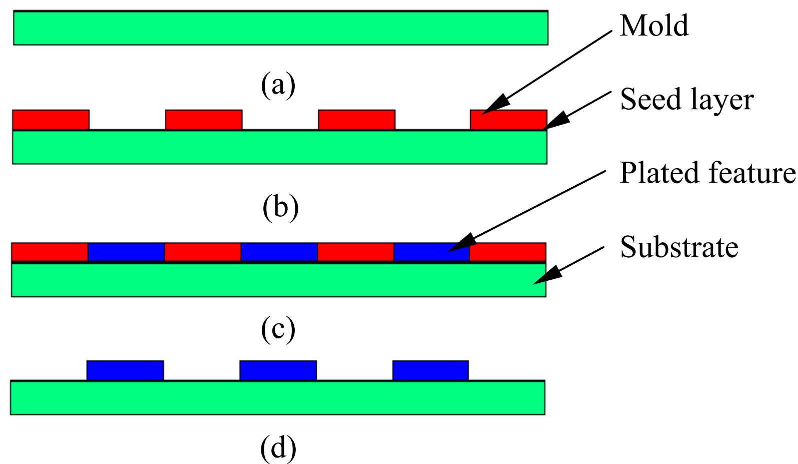

Figure 1.7: Schematic drawing of the UV-LIGA process. (a) deposition of metallic seed layer by PVD; (b) pattern the resist mold by photolithography; (c) electroforming; (d) after mold removal.

1.4 Electrochemical Deposition Rate

The deposition rate needs to be calculated out to guide the experiment. Electroforming is performed in a liquid solution called an electrolyte, otherwise referred to as the "plating bath".

The bath is a specially designed chemical solution that contains the desired metal ions (such as gold, copper, or nickel). In addition, various substances (additives) are introduced in the bath to obtain smooth and bright deposits. The object that is to be plated is submerged into the electrolyte (plating bath), acting as a negatively charged cathode. The positively charged anode(s) completes the electric circuit; those may be at opposite edges of the plating tank. A power source in the form of a battery or rectifier (which converts ac electricity to regulated low voltage dc current) is providing the necessary current (Figure 1.5). Now, in the bath the electric current is carried largely by the positively charged ions from the anode(s) toward the negatively charged cathode. This movement makes the metal ions in the bath to migrate toward extra electrons that are located at or near the cathode's surface outer layer. Therefore, it would appear that the thickness of the electroplated layer on the substrate is determined by the time duration of the plating.

For a single metallic ion in the electrolyte, the deposition of a metal, which occurs during the plating process, has been generalized as Equation (1.1).

$$M^{+n} + ne^{-} \Longrightarrow M \qquad (1.1)$$

Obviously, to reduce one mole of a given metal, "n" moles of electrons are required. That is, the total catholic charge used in the deposition "Q" (coulomb) is the product of the number of gram moles of the metal deposited "m", the number of electrons taking part in the deposition "n", Avogadro's number "N_a" (the number of atoms in a mole), and the electrical charge per electron "Q_e" (coulomb). Thus, the following equation gives the charge required to reduce "m" mole of metal:

$$Q = m\, n\, N_a\, Q_e \quad (1.2)$$

Now, the product of the last two terms in this equation is the "Faraday constant" "F". Therefore, the number of moles of metal reduced by charge "Q" can be obtained as:

$$m = Q / (n\, F) \quad (1.3)$$

On the other hand, the total charge used in the deposition can be obtained as the product of the current "I" (ampere) and the time of deposition "t" (second) if the deposition current is held constant. Or, if the current varies during the deposition:

$$Q = \int I dt \quad (1.4)$$

So, the number of moles deposited can be calculated as:

$$m = \frac{1}{nF} \int I dt \quad (1.5)$$

The weight of the deposit "w" (gram) can now be obtained by multiplying Equation (1.5) with the atomic weight "M_w" of the deposited metal. Finally, to calculate the thickness of the deposit, we have to use the density of the metal "ρ" (gram/cm^3):

$$\rho = w / V = w / (A\, T) \quad (1.6)$$

where "V" is the volume of the deposited metal in cm^3, "A" is the area of the deposit in cm^2, and "T" is its thickness in cm. Solving for thickness, using Equations (1.5) and (1.6) we have the useful practical expression:

$$T = \frac{w}{A\rho} = \frac{M_w}{nFA\rho} \int I dt \quad (1.7)$$

As mentioned above, if the current is held constant during the deposition, the integral in equation (1.7) can be replaced by the simple product of current and time "I×t". Therefore, (1.7) can be rewritten as

$$T = \frac{w}{A\rho} = \frac{M_w It}{nFA\rho} \tag{1.8}$$

If we define a new variable current density J=I/A, equation (1.8) can be written as

$$T = \frac{w}{A\rho} = \frac{M_w Jt}{nF\rho} \tag{1.9}$$

Applying equation (1.8) to nickel, we can Figure out its deposition rates vs. current (Figure 1.8) assuming that the current efficiency is 100% (95%-97% for real case). The constants used in this case are listed below:

F =96485 C mol $(e)^{-1}$

M_W =58.69 g mol^{-1}

n =2e

Density (ρ) =8.9 g cm^{-3}

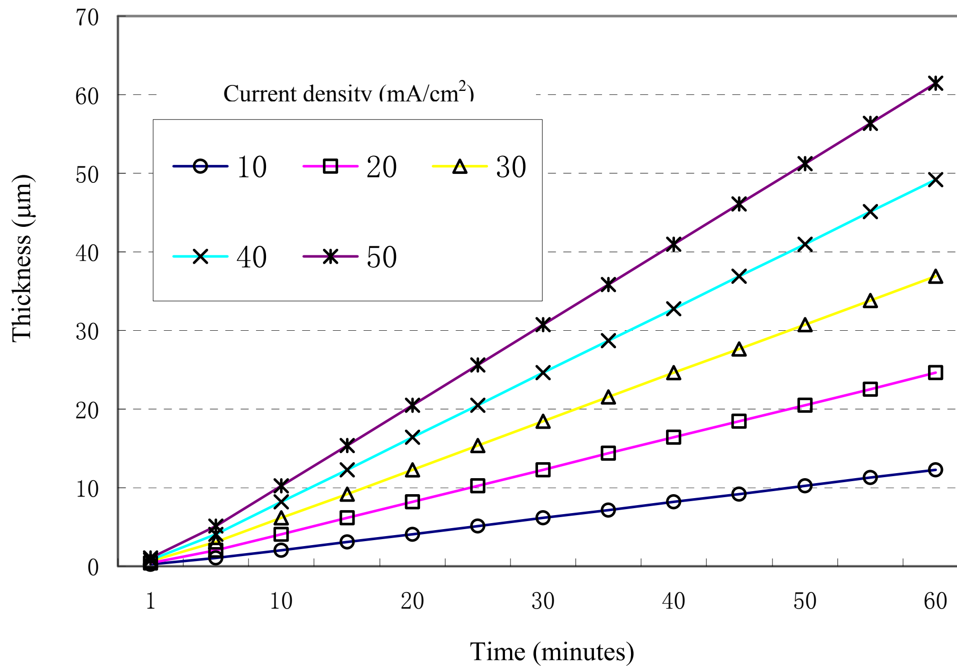

Figure 1.8: Nickel electrochemical deposition rate (calculated)

For copper, the deposition rate can be calculated using the constants listed below and is shown in Figure 1.9. The deposition rate is about 10% higher than that of nickel in the same conditions.

$$M_W = 63.55 \text{ g mol}^{-1}$$

$$n = 2e$$

$$\text{Density } (\rho) = 8.96 \text{ g cm}^{-3}$$

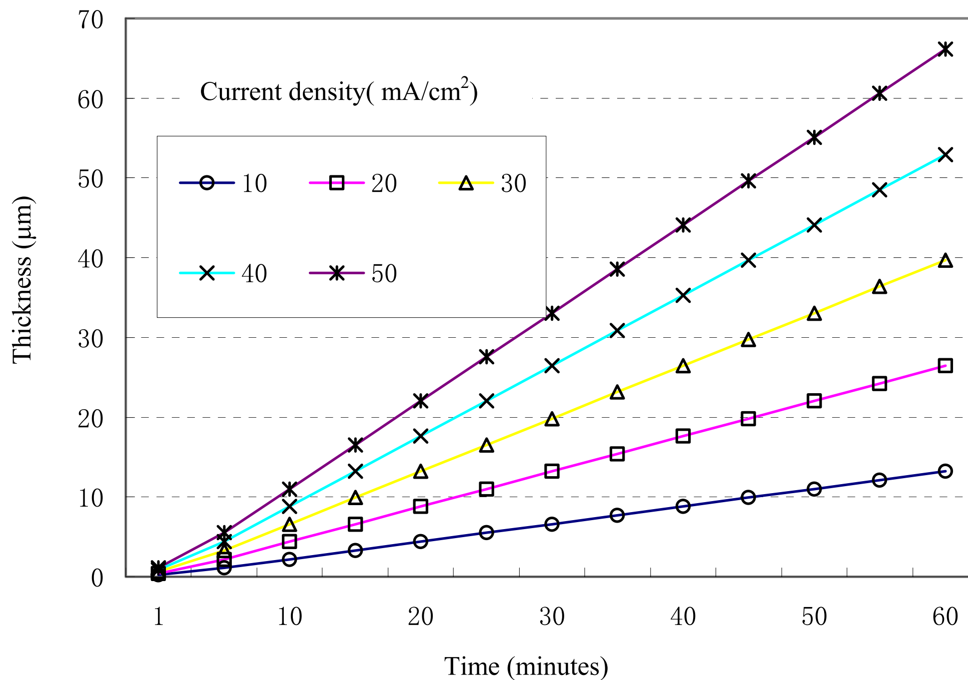

Figure 1.9: Copper electrochemical deposition rate (calculated)

1.5 Principles Governing Electroforming Process

To perform electroforming with good precision and finishing conditions, it is necessary to understand the principles governing this process. There are many factors that affect the

success or failure of through molds plating, including substrate cleanness, adhesion between substrate and seed layer, resist, developing solution, seed layer surface pretreatment, plating solution, resist removal. This represents a complex set of interactions, which will primarily affect adhesion of the plated film, nucleation and metallurgical structure. In addition to these, another important problems is the current distribution and mass transportation. For successful electroplating, it is required that the principles of mass transport and current distribution to be well understood [4].

1.5.1 Mass Transport

Mass transport is important in the plating process in that it determines the ultimate rate in the electrochemical micro-fabrication process. It has an important influence on the shape evolution of the electrode in through molds plating and affects the microstructures of the deposited metals. Even with vigorous agitation on the bulk solution, convection cannot reach very deep into very small and narrow patterns.

So, mass transport can be described by a diffusion model, in which metal ions diffuse to the bottom of the feature (cathode), where the concentration may be depleted due to the diffusion distance from the bulk electrolyte. As a result, the local deposition rate is smaller at the feature bottom. Thus, hydrogen bubbles will be greatly generated, which degrades the quality of the film. A simple dimensional analysis suggests that, assuming stagnant diffusion within the feature,

$$\tau \cong \frac{L^2}{D} \tag{1.10}$$

where τ is the characteristic diffusion time constant, L is the feature depth, and D is the diffusion coefficient of the metal ions. For L = 1 mm and D ~ 10^{-5} cm^2/s for a metal ion in water at 25 °C, τ = 1000 sec [5]. The diffusion time constant is important in choosing the time step for pulse plating [6].

1.5.2 Current Distribution

The uniformity of the thickness of electro deposition is determined by the current distribution on a macroscopic level. And on a smaller scale, the current distribution determines the shape evolution in through molds processes and the degree of leveling. In most applications, mass transport and current distribution are intimately related.

Three kinds of scales can be distinguished when studying current distribution on patterned electrodes: the *work piece scale*, the *pattern scale* and the *feature scale*.

At the *work piece scale*, the current distribution mainly depends on the cell geometry, anode and cathode size and position, agitation uniformity on the cathode and with or without auxiliary electrodes, which can be calculated in the same way as in other electrochemical reactors.

The size, spacing of the features and their geometry determine the current distribution on *pattern scale*. As the current flows through the cell (electrolyte), the local current density on the cathode increases at the patterns and current crowding occurs to an extent depending on

the size of the masked area. Figure 1.10 illustrates schematically the current distribution on the pattern scale and the feature scale [4]. The larger the surrounding covered area and the smaller the plated feature the higher will be the local current density because of current crowding. Therefore, the large and the small patterns will be plated at different rates. The smaller features will grow faster. The uniformity of current distribution at pattern scale can be improved by reducing the effective anode-cathode distance, optimizing the electrode arrangement and the cell design.

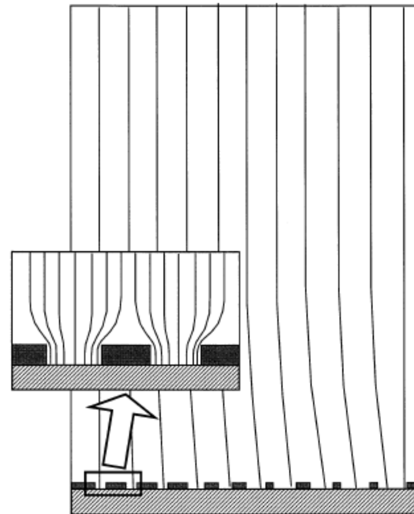

Figure 1.10: Schematic drawing of the pattern scale and feature scale current distribution on a patterned electrode (after reference [4]).

On the *feature scale*, the concentration field of the reacting species and/or the potential field in the feature determine the current distribution, which determines the shape of the growth front in plate-up plating and the homogeneity of cavity filling. In order to get uniform current distribution on the feature scale, leveling agent is used, which works as an inhibitor of the

metal deposition reaction. The valleys of a surface profile are more difficult to access than the peaks. Therefore, the peaks are more strongly inhibited by the leveling agent, leading to a more flat surface. Some additives for this purpose are coumarin and 2-Butyne-1, 4-diol.

1.5.3 Pulse Reverse Plating

Since the current distribution in the DC plating is by no means very uniform, which leads to a non-uniformly plated surface profile especially for thick structures. Therefore, it is necessary to use pulse reverse plating to achieve even surface. It is mainly a catholic deposition cycle followed by an anodic dissolution (etching) cycle, which offers the theoretical opportunity to achieve a more uniform current distribution [6].

To get uniform plating profile, the pulse parameters are chosen in such a way that the current during the plating cycle is more uniformly distributed than during the anodic etching cycle. Usually, a higher current density is applied in the anodic etching cycle, which gives a higher etching rate at the peaks leading to a flat profile finally. The schematic drawing of the pulse is shown in Figure 1.11.

The mean current density can be calculated by

$$j_a = \frac{j_p \times t_{on} - j_r \times t_r}{t_{on} + t_r} \tag{1.11}$$

where, j_p is the deposition current density in mA/cm^2, j_r is the electrochemical dissolving current density, t_{on} is the deposition time, t_r is the dissolving time.

The pulse reverse plating improves the feature-filling performance, however, it requires more complex equipments and a large number of electrochemical conditions must be controlled for the optimization of pulse parameters. An example of application of the pulse reverse plating is the through hole plating. Here, the plating rate is proportional to L^2/r, where L is the whole thickness and r is the hole's radius. So, the current distribution depends on the absolute dimension as well as on the aspect ratio.

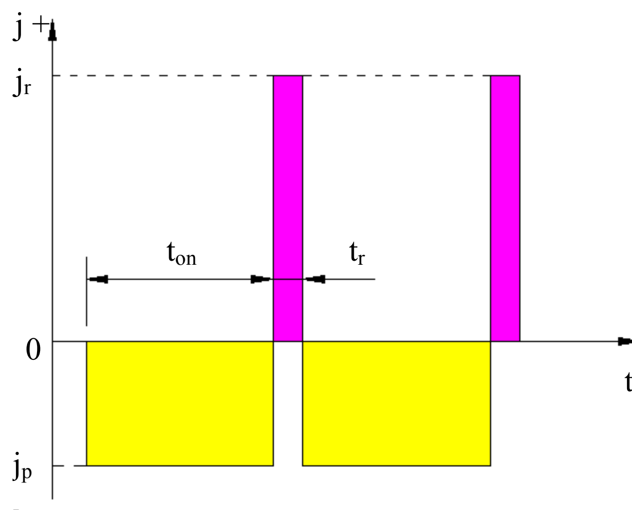

Figure 1.11: Schematic drawing of the pulse scheme

1.6 Scaling Laws in MEMS

With the characteristic length scale decreasing from the macroscopic to the micrometer size, micro devices could behave different from their macro counterparts. Due to the large surface area to volume ratio, surfaces and interfacial phenomena play a key role in MEMS performance and reliability. The effects of gravity become negligible as compared with adhesive and friction effects. Surface tension dominates gravity as dimensions diminishing.

Therefore, it is important to understand the scaling laws to design and understand the performance of micro devices.

1.6.1 Scaling Laws in Mechanics

Let us consider elements with a typical linear dimension L. In the following, except when explicitly stated, it is assumed that all the linear dimensions vary proportionally to L. This implies that all areas S vary like L^2 ($S \propto L^2$) and all volumes V vary like L^3 ($V \propto L^3$). This implies that the masses m scale to $m \propto L^3$ for incompressible media. So the *gravitation force*

$$G = mg \propto L^3 \tag{1.12}$$

Therefore the pressure exerted by the gravitation force is

$$P_G = G/S \propto L \tag{1.13}$$

The *adhesion force* between two surfaces is mostly caused by the Van der Waals type forces [84]. The attractive force experienced by an infinite flat slab separated by a distance x from another infinite flat slab is given by [85]

$$F_a(x) = H/(6 \pi x^2) \tag{1.14}$$

where H is the so-called Hamaker constant. H depends on the nature of the medium between the slabs. H is of the order of 10−19 J in air and of 10−20 J in water. This relation is valid for x between around 2 and 10 nm. It is obvious that $F_{vdw}(x)$ varies like the contact area.

$$F_a(x) \propto L^2 \tag{1.15}$$

It is obviously that the gravitation force and the surface adhesion force behave differently, and the adhesion force dominates the gravitational force at low L. Gravitation may then be

neglected at such small dimensions, both in the micro- and the nano-worlds. Therefore, the striction problem needs to be considered and solved when designing micro devices.

1.6.2 Scaling Laws in Fluid Mechanics

The transition from laminar to turbulent flow is given by the Reynold number Re. Re = $\rho vL/\mu$, where ρ is the density, v is velocity and μ is the dynamic (absolute) viscosity. If $v \propto L$, then

$$Re \propto L^2 \quad (v \propto L) \tag{1.16}$$

For the flow in pipes, the transition from laminar to turbulent flow occurs when $Re \cong 10^3$ [7]. In this case, turbulence disappears in micro systems in which liquids flow.

1.6.3 Resonant Frequency of the Cantilever Beams

Applying scaling laws, the resonant frequency of cantilever beams (Figure 1.12) used in Chapter 2 can be expressed.

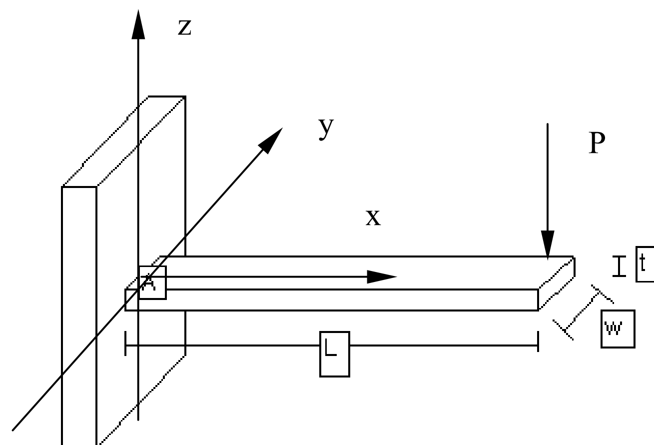

Figure 1.12: Typical cantilever beam studied

When a force P is applied to its transverse direction at the free end, the displacement at this end can be expressed as:

$$u(L) = -\frac{PL^3}{3EI} \tag{1.17}$$

where u is the transverse displacement, L is the length of the beam, E is the modulus of elasticity and I is the moment of inertia. So, the stiffness of the beam k is

$$k = \frac{3EI}{L^3} \tag{1.18}$$

In this case, I can be determined by

$$I = \frac{1}{12}wt^3 \tag{1.19}$$

the resonant frequency in traverse direction can be determined by

$$f_0 = \frac{1}{2\pi}\sqrt{\frac{stiffness}{effective\ mass}} \tag{1.20}$$

The effective mass is the equivalent moving mass of the beam and can be determined by

$$m_{eff} = \frac{33}{140}m = \frac{33}{140}\rho Lwt \tag{1.21}$$

Therefore,

$$f_0 = 0.164\frac{t}{L^2}\sqrt{\frac{E}{\rho}} \propto \mathrm{L}^{-1} \tag{1.22}$$

For the nickel beam used in chapter 2 with L=400 μm, t=10 μm, E=211 Gpa (bulk) and ρ=8900 Kg/m^3, the resonant frequency can be derived as *49.9 KHz* from equation 1.22. For comparing, if we increase the dimensions 100 times proportionally (L=4 cm, t=1 mm), then

the frequency will be reduced to *499 Hz*. So, scaling laws are valid in the frequency of micro devices.

1.6.4 Squeeze-Film Damping

Damping issue is a crucial concern for RF MEMS and our microvalve design, where the frequency and quality factor need to be considered. According to Andrews et al [86, 87], the quality factor is dominated by squeeze-film damping (Figure 1.13) in these devices.

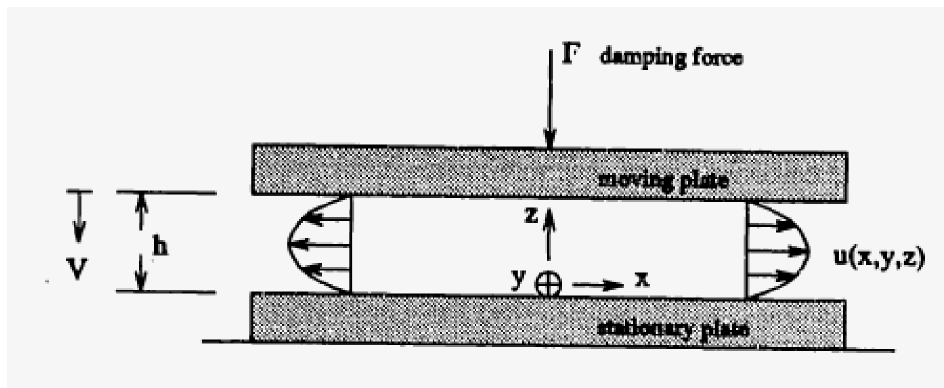

Figure 1.13 Squeeze film damping

where F is the damping force, V is the relative velocity between the two plates, u is the fluid velocity and h is the gap between the two plates.

For incompressible fluid, the damping coefficient has been derived [86, 87] as

$$B = \frac{F}{V} = 0.4217\mu \frac{A^2}{h_0^3} \tag{1.23}$$

where A is the area of the moving plate, μ is the dynamic viscosity of the fluid and h_0 is the initial gap between plates. So the damping ratio can be obtained from

$$\zeta = \frac{B}{4\pi M_{eff} f_0} \tag{1.24}$$

where M_{eff} is the effective of the system, and f_0 is the undamped resonant frequency. Finally, the damped resonant frequency f_d can be found as

$$f_d = f_0\sqrt{1-\zeta^2} \tag{1.25}$$

1.7 Objectives of the Research

The dissertational research focused on designing, fabricating and characterizing novel 3-D MEMS devices with electroformed nano-structured materials. Scaling laws are applied in the design to achieve highly functional devices. The developed micro devices and processes are listed below:

- Development of a robust hybrid nickel-silicon microvalve using UV-LIGA electroformed nickel;
- Development of a robust monolithic solid nickel microvalve using a bottom-up in situ UV-LIGA electroforming process;
- Development of micro heat-exchangers for cryogenic heat transfer;
- Development and characterization of copper/carbon nanotube nanocomposites with decreased CTE (coefficient of thermal expansion) and increased thermal conductivity for heat spreading.

- Mechanical and material characterization of electroformed nickel and nanocomposite for MEMS devices using micromachined specimens;

Firstly, compact microvalve arrays for robust pumps were developed and tested, where both nickel and silicon were used for the valve fabrication. The completed valve has a high frequency (>10 kHz), high flow rates (10 ml/sec) and high-pressure support (>10 Mpa). However, the silicon material used may be a problem when large dynamic loads are subjected. In this case, more robust compact microvalve arrays would be needed. Therefore, self-assembled solid nickel microvalves were developed and tested.

Second, laminated micro heat exchanger was developed by the UV-LIGA process, where patterned SU-8 and the electroformed nickel were used as structural materials with micro fluid channels inside. The fabricated microstructure passed cryogenic test without any structural damages.

Third, copper/SWNT nanocomposite was developed through electroforming process by dispersing SWNTs in copper electrolyte and being co-deposited with copper when plating. Density measurement implies the content of SWNT is approximately 18 percent. The measured CTE is greatly reduced from pure copper while its thermal conductivity is greatly improved, making it an ideal candidate for heat spreading.

Finally, for better understanding the mechanical behavior in micro scale and validating simulation results of MEMS devices, mechanical testing was conducted using microfabricated specimens. Results were obtained and presented in this dissertation.

CHAPTER 2 ELECTROFORMED ROBUST LARGE FLOW RATE PASSIVE HYBRID MICRO CHECK VALVES

2.1 Introduction

Compact actuators are currently being proposed for space related applications [1,7]. Compact robust actuators are important because they provide larger power per unit volume/weight ratio than conventional actuators. Actuator requirements include large displacements, large output forces, a high bandwidth, and a high precision together with a compact size. One example is that NASA intends to reduce the launching cost dramatically from current $8000/pound to $100/pound by 2025 [7]. Miniaturization will play an important role for achieving the objective, as any reduction in mass or power required for a space instrument or subsystem results in an exponential savings for launch cost [7]. MEMS based microvalves and compact piezoelectric pumps represent key components for fluid management systems to meet the rigorous performance requirements for various space applications. For example, NASA has identified a low-leak space qualified regulator valve as a key technology for enabling micro-instruments, micro-spacecraft, and the future of space exploration [7].

Hydraulic compact actuators consisting of piezoelectric stacks and robust microvalves represent an alternative approach to other compact actuators. These hydraulic actuators produce power per unit volume ratio about 100 to 1000 times greater than their electrostatic counterparts. Compact pumping components (pusher) are fabricated with smart (active) materials due to simplicities in design and high power densities. These smart materials

include, but are not limited to, piezoelectric materials, magnetostrictive materials, shape memory alloys and phase change materials [8]. Requirements for compact pumping components include large displacements, large force outputs, high working frequencies, low energy consumptions (high efficiency) and ease of operation. Generally speaking, piezoelectric materials produce larger force outputs at high operation frequencies (up to 100kHz) with small displacements (<0.5%); shape memory alloys produce large displacements (up to 8%) and very high energy densities with low working frequencies (<100Hz). Other materials and/or driving mechanisms are ranked in between the piezoelectric material and shape memory alloys, in terms of forces, displacement outputs and the operational frequencies.

Robust microvalve is required to perform two functions as a component of a hydraulic actuator (pump). One function is manipulating/directing/switching the flow direction (forward or backward) and the other one is to bear the load when the valve is in a closed state. Therefore, requirements for compact valves are stricter than those for a pumping component (pusher), in addition to the common limitations encountered in MEMS devices [9]. Nevertheless, valves should be able to open wide (enhancing forward flow) and close tightly (preventing back flow). A high operation frequency is required for microvalves to produce high flow rates such that large displacements could be achieved for the hydraulic actuator.

Current research on micro valves can be classified as active (self controlled) valves and passive valves (controlled by the pressure difference produced by the pusher) [10-22]. Research on non-mechanical moving parts or valveless system is not referenced in this article

due to the small pressure gradient and/or small flow rate produced. In general, active valves have a relatively quicker response time or higher frequency response (for example, up to 100 kHz for piezoelectric valves). However, they provide only low to moderate flow rates due to either small displacement (piezoelectric) or longer response time (shape memory alloys). The active valves also need additional control unit (power activated) for operation so that additional power consumption is required. This will make a complicate design and hard to fabricate. In addition, the synchronization between pumping component (pusher) and the valve is challenging at high frequencies.

On the other hand, passive valves or check valves are operated by pressure differences created by the pumping component (pusher). These valves have been successfully tested in both macro scale and micro scale applications [10,11,12]. While successful in operation, these passive valves are typically more susceptible to back flow (leaking) problems. In addition, traditional passive valves (macro scale) are considered to be low frequencies, i.e. less than 500 Hz [10]. However, the emerging MEMS techniques provide the opportunity to design and fabricate high functional passive valves. Scaling laws have proven that micro mechanical systems could be changed greatly when the physical dimensions shrink [12] and they should apply equally to robust micro valves.

This research investigates the feasibility of utilizing micro mechanical passive valves to achieve high operational frequencies, large flow rates and large pressure support for a robust compact piezoelectrically actuated pump. Scaling laws were applied to the design. A novel micro reinforced valve flap is employed to provide high-pressure capabilities, i.e., 10 MPa

when the valve is closed. It is also designed to work at frequencies larger than 10,000 Hz. With a specially designed valve stopper, the valve is also capable of preventing potential tear-off of the valve flap under an extreme high pressure when it is open. Test results show that a flow rate of 18 cc/sec can be achieved under a pressure of 50 psi. The work indicates that microvalves can be used to support extremely high-pressure difference (> 10 MPa) and large flow rates (>10 cc/sec) with high operational frequencies (>10 kHz).

2.2 Microvalve Design

2.2.1 Requirements

The micro mechanical passive valve designs are based on the requirements for compact hydraulic actuators being developed for space applications [23,24]. The requirements on the integrated micro valves include:

- Ability to support pressure differences of 10 MPa or larger;
- Flow rates of 10 cc/sec or larger;
- Operating frequencies of 10 kHz or larger;
- Low or no power consumption.

As described below, current MEMS based microvalves can meet all these requirements.

2.2.2 Hydraulic Actuator and Microvalve Structure

Figure 2.1 is a sketch of the microvalve design integrated with a compact robust pump (the hydraulic actuator) being developed. A piezoelectric stack is used as the pump pusher, which

produces large pressures and high flow rates when operated at high operating frequencies. The pump pusher (PZT) deforms a membrane to compress the liquid in the chamber to open the valve. The pump is 50 mm long and 25 mm in diameter (Figure 2.1).

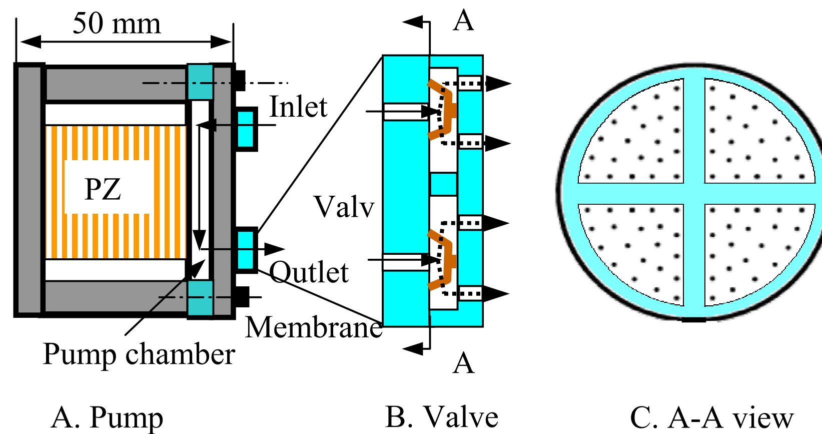

Figure 2.1: Sketch of compact pump and integrated microvalves (not in scale)

The microvalve developed is a mechanical normally closed check valve (Figure 2.2 and Figure 2.1 b for array). The microvalve consists of inlet channels and novel nickel valve flaps, and a valve stopper (Figure 2.2). Liquid is directed through orifice of the valve flap and passing the outlet channels fabricated on the valve stopper. The gap between valve flap and valve stopper is 10 μm. The valve flap (Figure 2.2) is linked with four identical micro beams (springs), which hold the valve flap to the valve substrate and thus closes the valve channel (200 μm in diameter, Figure 2.2) elastically.

The valve is opened by a pressure pulse produced by the PZT actuator (Figure 2.1 a), where forces liquid passing the valve inlet channels and then through the valve flap (Figure 2.2). The valve returns closed by the spring force developed in the four beams in addition to the

reverse pressure difference upon PZT's contraction (Figure 2.1). The size of the valve-flap (square) is 300 μm x 300 μm held by four beams (50 μm x 400 μm each) and the thickness is 10 μm for both the valve flap and the beams. A cross-shaped nickel structure (300 μm x 40 μm x 20μm) is designed on top of the valve-flap (Figure 2.2). It is used to increase the valve's load bearing ability.

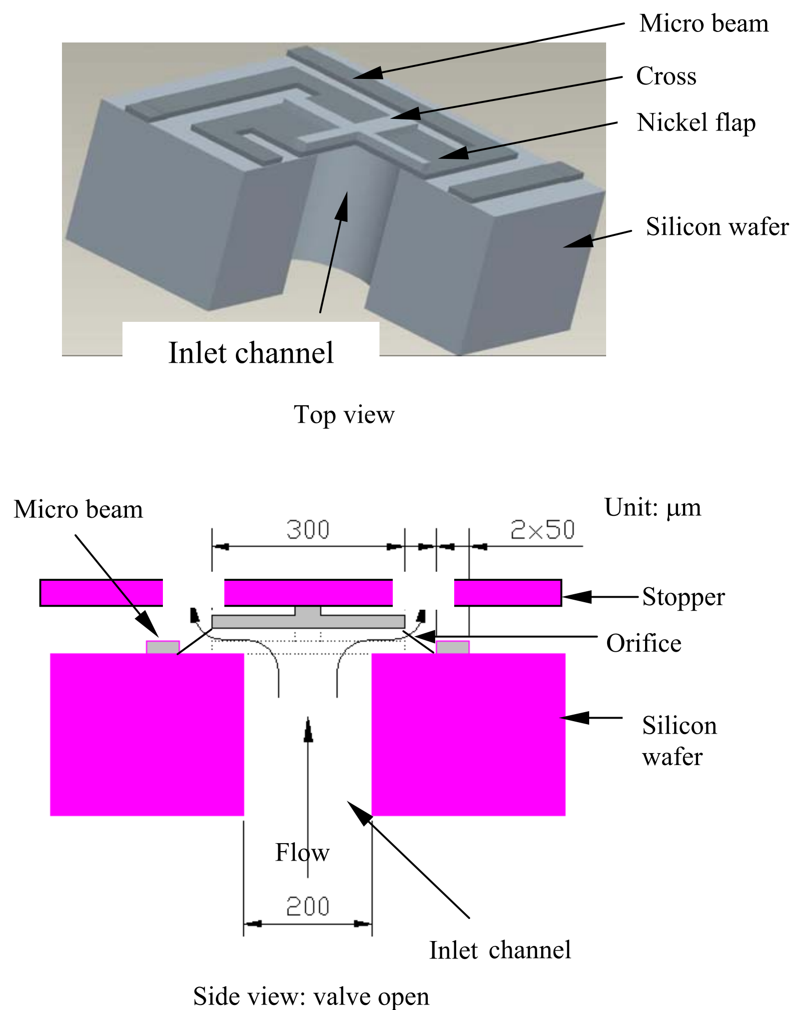

Figure 2.2: Details of individual microvalve of valve array shown in Figure 1 C

2.2.3 Flow Rate Calculation

The flow rate requirement needs to be fulfilled. So, it is important to predict the flow rates of the valve for different pressure differences applied. Equation for flow rates was developed based on Bernoulli equation.

When the valve is open (see Figure 2.3), the fluid flow beneath the thin plate is absolutely a Newtonian flow. If entrance effects are neglected, the pressure drop can then be given by the Bernoulli equation. By expressing the fluidic resistance, and the velocity, the pressure drop can be written as:

$$\Delta P = \frac{12\mu L_s Q}{\pi D_s \Delta z^3} \tag{2.1}$$

where μ is the dynamic viscosity of the fluid (for water μ=0.001 N-s/m^2), Q is the volume flow rate, Δp is the pressure difference and Δz is the maximum deflection of the beam. Therefore, the flow rate can be written as:

$$Q = \frac{\pi D_s}{12\mu L_s}\left(\Delta P \Delta z^3\right) \tag{2.2}$$

The flow rate under different pressure is obtained from equation 2.2 with a duty of 50% assigned due to the operational mechanism (Δz is fixed to 10 μm based on the structure, Figure 2.4).

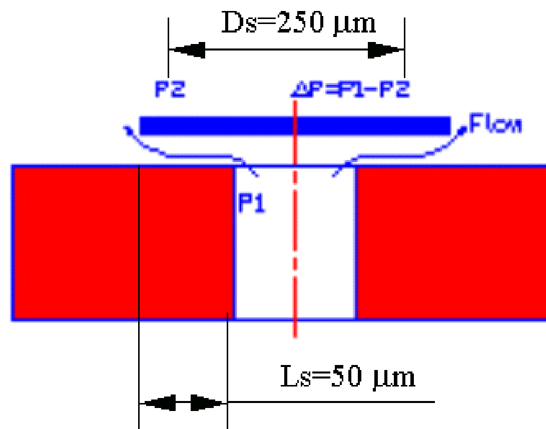

Figure 2.3: Scheme of flow rate calculation parameters

Calculation results (Figure 2.4) indicated that a single valve with above-mentioned dimensions could not produce sufficient flow for this research. Larger valves would reduce the frequency and the load bearing ability, and are therefore not an option. In order to meet the flow rate requirement (> 10 cc/sec), a compact robust microvalve array consisting of 84 individual valves has been adopted (Figure 2.1 C). The resulted flow rate would be 84 times larger than that of a single valve so that flow rate of 10 cc/sec could be easily achieved at a relative low pressure (30 Psi in Figure 2.5). Array of 84 valves was selected due to the symmetric arrangement over the 12 mm in diameter proposed from the pump design.

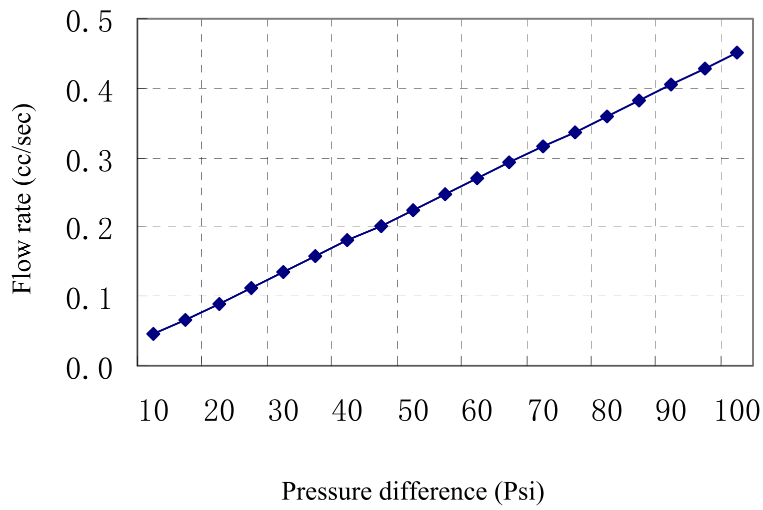

Figure 2.4: Calculated flow rate of a single micro valve

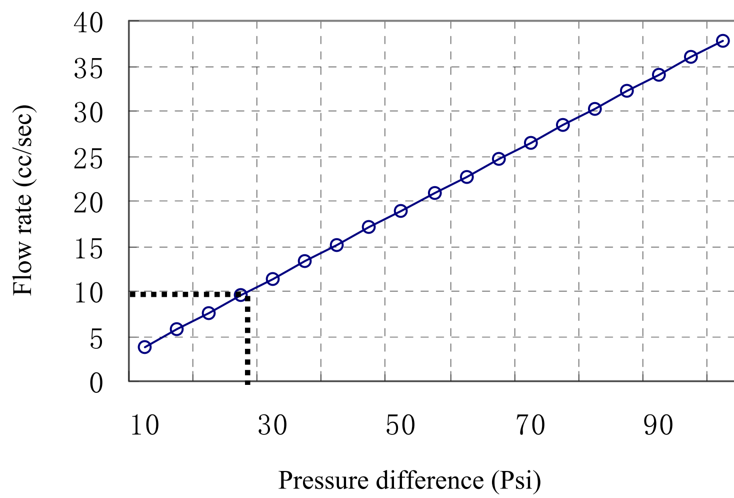

Figure 2.5: Calculated flow rate of 84 micro valves

2.3 Finite Element Analysis

Static finite element analysis was conducted to predict the stress distribution over the valve flap and the silicon substrate both in the open and close condition. The resonant frequency was also simulated to validate the design. The properties of nickel used here are: density of 8.88 g/cc, modulus of elasticity of 207 Gpa and Poisson's Ratio of 0.31 (bulk).

2.3.1 1st Mode Resonant Frequency and Damping

Finite element simulation was conducted with the help of I-DEAS. In this case, the ends of the cantilever beams (spring) were clamped. Results show that the first natural frequency of the valve is 30.8 kHz in vacuum. This is much higher than the required PZT actuator's designated working frequency (10 kHz). Therefore, it is safe for the valve to work at this frequency. This is also a major advantage of MEMS devices due to scaling laws. With the dimensions shrink with MEMS devices, the natural frequency will be improved greatly. The mode shape is shown in Figure 2.6.

The damped frequency can be calculated using equations (1.23) – (1.25). First of all, the damping coefficient B can be calculated from

$$B = 0.4217\mu\frac{A^2}{h_0^3} = 0.4217\times 0.001\times\frac{(300\times 10^{-6})^4}{(10\times 10^{-6})^3} = 3.42\times 10^{-3}\ \frac{N\bullet S}{m} \quad (2.3)$$

The effective mass of this system is a combination of the mass of the flap and the effective mass of the beams, which can be derived from

$$M_{eff} = 8900 \times [4 \times \frac{33}{140} \times (400 \times 50 \times 10) + 4 \times 50 \times 50 \times 10 + 560 \times 40 \times 20 + 300 \times 300 \times 10] \times 10^{-18} = 1.46 \times 10^{-8}\ Kg \quad (2.4)$$

So the damping ratio can be obtained from

$$\zeta = \frac{B}{4\pi M_{eff} f_0} = \frac{3.42 \times 10^{-3}}{4\pi \times 1.46 \times 10^{-8} \times 30.8 \times 10^3} = 0.605 \quad (2.5)$$

Therefore the damped resonant frequency is

$$f_d = f_0 \sqrt{1 - \zeta^2} = 30.8 \times \sqrt{1 - 0.605^2} = 24.5 KHz \quad (2.6)$$

This is still much higher than the required PZT actuator's designated working frequency (10 kHz).

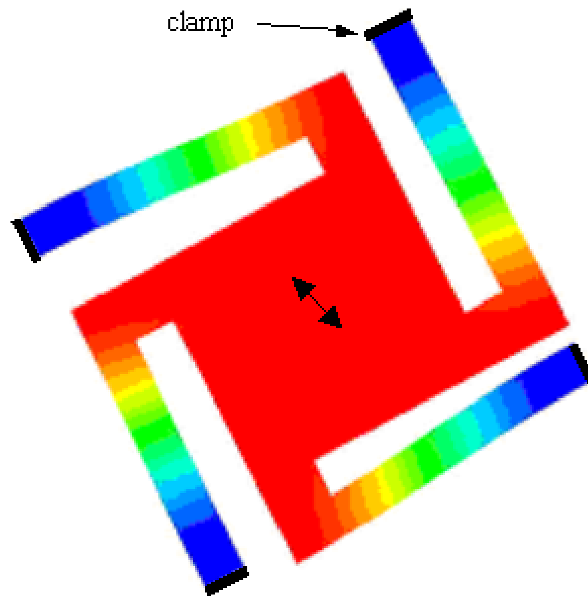

Figure 2.6: First mode natural frequency of the micro valve flap

2.3.2 Stress Analysis of the Valve Flap

As the key component of the microvalve, the safety of the flap is extremely important. In order to predict any potential damages occurring in the flap, the stress distribution was analyzed to find the maximum value and its locations. If they are beyond the strength limits of the material, changes of the design will apply. For all the simulation discussed below, the ends of the beams were fixed and pressure differences were applied on one side of the flap.

2.3.2.1 Stress on the flap when it is fully opened

It is anticipated that the pressure differences acting on the valve flap during the open period are not very high (pressure difference over the valve flap, less than 100 psi). Therefore, a pressure difference of 1 atmosphere (14.5 Psi) was applied on the valve flap. The stress distribution on the valve flap was illustrated in Figure 2.7.The maximum von misses stress is 191 Mpa, which corresponds to a maximum deflection of 6 μm in the center of the flap. It is reasonable to predict that the stress is proportional to the deflection in the elastic range. The deflection is determined by the pressure difference applied.

The maximum stress on the cantilever beams as well as at the connections by beams and the flap will be very large if the flap can move unrestrictedly, during “open” state of the valve. In order to prevent any potential failures such as permanent deformation or tear off of the beams in case of large pressure differences applied; a valve stopper has been designed (Figure 2.1 and Figure 2.2). The valve stopper is fabricated out of silicon wafer and bonded on top of the

flap to stop the valve-flap motion to a limited distance (10 μm) during the open period (Figure 2.1 b and Figure 2.2). The gap of 10 μm is chosen such that the maximum stress is in the allowable range as well as a high flow rate can be maintained (Figure 2.5). The maximum stress of 318 Mpa for a deflection of 10 μm can be predicted elastically from Figure 2.7, which is allowable for the nickel material used from the results of strength testing in Chapter 6. Test results show that micromachined nickel has a tensile strength larger than 800 Mpa. Nevertheless, the cross pattern will also overcome potential stiction problems when the valve-flap touches the valve stopper during open periods

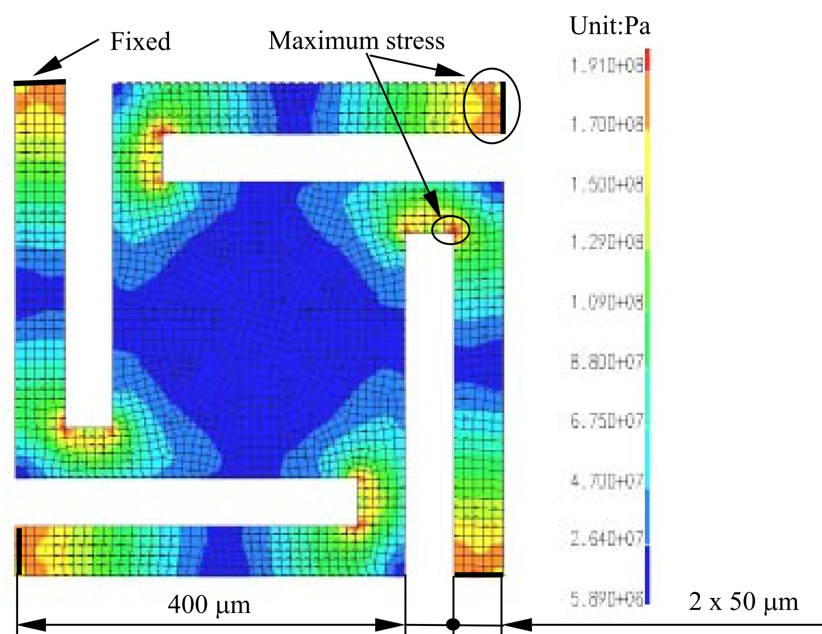

Figure 2.7. Stress distribution over microvalve flap while it is fully opened

2.3.2.2 Stress on the flap when it is closed

As mentioned above, the valve needs to support pressure larger than 10 MPa when it is closed. The valve flap is the key component for this load bearing. As the valve flap is a membrane (10 microns thick), it is difficult to support such a high pressure without permanent deformation/damage (predicted by FEA simulation). To overcome this problem, a micro cross structure is designed to add on top of the valve flap. Even though the cross has a small dimension (300 x 40 x 20 μm), the effect of stress reduction is tremendous.

It indicated that the maximum von misses stress of the valve flap with cross pattern could be reduced by a factor of 5 than that without cross when the valve is closed to support 10 MPa pressure (Figure 2.8). Figure 2.8 shows that with the help of the micro cross structure, the valve flap can stand up to 10 MPa pressure difference without failure. The maximum stress of 180 Mpa under pressure of 10 MPa occurs in the micro cross instead of in the flap when no cross present. The stress is safe for the flap according to the testing results from Chapter 6. This pressure support ability is 4 times larger than that without the cross structure.

2.3.3 Stress Analysis of Silicon Substrate

A silicon piece (12 mm in diameter and 500 μm thick) is used to support the valve flap and to house the inlet channels. It is anticipated to hold pressure when the valve is closed. Therefore, stresses will be generated over it during operations. The valve was supported in such a way that can minimize the stress, as shown in Figure 2.9.

Due to the symmetry of the geometry, only one quarter of the silicon substrate was simulated. Commercially available (100) single crystal silicon is used with Young's Modulus of 150 Gpa and Poisson's Ratio of 0.17: all the edges shown in Figure 2.10 were fixed. The stress results were illustrated in Figure 2.10. The maximum stress is 179 Mpa, which is located in the edges of the structure. The published value from [25] is as high as 1Gpa for RIE fabricated single crystal silicon, as being used in the fabrication described below. Therefore, this silicon structure is safe.

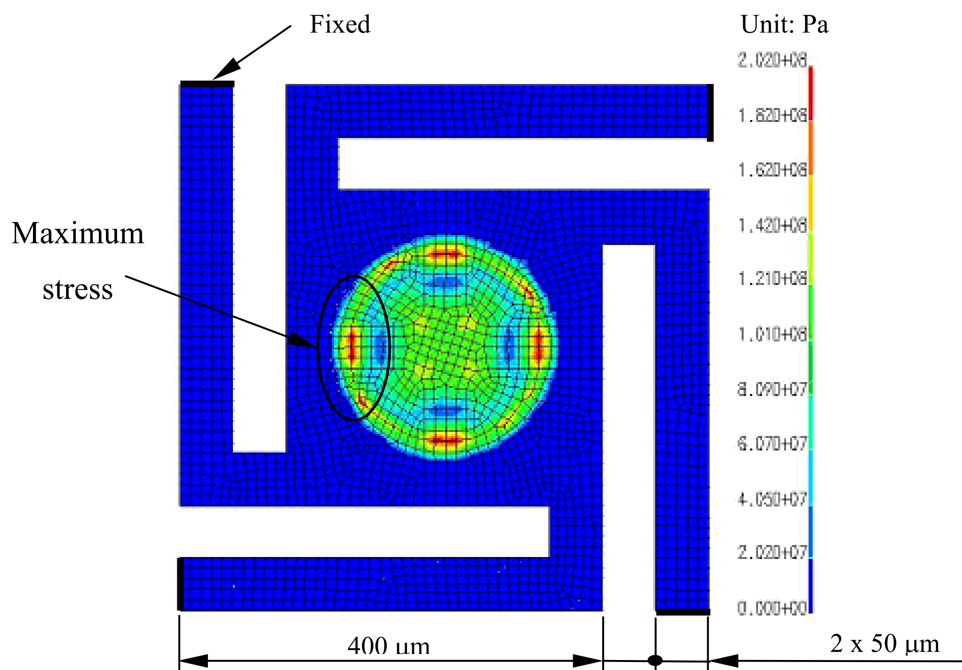

Figure 2.8: Stress distribution of microvalve under 10 MPa pressure while closed.

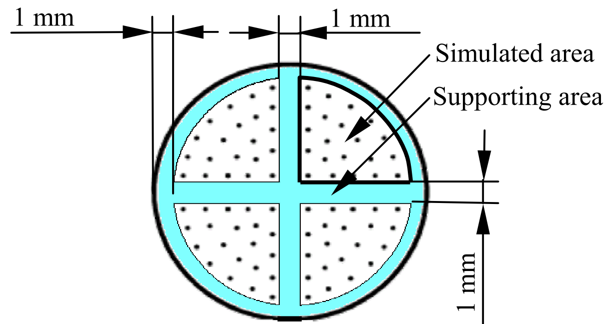

Figure 2.9: Supporting area of the valve & the silicon substrate

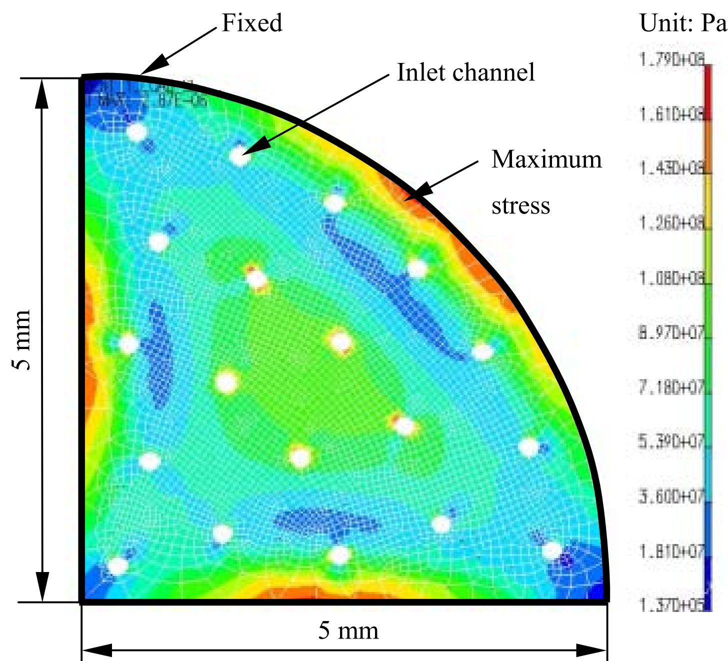

Figure 2.10: Stress distribution of silicon substrate under 10 MPa pressure while closed.

In summary, the designed valve structure is safe both for the nickel and the silicon according to the finite analysis results. The valve is predicted to be able to support pressure differences up to 10 Mpa while maintaining a large flow rate. The 1st natural frequency of the flap is very high (30.8 KHz), which allows the valve to operate at 10 KHz without resonance related damages.

2.4 Fabrication

An innovative fabrication process was designed with the concern of the available equipment and the needs for the precise machining. The process consists of etching inlet channels in a silicon substrate, electroforming nickel the valve flap and the micro cross, etching outlet channels in another silicon substrate and separating valves and stoppers from the silicon wafers for packaging.

As illustrated in Figure 2.12, the valve flap and the micro beams as well as the cross pattern are fabricated by electroforming nickel on a silicon wafer with patterned photoresist as molds (Figure 2.11) and a spurted (or evaporated) metallic thin layer as the starting seed. The nickel electroforming solution used was a slightly modified Watts bath [26] based on experimental results conducted during the development regarding of internal stress and surface roughness. The solution contained $NiSO_4 \cdot 6H_2O$ 350 g/l, $NiCl_2 \cdot 6H_2O$ 25 g/l, H_3BO_3 40 g/l and Saccharin 0.1 g/l. The PH value of the solution was held at 4.0~4.5 and the temperature were kept constant at 60 °C. A nickel deposition rate of 12 μm/hour was achieved by maintaining the current density of 10 mA/cm^2.

The fabrication process (Figure 2.12) starts with a silicon wafer coated with a thin layer of Cr/Cu by the thermal evaporation (or spurting) for nickel electroforming. Then photoresist (shapely 1075) was applied and patterned by photolithography to form the electroforming molds. After electroforming the valve flap and micro beams, another layer of photoresist was applied and patterned serving as the molds for the electroforming of the cross. Next

electroforming was conducted to generate the micro cross. Finally the whole flap pattern containing the cross was formed (Figure 2.13).

Next, a deep reactive ion etching (RIE) process was used to fabricate the valve inlet channels (100 micron in radius) and separate the silicon supporting substrate from the backside of the silicon wafer with the help of a double-side aligner. The RIE etching stopped at the nickel valve flap when all silicon underneath was etched out. The valve-flap and beams are then released by removing a sacrificial layer underneath.

The valve stopper was fabricated by wet chemical etching to make the cross ribs similar to that of the valve. Deep RIE was used to open outlet channels on the silicon substrate (as a valve stopper) for liquid passages when the valve is open. A separation etching was performed during etching of channels (both on inlet substrate and outlet or valve stopper substrate). No dicing (actually it is difficult to dice circular shape) is needed. The valve

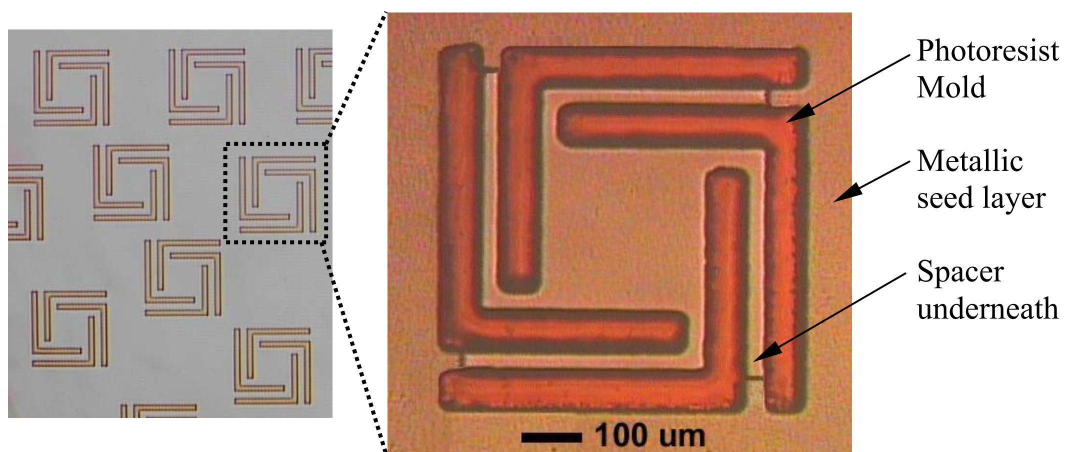

Figure 2.11: Photoresist mold (thickness 12 μm) for the flap electroforming

stopper was then bonded on top of the valve array and final device (weighs 0.2 grams) was ready (Figure 2.14) for testing. The fabrication process is shown in Figure 2.12.

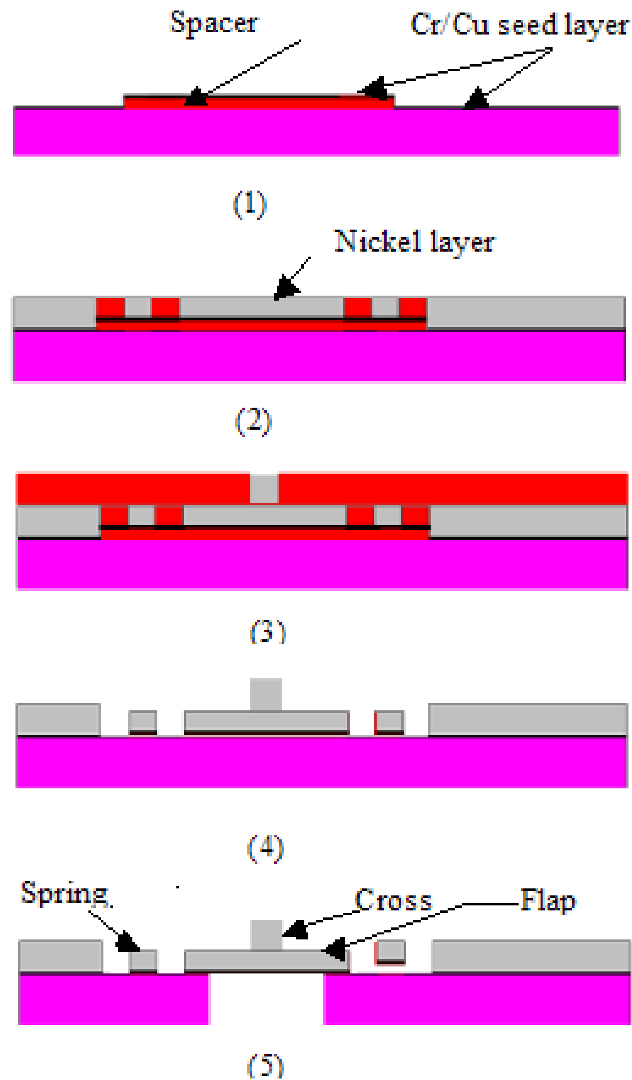

Figure 2.12: Fabrication process: (1) Spacer with seed layer on the top; (2) Nickel plating of the springs and the flap with PR mold; (3) Cross plated; (4) Structure released by lift-off; (5) Hole etched by deep RIE etching

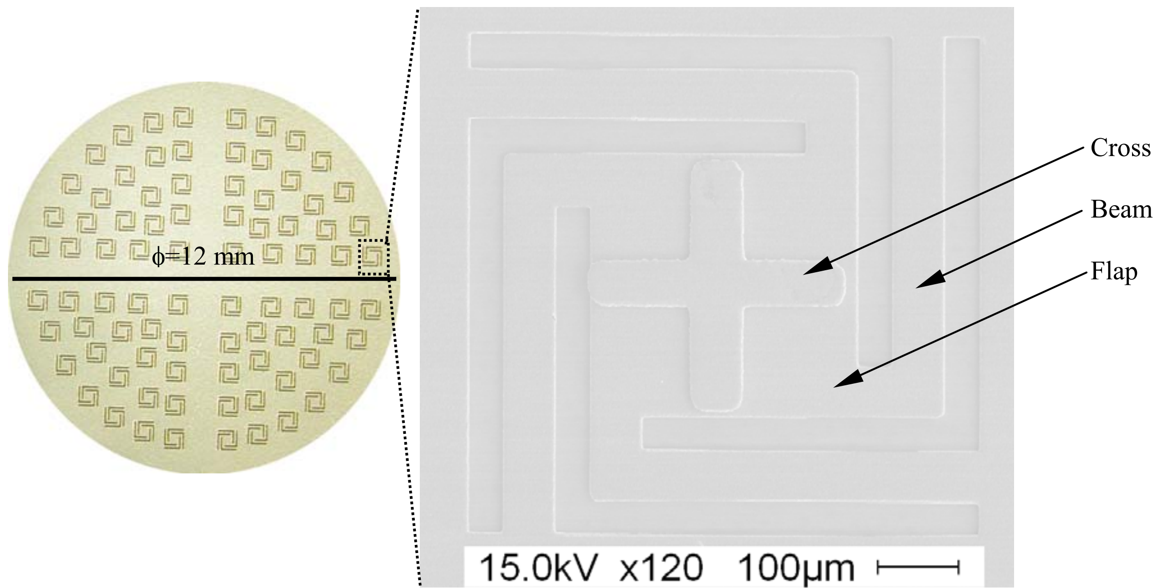

Figure 2.13: Array of microvalves (84) over 6-mm radius area before bonding with valve stopper

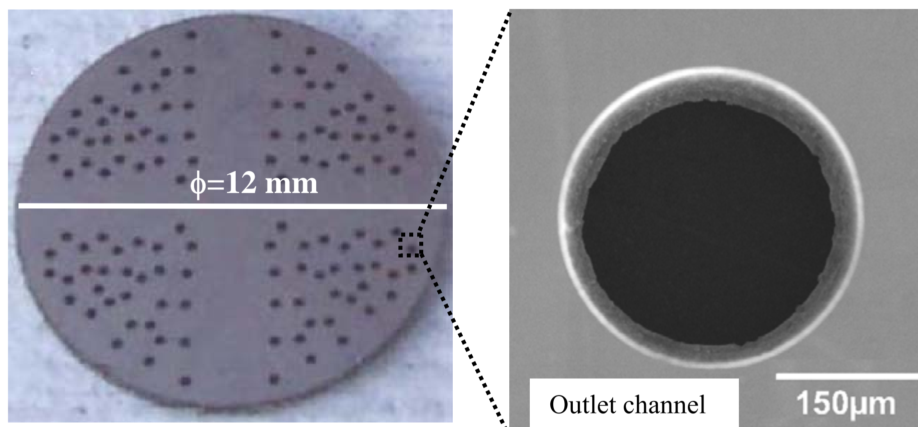

Figure 2.14: Microvalve arrays (84) after bonding with valve stopper (top view). The device weighs 0.2 grams in total.

The electroformed nickel was studied in the material aspect in terms of grain size and morphology. Figure 2.15 shows the surface profile of the electroformed nickel. It is obvious that the grain size in this material is in the nano meter range. It is expected that the yield strength (σ_y) of polycrystalline metals and alloys will increase with decreasing grain size (d) according to the well-known Hall–Petch (H–P) equation [99]:

$$\sigma_y = \sigma_0 + kd^{-1/2} \tag{2.7}$$

where σ_0 is friction stress resisting the motion of gliding dislocation, and k is the Hall–Petch slope, which is associated with a measure of the resistance of the grain boundary to slip transfer. Therefore, the electroformed nickel is expected to have a higher strength than conventionally fabricated nickel, which has a larger grain size. This is proved by the tensile test results as described in chapter 6.

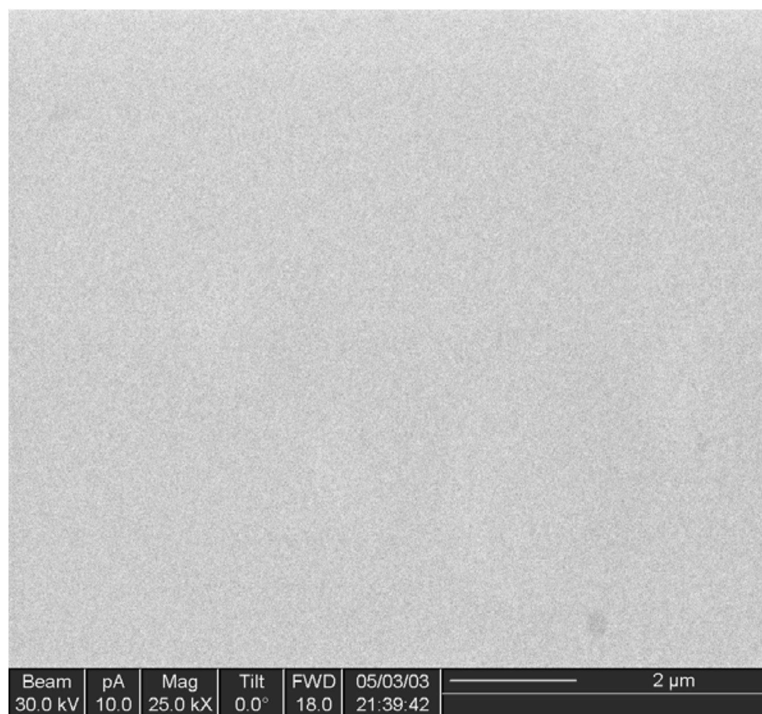

Figure 2.15: Nanostructured electroformed nickel.

2.5 Test Results and Discussion

The characterization of the microvalve was performed by measuring the flow rates on an array of 84 single valves under different pressure conditions. The valve array was held by a specifically designed valve holder (upper left, Figure 2.16) while a pressure difference is applied. DI water was used for testing.

2.5.1 Single Static Testing

Static test was performed by raising the pressure from low to high for both the forward flow and the backward flow. Test results of flow rates versus applied pressure differences are provided in Figure 2.16. From the results the valve's crack pressure is determined to be about 5 Psi. The measured flow rates is proportional to the pressure differences applied, as predicted by Poiseuille's law. The flow rate is about 18 cc/s at a pressure difference of 50 psi, which is the largest pressure tested. Much higher flow rate is expected if larger pressures are applied based on Poiseuille's law. On the other hand, the valve sealing is very good as the backflow rate is negligible (Figure 2.16).

2.5.2 Repeat Static Testing

In addition to the valve's functional performance, the valve's durability/reliability is another relatively important concern. A specific loading/unloading sequence was designated to testify the valve's durability. The tested loading parameters are indicated in the lower right in Figure

2.17. Ramped pressure differences were applied over the valve flap and then released back step by step in an interval of 10 psi. The flow rates were measured at each pressure level during the testing process. The tested pressure progressed from lower pressure to higher. Flow rates versus applied pressures are shown in Figure 2.17.

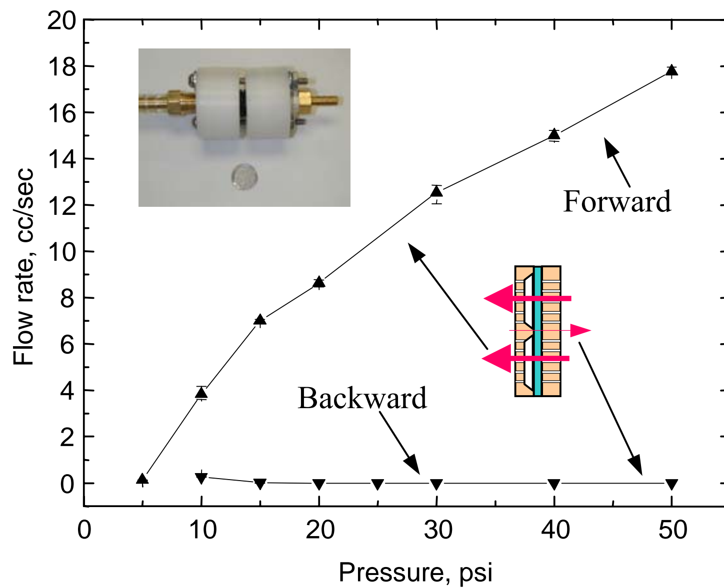

Figure 2.16: Forward and backward flow rates under pressure differences (water)

The test results in Figure 2.17 show that the flow rates measured repeat very well at similar pressure levels over a the range of pressure differences tested. The flow rates are really linearly proportional to the pressure differences applied, regardless of how the pressure was applied. This indicates that Poiseuille's law is valid for this structure during the test. An important fact is that there were no damages or permanent deformations presented in the valve flap during the loading/unloading testing processes, since any permanent deformation would result in non-elastic response (Poiseuille's law world not be valid). Microscope inspection verified this after testing. This is due to the relatively small bending of the beams.

2.5.3 Dynamic Testing

The fabricated valve set was assembled in a similar way as depicted in Figure 2.16 with a piezoelectric pump at Kinetic Ceramic Inc. using a specifically designed valve holder for dynamic response characterization. Two sets of the microvalve array (Figure 2.14) were tested. The water was pumped against a blocking force and the increased pressure was measured. Test results showed that a measured pressure rose up to *350* psi when the pumping frequency was 10kHz. This is the highest pressure buil-up from a microvalve ever produced, based on the author's knowledge.

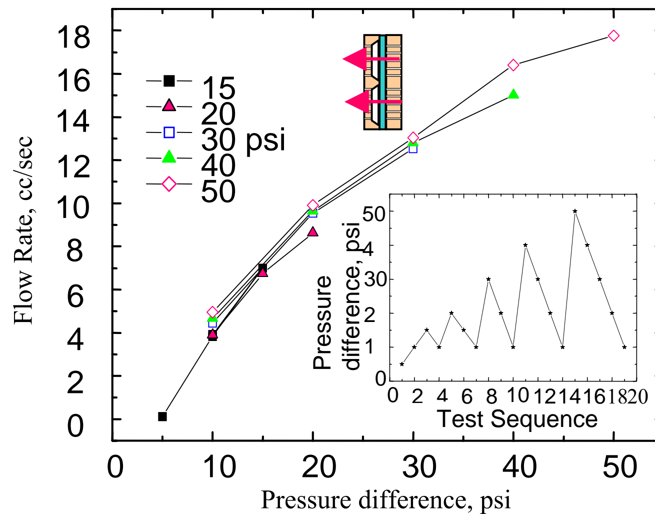

Figure 2.17: Repeat tests of flow rate under pressure differences applied (water)

2.6 Conclusion

A robust passive high frequencies, high pressure micro check valve has been developed for piezoelectrically actuated pumps or hydraulic actuators. The valve can support pressure up to 10 MPa due to a novel cross pattern designed on the valve flap. The valve's reliability is assured by using a mechanical valve stopper. The valve flap was fabricated with the electroformed nickel on silicon substrates. Deep RIE etching was used to fabricate the valve channels on silicon substrates as well as separate valve and valve stopper from silicon wafers. The whole valve array weighs 0.2gram including the packaging. The flow rate of the microvalve tested is about 18 cc/sec (DI water) under a pressure difference of 50 psi. No damage was identified during the repeated tests. Dynamic test results showed that the micro valve integrated with a compact piezoelectric pump can produce a pressure of 350 psi when operates at 10kHz. The developed micro mechanical passive valve array matches well to piezoelectric pusher's inherent material properties in terms of high actuating frequencies and large force support ability. The compact pump/hydraulic actuators integrated with the novel microvalve arrays will find broad applications in aerospace and deep space exploration for fluid management systems such as pumps and robust actuators where payload is critical, as well as other industry applications when miniaturization and robustness are important.

CHAPTER 3 LOW STRESS SU-8 PROCESS AND ITS APPLICATION FOR THE FABRICATING A NOVEL MICRO HEAT EXCHANGER

3.1 Introduction

SU-8 is an ultra-thick, high contrast, negative tone, epoxy based photoresist, which can be exposed by near UV lights. It is an excellent material for the fabrication of high aspect ratio [27,28] and vertical wall Micro-Electro-Mechanical Systems (MEMS). Thick layer up to several milimeters [29] can be achieved by a single spin coating. SU-8 has very high optical transparency above 360nm, which makes it ideally suitable for imaging near vertical sidewalls in very thick films. It is reported that an aspect ratio of 18 was achieved reproducibly with a single layer [30]. Because of its superior aspect ratio, vertical sidewalls and stable characteristics within a nickel–sulfamate & sulfate solution, SU-8 turns out to be an excellent molding material for the electroforming process. In addition, SU-8 has good physical properties and is also a good structure material for microstructures. The mechanical propertiessuch as Young’ smodulus and the ultimate strength (differ with processing) are measured by a newly developed tensile test method with the help of a MTS Tytron Microforce Tester (chapter 6).

However, using SU-8 in the fabrication of MEMS devices is greatly limited the large internal stress generated in the fabrication process and its poor adhesion on most metals, such as copper, gold, titanium and chromium, etc [28]. In order to overcome these problemss, a newly developed material by Microchem Inc., called Omnicoat, was applied to improve

adhesion of SU-8 on metallic layer. The parameters in the SU-8 process were refined for the fabrication of low internal stress, ultra-thick, high aspect ratio micro molds. A micro heat exchanger (a laminated structure) designed to operate at cryogenic temperature was then fabricated by this process, in which SU-8 works as the micro molds for nickel electroforming as well as the structural material for the thermal insulation layers. Even though nickel is not a good thermal conductor at room temperature, its thermal conductivity increases to 1250 W/k.m at cryogenic temperature (77K). Therefore nickel was chosen for the thermal conduction layer. The thermal conductivity of SU-8 is 0.2 W/m-K (general value for thermoplastic), making it ideal for thermal insulation. The laminated microstructure with stacked nickel and SU-8 for potential micro heater exchanger had been fabricated and passed the cryogenic test without structural damages.

3.2 Development of the SU-8 Process

SU-8 is a negative photoresist, good for fabricating pricise and stable patterns because of its good physical and optical properties as well as its stability in most chemicals. However, it is very difficult to produce fine thick SU-8 structures due to the large internal stress generated if following the process provided by the manufacturer, which will induce micro cracks (Figure 3.1) in the structures harming its mechanical strength and reliability or even completely distort the patterns. This situation could be worse if the SU-8 layer is being used on top of metallic layers. The SU-8 patterns may be totally peeled off due to the poor adhesion between SU-8 and the metallic layer by the large internal stress produced (Figure 3.2). So it is necessary to optimize the fabrication process to develop low stress, cracks free SU-8 patterns

for MEMS development. In order to overcome the adhesion problem, an Omnicoat layer is applied between SU-8 and the metallic layer to improve the adhesion. It also helps to remove the micro molds after nickel electroforming, because the Omnicoat is dissolvable in the SU-8 remover.

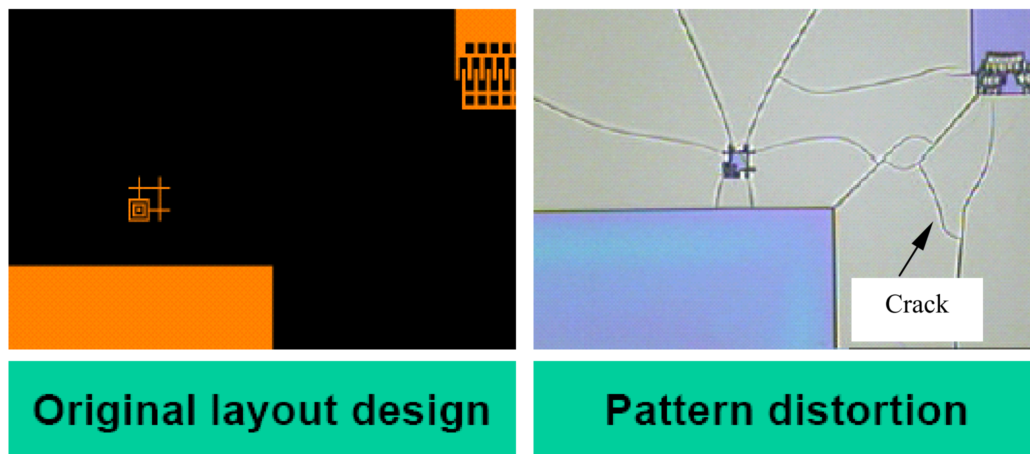

Figure 3.1: Distorted SU-8 pattern and cracks

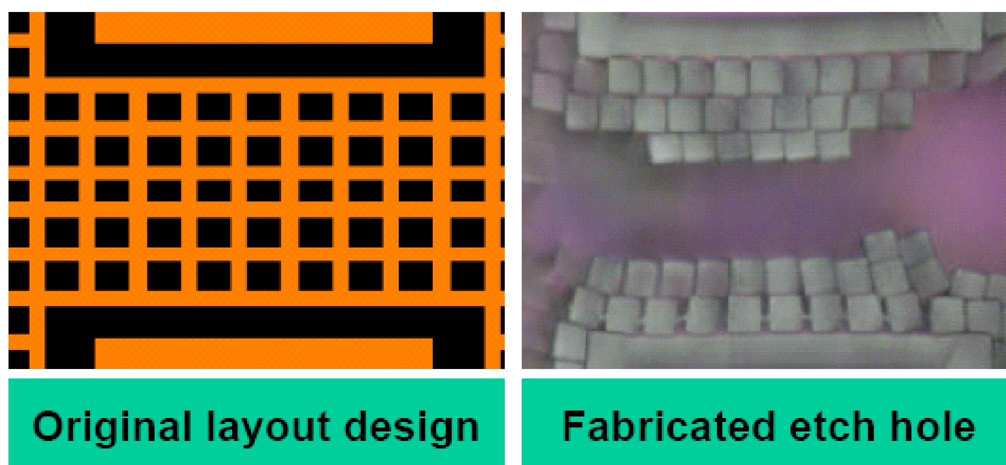

Figure 3.2: SU-8 pattern partially peeled off

3.2.1 SU-8 Process

The extra high internal stress in SU-8 after post exposure bake (PEB) is a critical problem for the application of thick SU-8. The major parameter to be controlled in order to reduce the internal stress is the amount of cross-linkage in the material after post exposure bake. Insufficient cross-linkage is good for stress and easiness of removal, but it will cause development failure and bad wall profile. Excessive linkage is good for fine pattern generation and good wall profile, but it will cause high film stress and difficulties to remove. Therefore the amount of linkage need to be balanced for a low stress, cracks free, high aspect ratio SU-8 process. The controllable parameters for this are the dose of exposure and the temperature & time of the post exposure bake. Also relaxation between steps is assigned to help to reduce the internal stress.

In this dissertational research, the author has conducted experiments to optimize the process, in terms of spin speeds, the soft bake time and temperature, the exposure time, the post exposure time and temperature and the relaxation time between steps. A process for low stress, high aspect ratio, and ultra thick SU-8 structures has been developed. In this process, the Omnicoat and SU-8 as well as the processing materials (Developer, Remover, etc) were purchased from Microchem Inc. SU-8 2150 was preferred to use in this research for thick coating because of its high viscosity. The Omnicoat layer and SU-8 layer were spun on by a conventional spinner (Model WS-400A –6NPP/LITE by Laurell Technologies Cooperation) and near UV exposed by a Karl Suss mask aligner with a power density of 13 mW/cm^2 for I-line (365 nm).

The detailed process for a 300 μm thick layer is listed below:

1. Spin on Omnicoat layer at 3000 RPM for 30 seconds by a conventional spinner;
2. Bake Omnicoat layer at 200 oC on a hotplate for 1minute;
3. Dispense 3 ml SU-8 2150 on a 3” wafer and spin coating at 1500 RPM for 30 seconds by a conventional spinner;
4. Relax at least 1 hour;
5. Soft bake at 65 ^{o}C for 15 minutes on leveled hotplate and at 95 ^{o}C for 8 hours (ramp temperature up and down slowly);
6. Relax 9 hours after soft bake at room temperature;
7. Remove bead in the edge;
8. Near UV exposure with contact aligner for 4 minutes;
9. Relax 30 minutes;
10. Post exposure bake at 55 ^{o}C for 2 hours (ramp temperature up and down slowly);
11. Relax for at least 24 hours;
12. Develop with Microchem developer for 30 minutes, rinse with IPA followed DI water and blow dry;
13. Etch by MF 319 to remove the uncovered Omnicoat;
14. Nickel electroforming;

Remove SU-8 mold by Microchem Remover PG at 90 ^{o}C for 30 minutes.

3.2.2 Discussions

The more than 1-hour relaxation time (step 3) just after the spin coating is used to allow the SU-8 to re-flow in order to get a flat surface as well as to eliminate the stress related to the spin coating step. A long time soft bake is used in this process on a leveled hotplate to completely vaporize the solvents and allow the trapped air bubbles to evolve out of the film, which results in a very smooth and bubbles free SU-8 coating. The relaxation step (5) is to reduce the stress due to SU-8 shrink. For step (7), the Bead Remover PG provided by the manufacture is not intended to use, which is designed to apply in the spin coating step. However, this didn't work well because the SU-8 reflowed when soft baking. The method used to remove the bead here is by a knife after soft bake with nitrogen blowing to remove the powders produced. For exposure, a much higher dose (8400 mJ/cm^2) is used intently to produce a strong acid in the SU-8, which makes it possible to link the SU-8 at low temperature in the post exposure bake step. After near UV exposure, the SU-8 is baked at low temperature (as low as 55 ^oC, which is much lower than the recommended temperature 95 ^oC). It is reported that most of the internal stress in the exposed SU-8 layer is produced in the post exposure bake step. The low temperature used in the post exposure bake (PEB) is to reduce the rate of heat enhanced SU-8 cross-linkage as well as to allow it to relax in the mean time, so that the internal stress is greatly reduced in this scheme. As a contrary, cracks and distortions are easy to identify in SU-8 patterns caused by large internal stress, if baking temperature is 95 ^oC (recommended by manufacture) or above. The IPA (isopropyl alcohol) used in the development step works well as an indicator for under developing if white spots

are observed when the SU-8 sample is rinsed by IPA as well as a solvent for the SU-8 Developer which is insoluble in water.

The fabricated SU-8 molds are shown in Figure 3.3. They are free of cracks under inspection of microscope and no distortions are identified. Good adhesion between SU-8 patterns and the copper seed layer has been achieved. This conclusion can be safely drawn from the fact that no SU-8 structures were peeled off from the seed layer after developing as well as in the process of electroforming. This is a very good method to test the SU-8 adhesion strength on silicon wafer due to its large coefficient of thermal expansion (CTE) which will cause an expansion mismatch between SU-8 and the substrate (such as Silicon or glass wafer with very small CET) when temperature increases (e.g. rinsing into nickel electroplating bath with a typical temperature of 55 ^{o}C). This mismatch will induce a large shear stress in the interface, causing peeling off of the SU-8 pattern from the substrate in case of a weak adhesion. This also indicates that the internal stress in the SU-8 layer is reduced to an acceptable level.

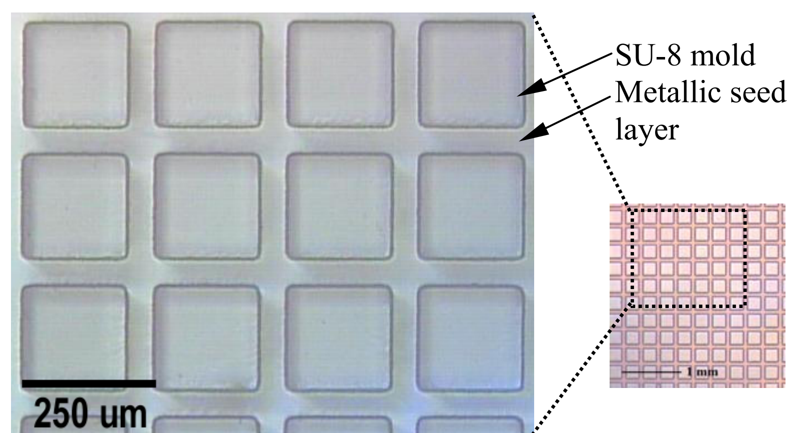

Figure 3.3: A 250 µm thick SU-8 mold for a nickel mesh like structure with 2704 squares columns (200 µm by 200 µm) in an area of 1.7 cm^2 (1.5 cm by 1.5 cm)

3.3 Design of the Micro Heat Exchanger

The designed micro heat exchanger is a sandwiched structure, as shown in Figure 3.4, in which heat carrying liquid flows through an array of micro channels formed by laminated layers consisting of thermal conductive layers (nickel) and thermal insulation layers (SU-8). The heat can be dissipated quickly through the nickel layer, as a short distance between the boundaries. Nickel is a good thermal conductor at cryogenic temperatures. Its thermal conductivity is 90.7 W/m-K at room temperature and 1950 W/m-K at 15K. A good heat-exchanging efficiency is expected at cryogenic temperature.

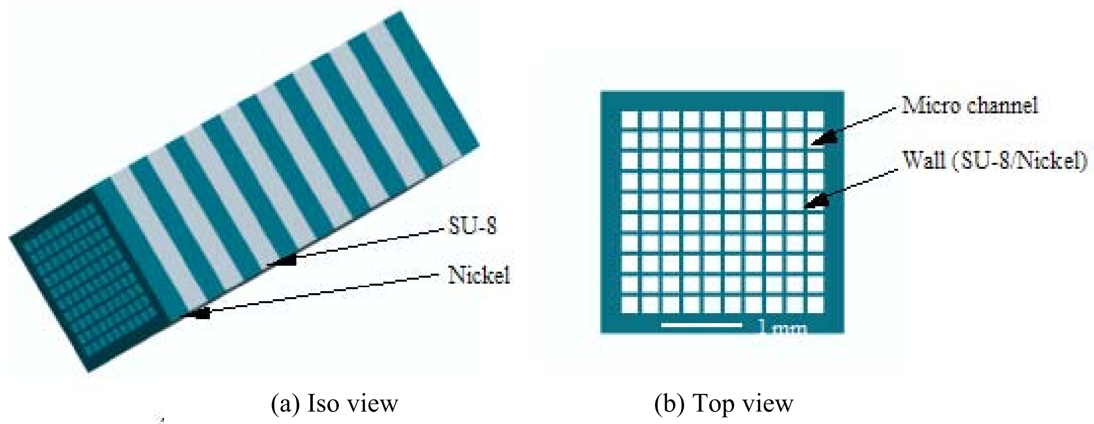

(a) Iso view (b) Top view

Figure 3.4: Sketch of the micro heat exchanger

As shown in Figure 3.4, for a heat exchanger having a cross section of 1.5 cm by 1.5 cm, it houses an array of 2704 micro channels with dimension of 200 μm by 200 μm and the wall thickness of 50 μm. The thickness of each layer is 300 μm. In this design, square-shaped micro channels are preferred for the reason of increasing the space usage comparing to circular shaped channels. The nickel layers (thermally conductive) will be electroformed with

SU-8 molds. The adhesion between the SU-8 mold and the seed layer (Cu/Cr) layer will be greatly improved by using Omnicoat (purchased from Microchem Inc.). In this process, SU-8 works as molds for nickel electroforming as well as thermal insulation layers.

Finite element simulation was performed to find the maximum stress developed in the micro heat exchanger upon operation. As the structure is fabricated at room temperature and there will be a great temperature gradient when one end of the heat exchanger accesses to a cryogenic temperature. For temperature changing from room temperature to 77K, a temperature gradient of 2.5 k per nickel layer will be produced in the structure. This temperature gradient is used for the FEM simulation. The properties adopted in the simulation are from the mechanical testing as well as from [31,32,33] and listed in table 3.1

Table 3.1: Properties used for heat exchanger simulation

Property	Nickel (bulk)	SU-8
Modulus of Elasticity	207 GPa	2.5 GPa
Poisson's Ratio	0.31	0.22 [19-21]
Tensile Strength, Ultimate	317 MPa	50 Mpa
Coefficient of thermal expansion (CTE)	13.1 µm/m-°C	21 µm/m-°C [19-21]

The simulation results of a five-layer sandwiched structure (consisting three nickel layers and two layer of SU-8) are illustrated in Figure 3.5. Only one half of the structure is analyzed because of the symmetric geometry. The results show that the maximum stress is 10.7 Mpa, located in the interface between nickel and SU-8 layers. This stress is by no means large, which won't cause the structure to fail if proper bonding between layers is achieved.

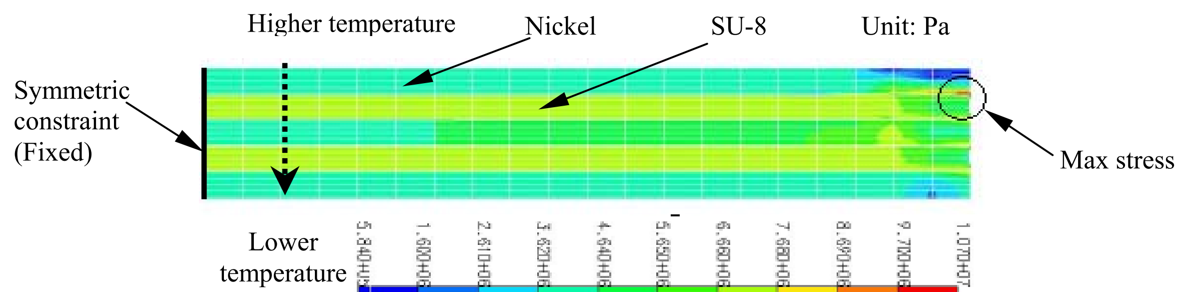

Figure 3.5: Stress distribution of the micro heat exchanger

3.4 Fabrication

The fabrication process is a UV-LIGA compatible electroforming process, in which nickel patterns were formed firstly by using SU-8 molds, then these molds were removed and finally the structural SU-8 patterns were patterned on top of the nickel structures. Therefore, this is a bottom-up self-assembled fabrication process.

3.4.1 Process Flow

The process flow is shown in Figure 3.6. The process begins with cleaning the 3-inch silicon wafer, followed by thermal evaporation of chromium and copper seed layer for nickel electroforming. Then a very thin layer of Omnicoat is coated on the copper layer and then

baked. A thick SU-8 2150 layer is spun on top of the Omnicoat layer and patterned to form the micro molds for nickel electroforming. The SU-8 mold is completely removed by the SU-8 Remover PG after nickel electroforming is finished. Finally, another SU-8 layer is deposited and patterned on top of the nickel structure to form the thermal insulation layer. So, a double layer is formed. Thick structures can be achieved by bonding more double-layer structures together to form the heat exchanger. The function of the Omnicoat layer is to improve the adhesion of SU-8 layer to the Copper seed layer as well as helping to strip off the SU-8 layer after electroforming.

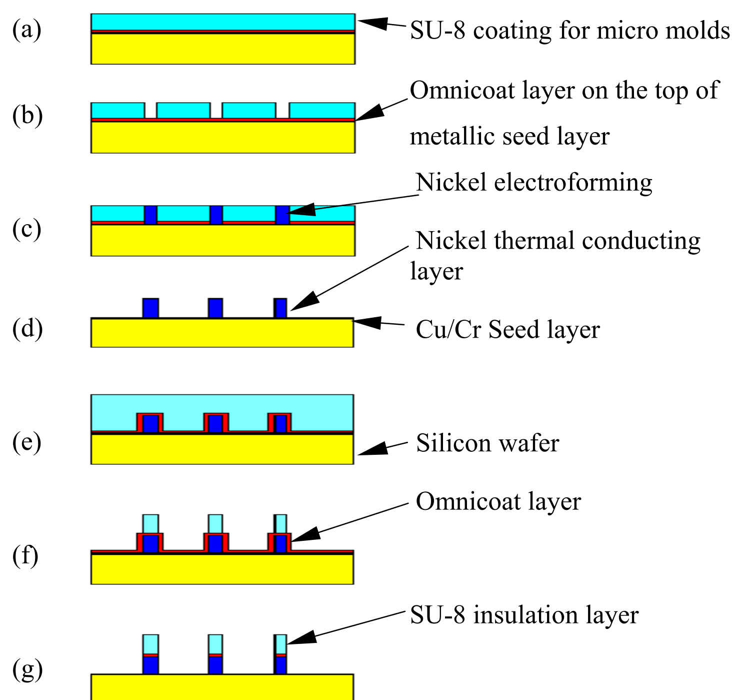

Figure 3.6: Fabrication process flow for the micro heat exchanger. (a) Coat and bake Omnicoat layer followed by SU-8 spin on coating after seed layer evaporation;

(b) Pattern and develop SU-8 layer and then develop Omnicoat layer;(c) Nickel electroforming; (d) Remove SU-8 mold and Omnicoat layer; (e) Coat and bake second Omnicoat layer and SU-8 layer; (f) Pattern and develop SU-8 layer; (g) Develop Omnicoat

3.4.2 Nickel Electroforming

The nickel thermal conductive layer is plated in a modified Watts bath, which contains Nickel Sulfate 300 g/L, Nickel Chloride 25 g/L, Boric Acid 40 g/L, Saccharin 0.1 g/L, X-100 0.01 cm^3/L. The PH value of the solution is kept at 4.0~4.5. A plating rate of 1 μm/min is achieved by maintaining the current density at 50 mA/cm^2 [4,34,35]. The temperature of the solution is kept at 55 ^oC by a hotplate, magnetically and air stirred. It is important to carefully adjust the pH, the amount of saccharin in the bath to get low internal stressed electroformed nickel layer. The SU-8 mold and the plated nickel are both 300 μm thick. The plated nicked structure is shown in Figure 3.7.

3.4.3 Fabricated SU-8/Nickel Sandwiched Structure

The SU-8 micro molds are completely removed by the Remover PG with the help of Omnicoat. Then, another SU-8 layer is deposited on the wafer after the remained nickel structure is cleaned by IPA and DI water and coated with Omnicoat. The second SU-8 layer is then baked, exposed and developed. And finally, double-layered structures are achieved. The SU-8 and Nickel sandwiched structure is shown in Figure 3.8. There is no delamination identified under microscope inspection. This suggests that the adhesion between SU-8 layer and the nickel layer is very good. This structure is then removed from the silicon wafer and no deformation was found.

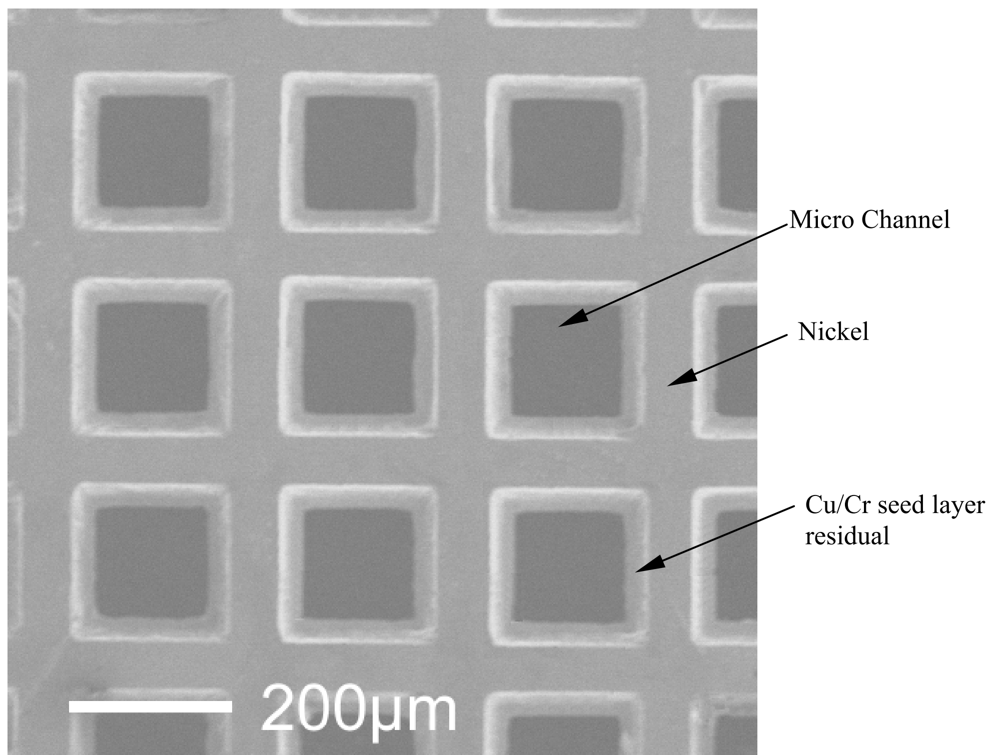

Figure 3.7: Top view of nickel thermal conductive layer with thickness of 300 µm

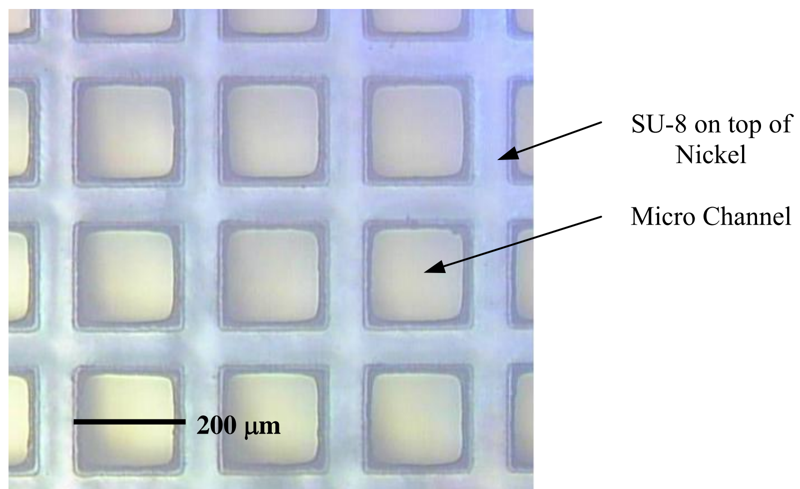

Figure 3.8: Top view of SU-8/Nickel sandwiched structure

3.5 Testing

To test its temperature enduring capability, the fabricated SU-8/Nickel sandwiched structure was immersed into liquid nitrogen (about 77K) directly from room temperature. After certain time (5 minutes), the structure was taken out to room temperature for observation. By inspection under microscope, no damages (cracks or delamination) were identified (Figure 3.9).

The microstructure after testing is shown in Figure 3.9. There is no crack developed in the SU-8/Nickel pattern and the adhesion between SU-8 and nickel layer is still good. Comparing to Figure 6, the tested structure is still in good shape and no deformation is found. This means that this laminated structure and the materials chosen can stand cryo temperature without damages, same as simulation results indicated in Figure 3.3.

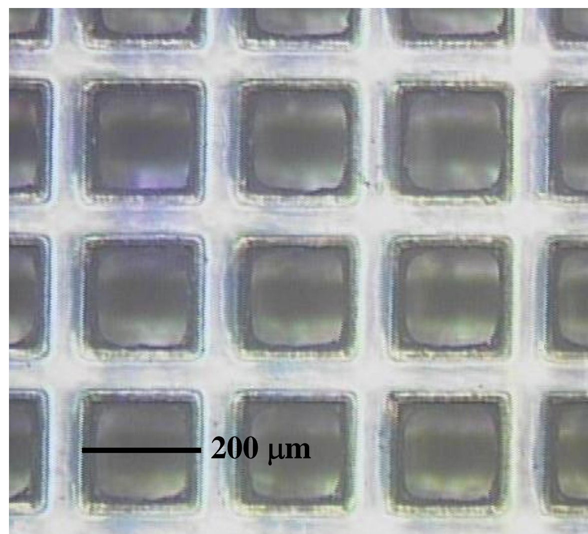

.

Figure 3.9: Top view of the tested sandwiched structure

3.6 Discussions and Conclusions

SU-8 is a very important material for fabricating thick vertical-wall micro patterns with sample equipment and low cost. However, large internal stress is often produced during the fabrication process as well as the poor adhesion between SU-8 and metallic layers, which causes deformation or mechanical failure of the devices. Therefore, a UV-LIGA process targeting low stress ultra-thick high aspect ratio SU-8 structures is newly developed by our group and the adhesion failure problem between SU-8 and metallic layers is sucessfully solved by applying a Omnicoat layer between the two layers. The mechanical properties of the SU-8 fabricated by this process are tested with Young’smodulus of about 2.5 Gpa and an ultimate strength of about 50 Mpa.

With the help of this process, a laminated (sandwiched) micro heater exchanger was successfully fabricated with patterned SU-8 as micro molds and electroforming process to generate electroformed nickel as thermal conductive layer, since nickel has very high thermal conductivity at cryogenic temperature. SU-8 layer is patterned on top of the nickel structure to form the thermal insulation layer. By careful processing the SU-8 layer and the help of Omnicoat layer, the adhesion between SU-8 and metal is greatly improved. The fabricated SU-8 molds are free of cracks and show very good adhesion to the seed layer. The patterned SU-8 structural layer also sticks tightly to the nickel layer.

The SU-8/nickel sandwiched structure passed the test in liquid nitrogen and no damages and deformations were observed, after taking out to room temperature. This verified the

simulation results that the nickel/SU-8 micro heater structure can stand at cryogenic temperatures (77K).

CHAPTER 4 DEVELOPMENT OF IN SITU ASSEMBLED SOLID NICKEL MICROVALVES

4.1 Introduction

As described in chapter 2, the author has successfully developed compact microvalve array for robust hydraulic pumps. However, when considering real applications where large dynamic loads are subjected, the silicon used may be a problem. This device needs carefully handling; otherwise it is easy to break because of its brittleness (silicon). Figure 4.1 shows a broken valve crushed by the valve holder when testing.

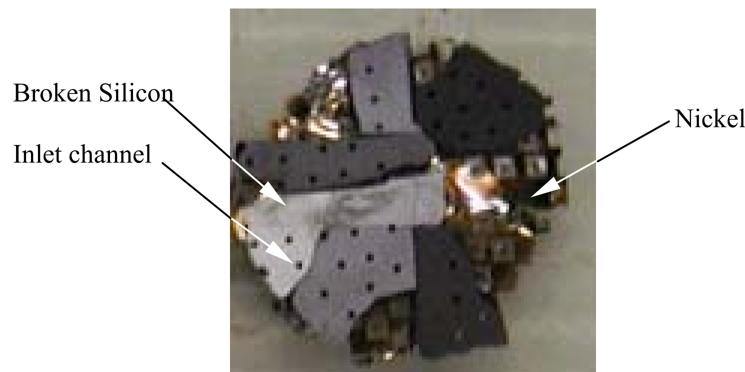

Figure 4.1: A broken silicon-nickel valve

Therefore, it is needed to develop a more robust compact microvalve array for large dynamic loads as well as easiness of handling. For this purpose, a self-assembled solid nickel valve was developed and tested. A micromachined thick nickel substrate and stopper were used to substitute the silicon substrate and stopper, respectively. Micro channels were formed into the nickel substrate and stopper using SU-8 molds. The stopper was aligned to the valve array

using an in situ UV-LIGA fabrication process. Thick (SU-8) and thin photo resist were used as the sacrificial layers during the valve fabrication. SU-8 molds are also used to separate the electroformed nickel valve from the substrate such that clean-edged valves will be received after removing all sacrificial materials.

4.2 Valve Design

The microvalve and the pump are shown in Figure 4.2. The valve array contains 80 single valves with the stopper automatically aligned to the valve array during fabrication. The whole dimension of the valve is 12 mm in diameter with total thickness of 1 mm. Each microvalve consists of three parts (Figure 1 c), which are the bottom substrate containing the inlet channels, the valve flap sitting above and the top substrate as the valve flap stopper and outlets. The thickness of the bottom and the stopper is 500 μm. The inlet channels (Figure 1 c, Figure 2 c) are 200 μm in diameter. Outlet channels are 200 μm and 400 μm in diameter, respectively (Figure 2 d). Both inlet and outlet channels are defined by SU-8 molds, which are also used to separate the valve set from its surroundings.

A copper sacrificial layer made by physical vapor deposition (evaporation or spurting) with thickness of 0.2 μm is employed to define the gap between the flap and the bottom substrate as well as serving as seed layer for flap electroforming. The bottom of the stopper is 10 μm higher than the flap, which is defined by a sacrificial layer (photoresist).

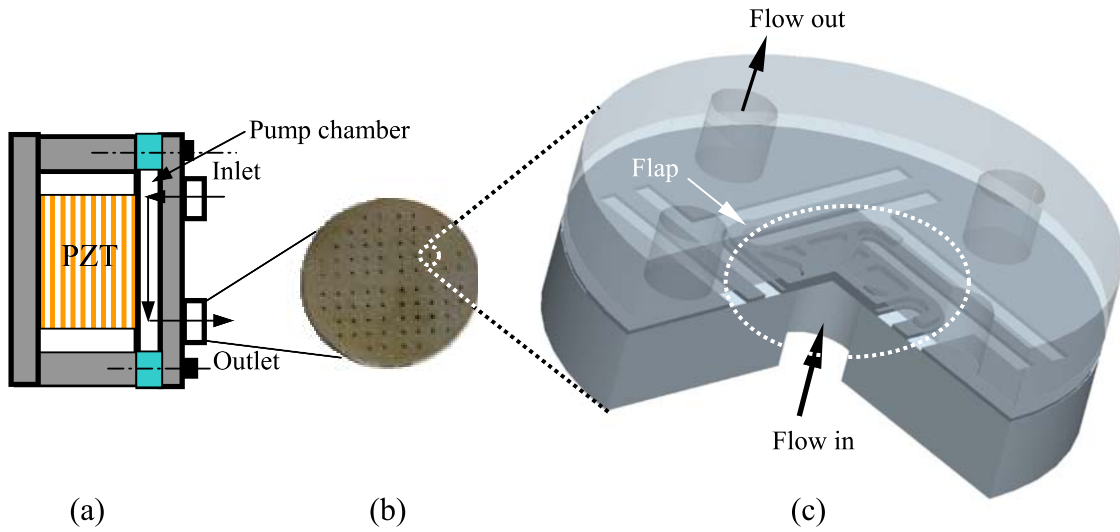

Figure 4.2: Robust pump and valve. (a) pump (b) valve array (c) concept sketch of the valve

The details of the valve flap are shown in Figure 4.3. The dimensions of the valve flap and beams as well as those of cross were optimized to reduce the stress. The double-layered valve flap with a total dimension of 300 μm x 300 μm is employed to open and close the valve. The bottom layer is 10 μm thick while the top layer is 15 μm thick. Comparing to the silicon-nickel valve described in chapter 2, this valve flap is strengthened while keeping the total mass of the flap small. This helps to maintain a high resonant frequency of the flap as well as assisting to overcome any stiction problem when the flap is lifted by opening pressure and contacts with the stopper thereafter.

Four micro beams are designed to hold the flap elastically. Their dimensions are 600 μm x 50 μm x 10 μm, longer than those of the silicon-nickel valve. This change helps to decrease the stress

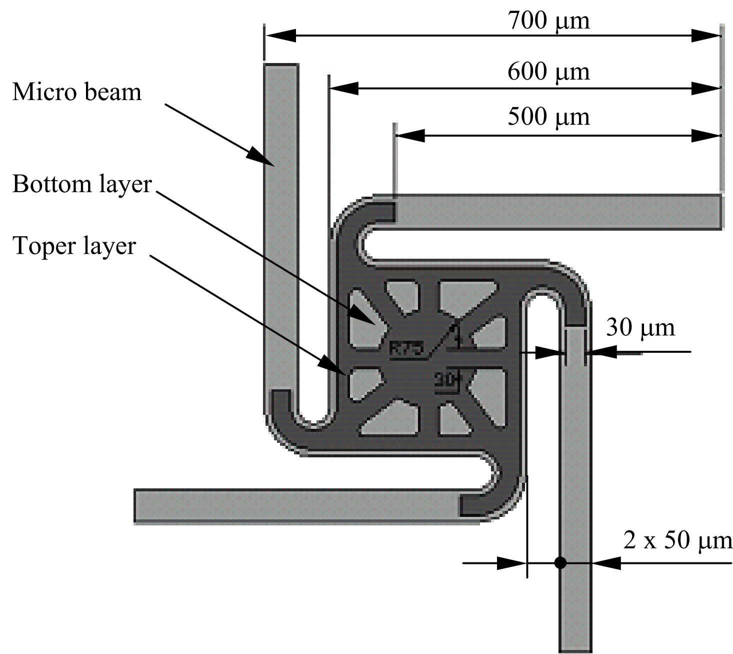

Figure 4.3: Concept sketch of the valve flap (top view)

4.3 Stress Analysis

Stress analysis was performed to find out the location and value of the maximum stress. First of all, the 1st mode resonant frequency was simulated by running mode analysis in I-DEAS, which is 18 kHz.

4.3.1 Stress on the Flap When It Is Fully Opened

The stress distribution in the valve flap was modeled by finite element analysis. In the open state, the beam-ends were fixed and pressure difference was applied to the bottom of the flap to lift it. For easy comparison, the deflection of the flap was kept at 6 μm, which is the same

value as used in chapter 2. The stress distribution is shown in Figure 4.4. The maximum von misses stress is 128 Mpa located in the beams, which is 32 percent lower than that of silicon-nickel valve (Figure 4.5). Higher-pressure difference will produce larger flap displacements, which will be sustained at 10 µm by valve stopper in case such a pressure difference is applied that it is capable of producing a displacement larger than 10 µm if the stopper is not present. In this way, the valve can support pressure up to 10 Mpa without damages.

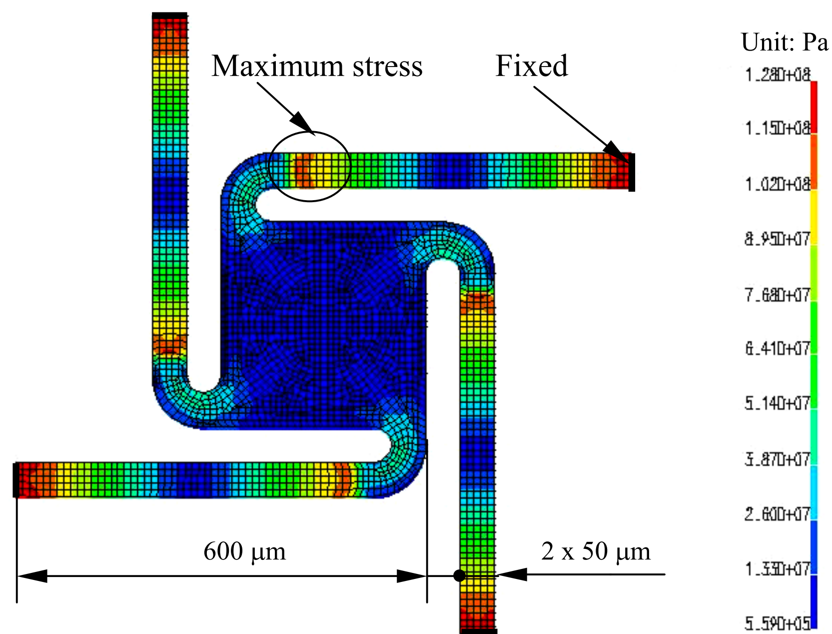

Figure 4.4: Stress distribution over microvalve flap while it is fully opened

4.3.2 Stress on the Flap When Closed

As mentioned in chapter 2, the valve needs to support pressure larger than 6 Mpa when closed. Therefore a pressure difference of 10 MPa is applied to the flap when it is closed with all the beam-ends fixed. The stress distribution is presented in Figure 4.6. The maximum von

misses stress is 132 Mpa, which is 34 percent lower than that of a silicon-nickel valve (Figure 4.7).

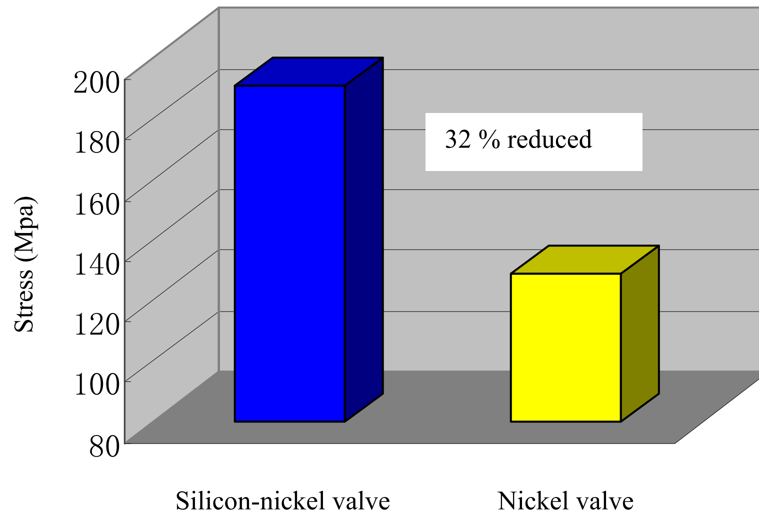

Figure 4.5: Comparing of maximum von misses stress between silicon-nickel valve and solid nickel valve when fully

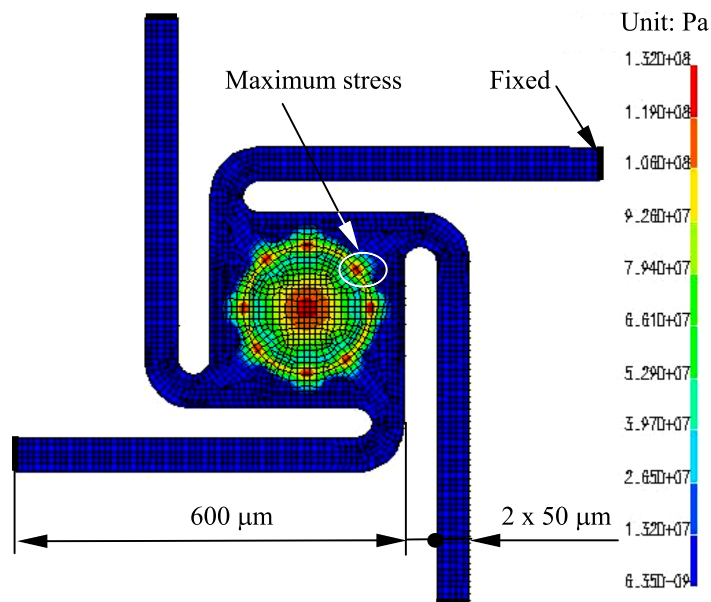

Figure 4.6: Stress distribution over microvalve flap while it is closed

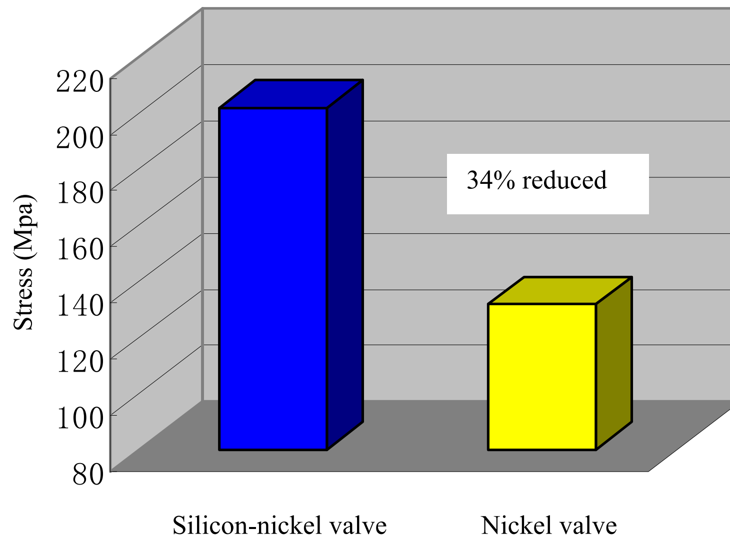

Figure 4.7: Comparing of maximum von misses stress between silicon-nickel valve and solid nickel valve when closed

4.3.3 Stress in the Nickel Bottom Substrate

Because the nickel bottom substrate (0.5 mm thick) would support pressure, the stress analysis was performed to find the maximum stress. Due to geometric symmetry, only one quarter of it was analyzed. A pressure difference of 10 Mpa was applied to one side of the nickel piece. The results are shown in Figure 4.8. The maximum von misses stress identified is 119 Mpa, which is 34 percent lower than that of silicon-nickel valve (Figure 4.9). This value is in the safe range of the nickel material used. The use of nickel as the supporting substrate overcomes the brittleness of the silicon substrate of the silicon-nickel valve. This valve is much easier to handle either in the process of fabrication or in post services.

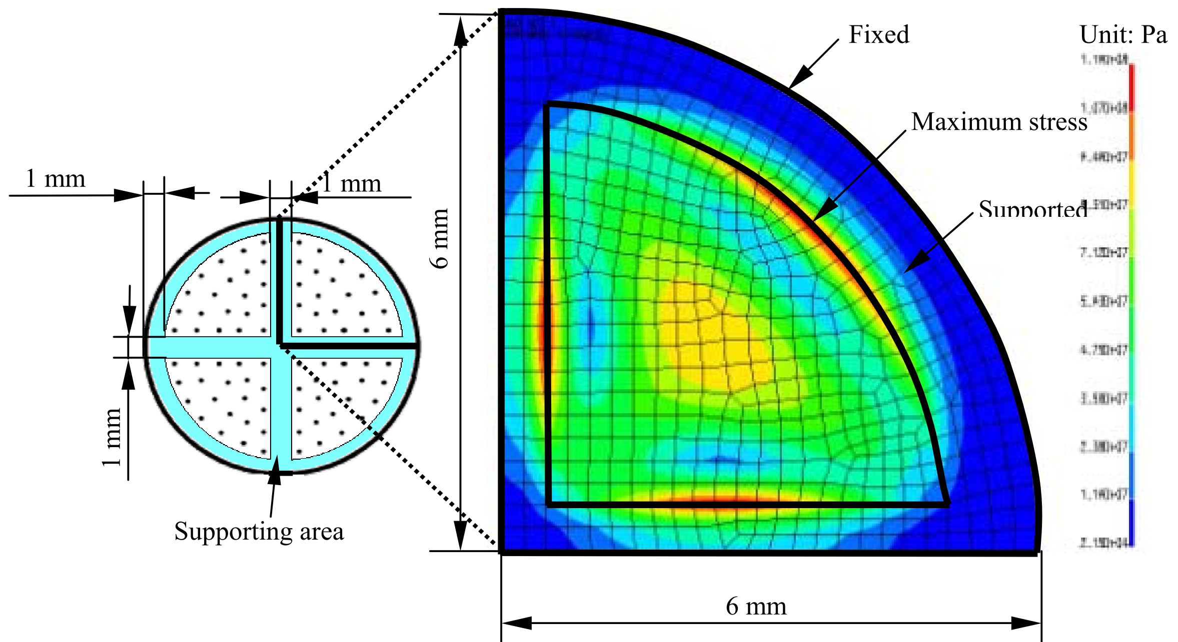

Figure 4.8: Stress distribution of nickel substrate under 10 MPa pressure while closed

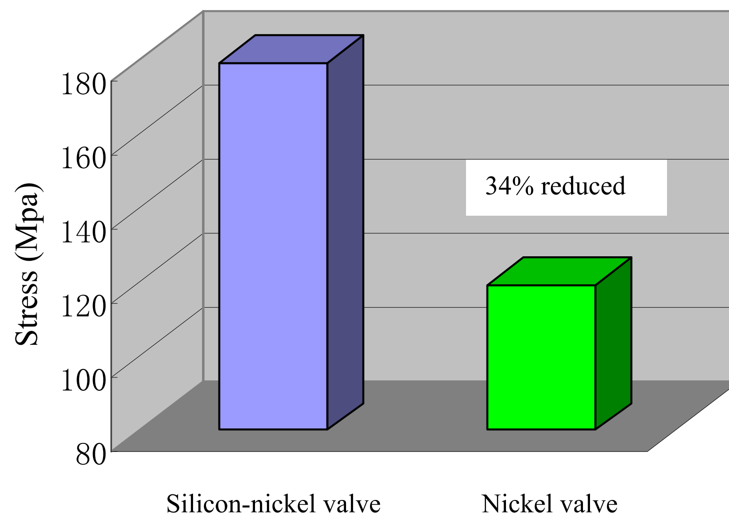

Figure 4.9: Comparing of maximum von misses stress in supporting substrate between silicon-nickel valve and solid nickel valve when closed

4.4 Fabrication Process

The fabrication of the compact microvalve array has been completed by an in situ UV-LIGA process. The valve inlet and outlet channels are defined by SU-8 molds. The valve flaps are defined by Photoresist molds. Chemical mechanical polishing (CMP) has been applied during the fabrication. After electroforming, all SU-8 and photoresist molds are removed by using SU-8 remover. Finally, separated valve arrays are received. Therefore, this is a bottom–up self-assembled fabrication. Neither etching nor bonding (or packaging) is involved during the fabrication.

The fabrication process begins with evaporating or spurting a Cu/Cr seed layer and then photoresist (Shipley 1813 or AZ 4620, 12 μm thick) is spun on and patterned with UV lithography technique to form micro molds for the valve flap and the beams (step A and Figure 4.11). A 10 μm thick nickel layer is electroformed to generate the valve flap and micro beams (Figure 4.10), which are defined by the photoresist micro molds (step B).

The thickness of the nickel layer is controlled by current density and plating time. In this case, it was plated with current density of 10 mA/cm^2 for 50 minutes. A nickel sulfamate solution (table 4.1) was adopted in this process, which has the ability to produce stronger nickel structure than the traditional Watts nickel solution.

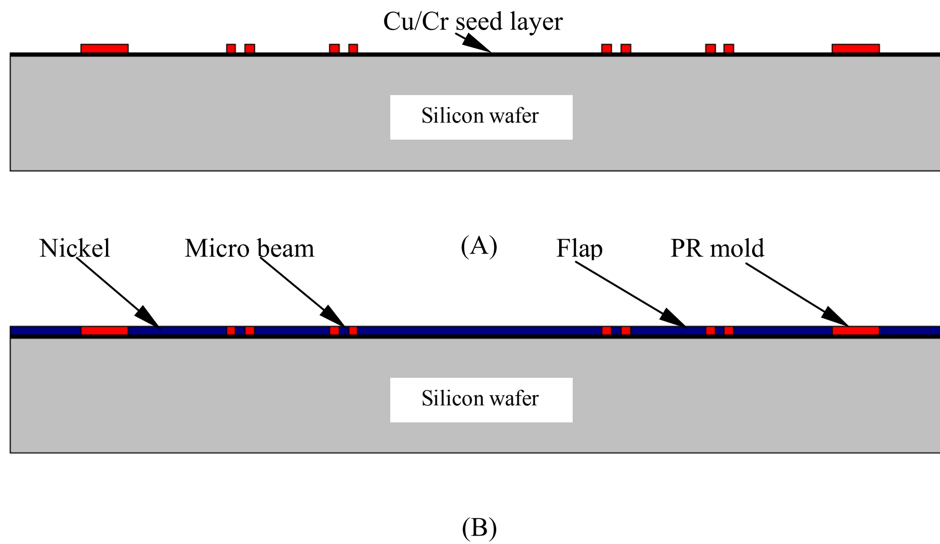

(B)

Figure 4.10: Sketch of fabrication process step (A) & (B). (A) Seed layer deposition and PR molds patterning (B) Electroforming for valve flap and beams.

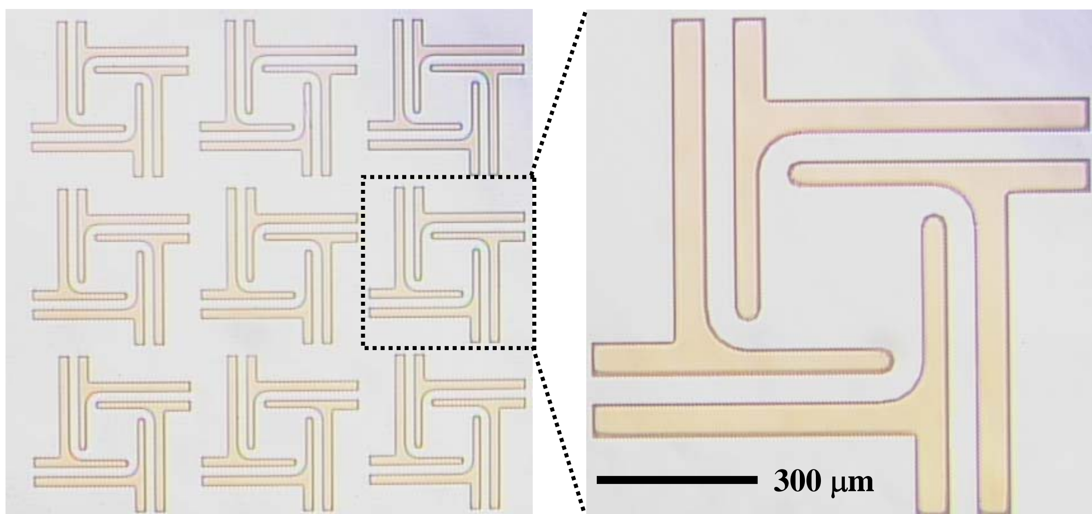

Figure 4.11: PR molds (12 μm thick) for valve flap and micro beams

Table 4.1: Operating conditions for electrochemical deposition schemes (nickel sulfamate solution)

Constituent/condition	Concentration (/L)/value
Nickel sulfamate ($Ni(SO_3NH_2)_2$_4 H_2O)	1.54 M
Boric acid (H_3BO_3)	0.73 M
Sodium dodecyl sulfate (SDS)	0.1 g
Saccharin	0.1 g
Operating temperature	60 °C
PH	3.5-4.0
Current density (mA/cm^2)	10-25

Next (step C, Figure 4.12), a thin layer of copper was evaporated or spurted on top of nickel layer and then patterned by the copper etchant to form sacrificial layer covering the valve flap and the micro beams. This is used to define the gap (0.2 μm) between valve flap and its bottom substrate. Then SU-8 molds (Figure 4.13) are patterned on top of copper sacrificial layer to define the inlet channels. Electroforming was then conducted to form the supporting substrate and the inlet channels (step D).

The copper etching solution used in step C acts as a redox etchant, which contains $CuSO_4 \cdot 5H_2O$ (15g/L) and NH_4OH (30% by wt) 300ml/L. The reason for choosing it is that it doesn't etch nickel. The measured etching rate is about 2500 $\overset{o}{A}$ to 3000 $\overset{o}{A}$ per minute.

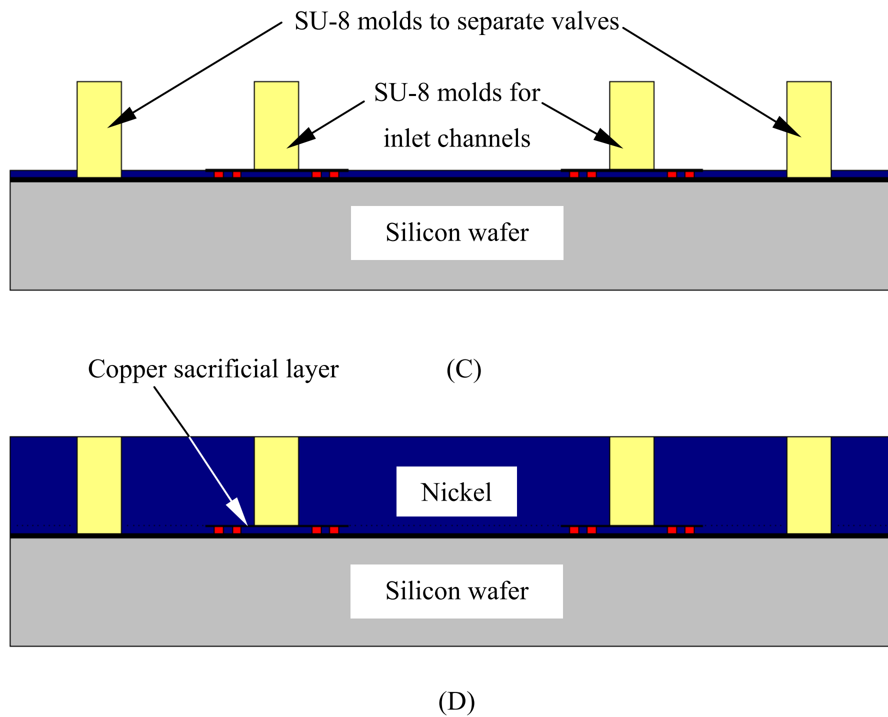

Figure 4.12: Sketch of fabrication process step (C) & (D). (C) SU-8 molds patterning (D) Electroforming for nickel substrate and inlet channels.

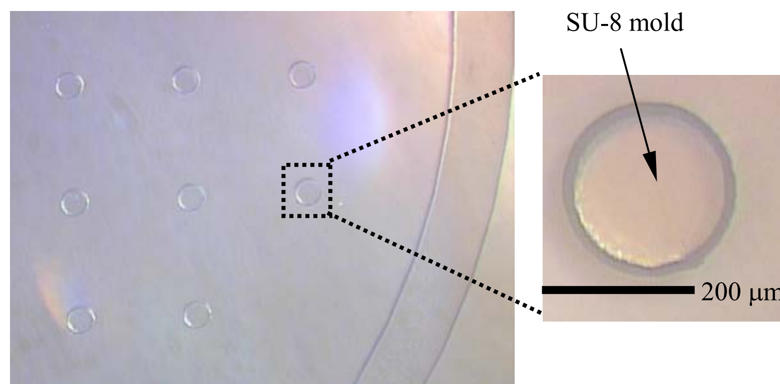

Figure 4.13: SU-8 molds for inlet channels

After electroforming, the thick nickel layer was polished to remove any higher points and thus makes the surface flat. In this step, an automatic polisher is employed with alumina

slurry. Then, the nickel & SU-8 structure was released by 30% KOH solution operating at 80 °C (step E). Copper etchant was applied to remove the Cu/Cr seed layer followed by a cleaning step. This will remove the photoresist molds for flap and micro beams. Then, the nickel & SU-8 structure was flipped over and photoresist molds (Shipley 1075 or AZ 4620, 18 μm thick) were patterned on its top for the top layer of the flap (Step F).

The top layer of the flap was then electroformed through PR molds (step G, Figure 4.15). The finished microvalve array and valve flap are shown in Figure 4.16 and 4.17, respectively. Another layer of photoresist (10 μm thick) was then applied to define the gap between the stopper and the flap. This PR layer was metalized by evaporating or spurting a thin layer of copper on it and patterned by the copper etchant to serve as the seed layer for the stopper (step H).

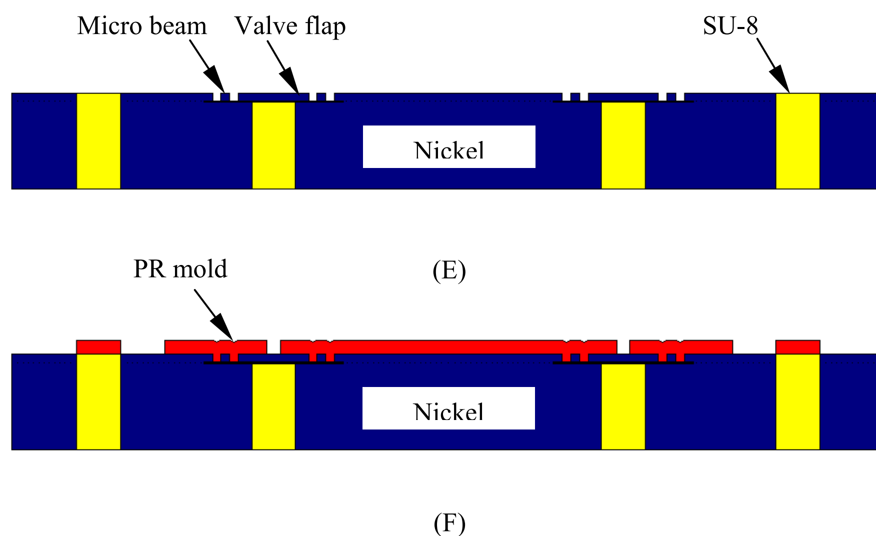

Figure 4.14: Sketch of fabrication process step (E) & (F). (E) Release nickel & SU-8 structure from silicon wafer (F) Pattern PR molds for top layer of the flap

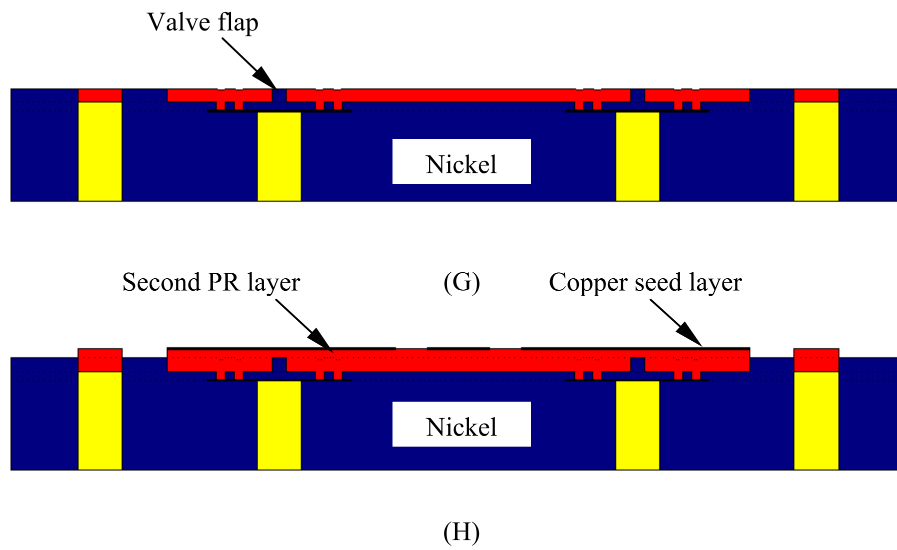

Figure 4.15: Sketch of fabrication process step (G) & (H). (G) Electroforming for the top layer of the flap (H) Pattern PR molds for defining the gap between flap and stopper

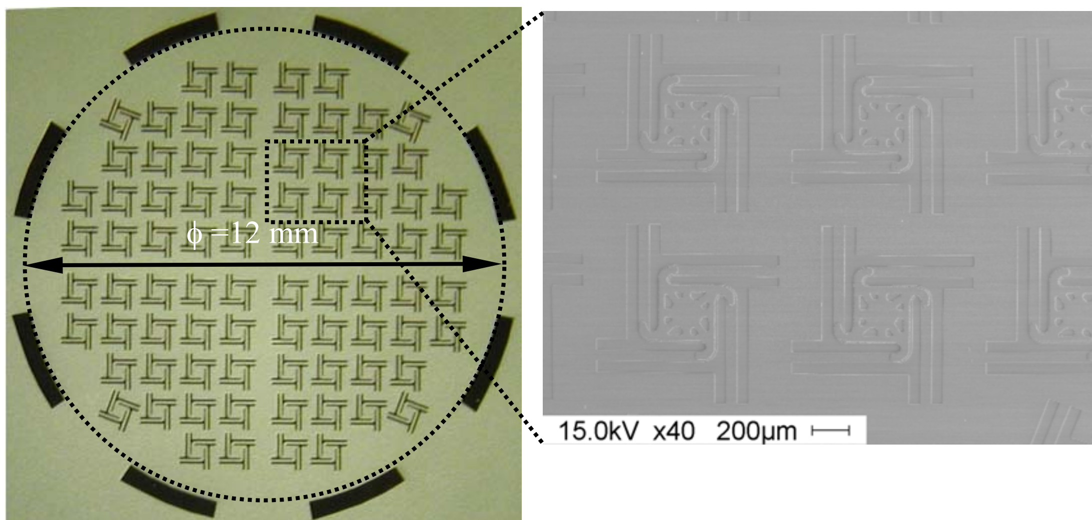

Figure 4.16: Fabricate microvalve array (80)

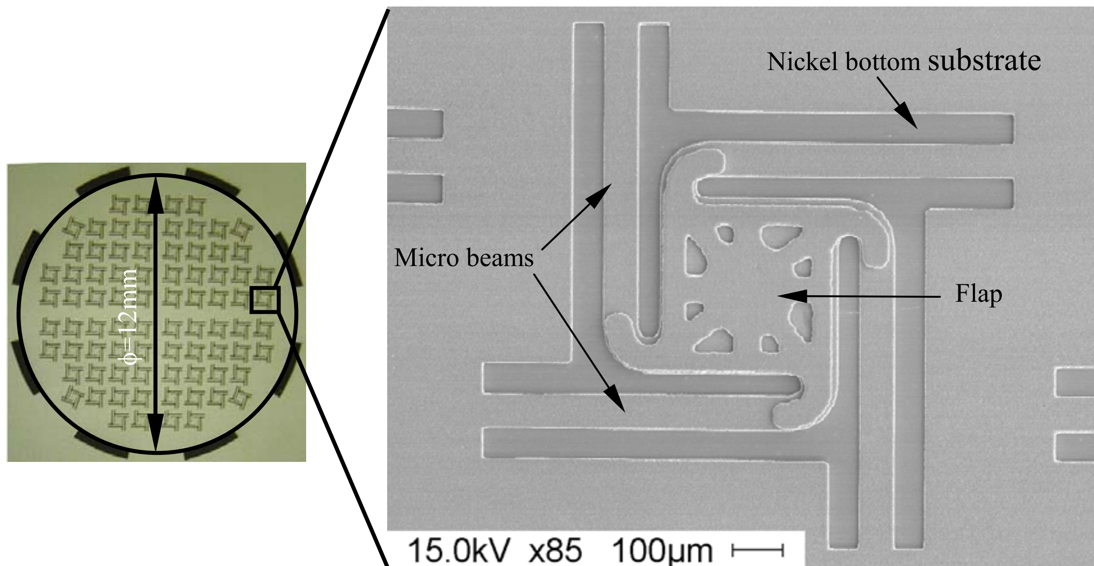

Figure 4.17: Finished micro flap with total thickness of 25 µm

A nickel layer (10 µm thick) was plated over the copper seed layer for the following SU-8 process, in which the shrink force will cause the copper seed layer peel off if SU-8 is applied on top of it directly (step I, Figure 4.18). Next, all the photoresist was removed by acetone to avoid its confliction problem with SU-8 (step J, Figure 4.18). Then a SU-8 thick layer was applied and patterned to define the stopper & outlet channels (step K, Figure 4.19). The stopper (500 µm thick) was formed through SU-8 molds (step L, Figure 4.19) with electrochemical deposition. After electroplating, polishing was applied to make the surface flat. Finally, all the SU-8 molds were removed by SU-8 remover @ 90 °C, followed by copper etching to remove interior copper materials (step M, Figure 4.20).

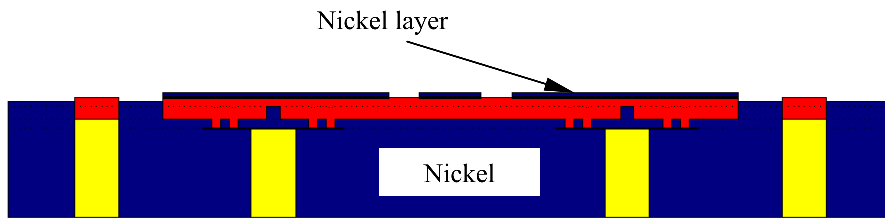

(I)

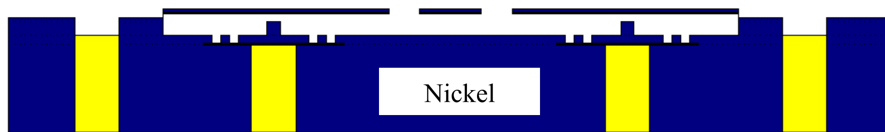

(J)

Figure 4.18: Sketch of fabrication process step (I) & (J). (I) Electroforming for the nickel thin film (J) Removal photoresist

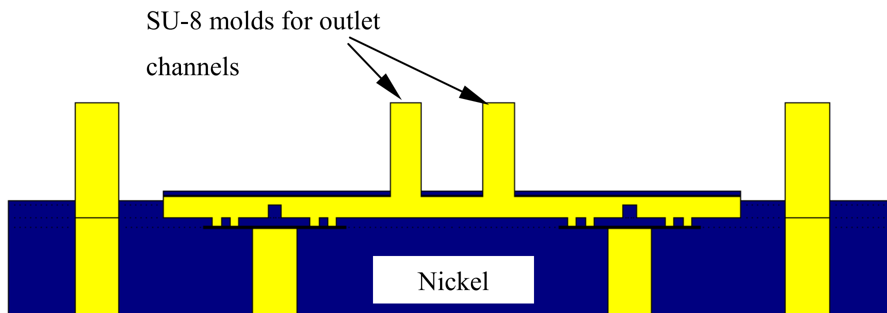

(K)

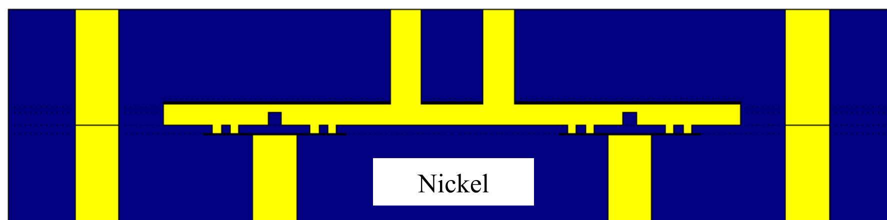

(L)

Figure 4.19: Sketch of fabrication process step (K) & (L). (K) SU-8 molds for stopper & outlet channels (L) Electroforming for stopper

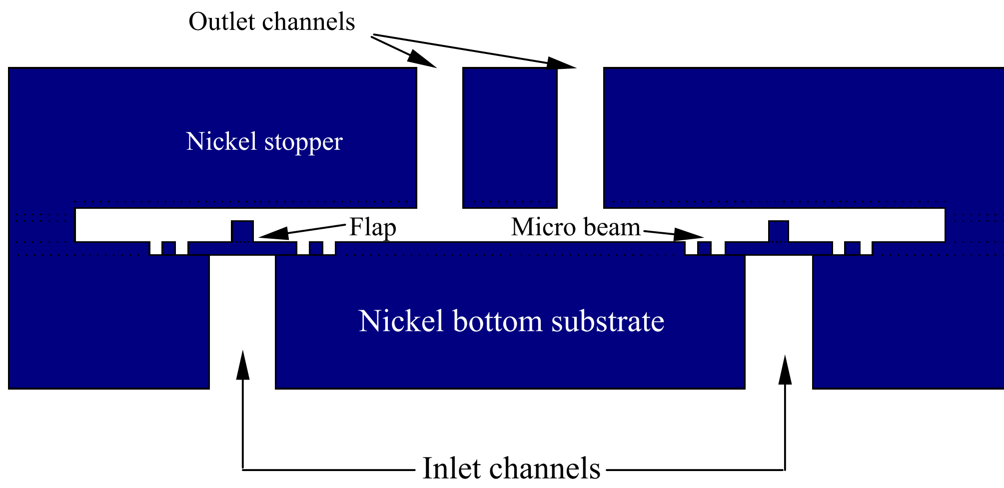

Figure 4.20: Final released structure

The final fabricated valve is shown in Figure 4.21, with scanning electron microscopy (SEM) pictures showing the details of the inlet (Figure 4.22) and outlet (Figure 4.23), respectively.

Figure 4.21: Finished nickel valve (a) Inlet (b) Outlet

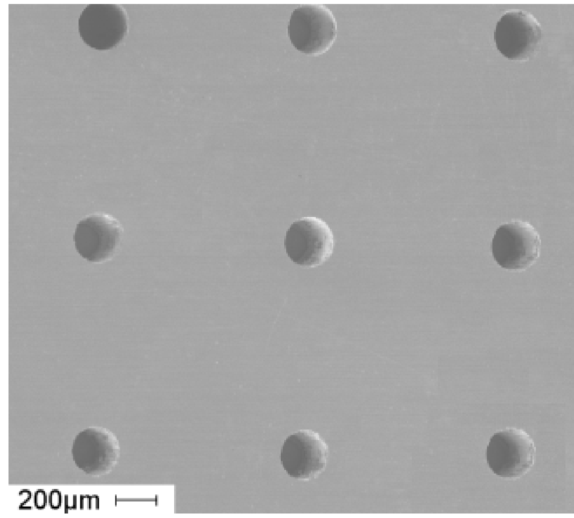

Figure 4.22: SEM picture of valve inlet (tilted for 25 degree)

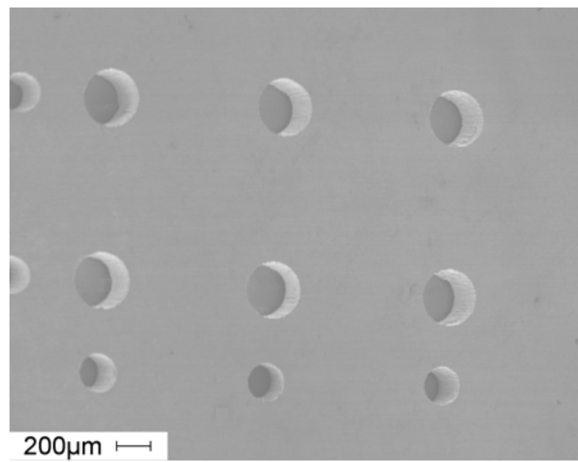

Figure 4.23: SEM picture of valve outlet (tilted for 25 degree)

4.5 Flow Rate Measurement

For the characterization purpose, the flow rate of the microvalve with an array of 80 single valves was measured under difference pressure. A fluid system (Figure 4.24) was developed, which contains a compressor, a liquid tank, pressure gauges, a flow meter, a filter and a valve holder for the microvalve fabricated.

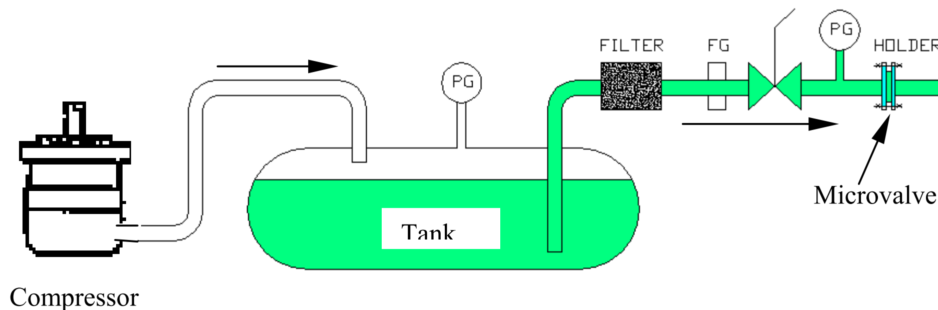

Figure 4.24: Scheme of flow rate measurement system

The valve array was housed by a specifically designed valve holder as described in chapter 2 while a pressure was applied by the compressor. DI water was used for testing and flow rate was measured by the flow meter. Test results of flow rate versus applied pressure difference are provided in Figure 4.25.

From the results the valve's crack pressure is determined to be about 5 psi. The measured flow rate is proportional to the pressure difference applied, as predicted by Poiseuille's law. The flow rate is about 19 ml/sec at a pressure difference of 90 psi, which is the largest pressure provided by the compressor. Much higher flow rate is expected if larger pressures are applied based on Poiseuille's law. On the other hand, the valve sealing is very good as the

backflow rate is very small (Figure 4.25). The backward flow rate is 0.023 ml/sec at applied pressure of 90 psi, which is negligible (0.13%).

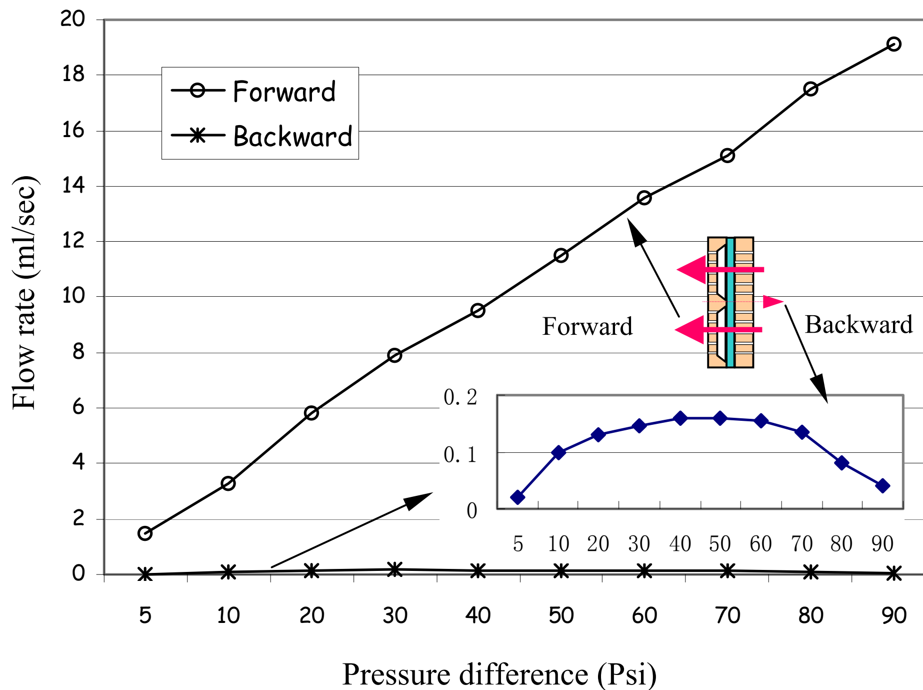

Figure 4.25:Tested flow rate versus pressure applied for a microvalve

The valve's durability is also an important concern in addition to the valve's functional performance. As described in chapter 2, a specific loading/unloading sequence was designated to testify the valve's durability. The tested loading parameters are indicated in the lower right in Figure 4.26. Ramped pressure difference was applied over the valve flap and then released back step by step in an interval of 10 psi. The flow rate was measured at each pressure level during the test process. The tested pressure progressed from lower pressure to higher. Flow rates versus each applied pressure are shown in Figure 4.26.

The test results in Figure 4.26 show that the flow rates measured repeat very well at similar pressure levels over the range of pressure differences tested. The flow rate is really linear

proportional to the pressure difference applied, regardless of how the pressure was applied. This indicates that Poiseuille's law is valid for this structure during the test. An important fact is that there were no damages or permanent deformations presented in the valve flap during the loading/unloading testing processes, otherwise any permanent deformation would result in non-elastic response (Poiseuille's law would not be valid). Microscope inspection verified this after test. We attribute this to the relative small bending of the beam.

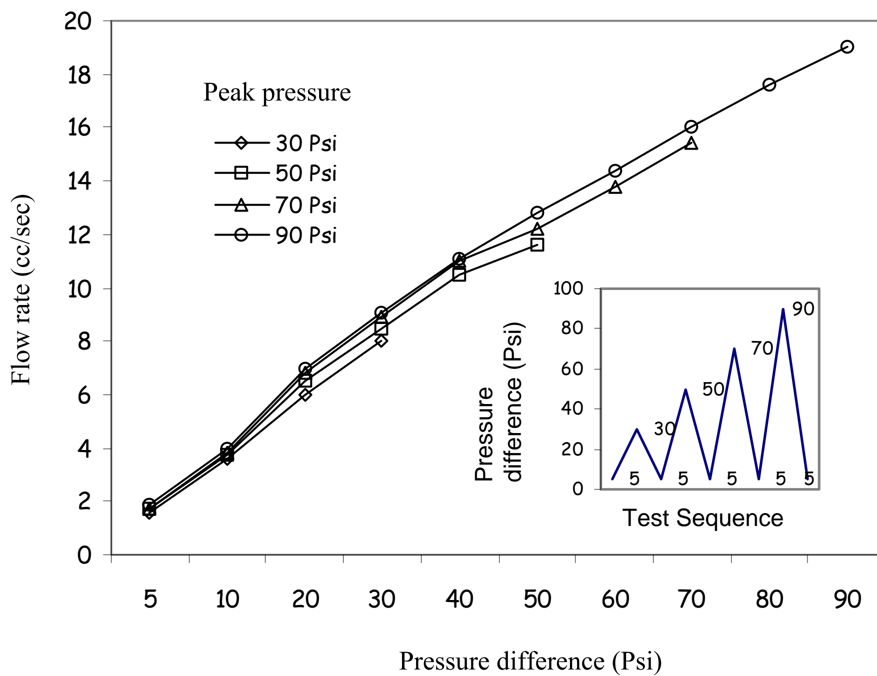

Figure 4.26: Repeated test of forward flow rate under loading/unloading conditions

4.6 Conclusion

A self-assembled robust passive high-frequency high-pressure solid nickel micro check valve has been developed for piezoelectricaly actuated pumps or hydraulic actuators. The valve can support pressure up to 10 MPa due to a novel double-layered valve flap. Simulation results show that the valve has a resonant frequency of 18 kHz (1st mode). The valve's reliability is assured by using a mechanical valve stopper.

The fabrication of the valve employed an in situ UV-LIGA process, in which the valve stopper was self-assembled to the valve array without any additional bonding process. Thick photoresist (SU-8) and thin photoresist are used as the sacrificial layers during the valve fabrication. The valve inlet and outlet channels were defined by SU-8 molds, which was also used to separate the electroformed nickel valve from the substrate. Chemical mechanical polish has been applied during the fabrication. After electroforming, all SU-8 and photoresist molds were removed by using SU-8 remover. Finally, separated final valve arrays were received. Therefore, this is a bottom–up self-assembled fabrication. Neither etching nor bonding (or packaging) is involved during the fabrication.

Test results show the forward flow rate is proportional to the pressure applied. It is approximately 19 cc/s at a pressure difference of 90 psi. The backward flow rate is 0.023 cc/s at 90 Psi pressure, which is negligible (0.13%). A specific loading/unloading sequence has been designed to test the reliability of the valve. Results show that the flow rate is extremely

well repeated over a large range of pressure differences. This implies that no damage or permanent deformation is present.

CHAPTER 5 ELECTROFORMED COPPER/SWNT NANOCOMPOSITE

5.1 Introduction

Electrolytic co-deposition of particles with metals is an effective way to fabricate innovative composite materials [36,37]. Generally speaking, composite co-deposition consists of electrolyte in which micron or sub-micron insoluble particles or fibers are suspended. Some amount of these particles become embedded in the electrochemically produced solid phase, to which they impart special properties, such as electrical conductivity, physical properties, mechanical strength, wear or corrosion resistance, etc. Metal particles, metallic oxide particles and polymer particle are used. For example, SiC particles are embedded in Nickel matrix to improve the hardness of the composite.

The deposition rate of the second phase material is affected by several interrelated parameters: the electrolyte concentration of the metal ions and particles, pH, applied current density/potential, agitation, organic additives and particle size. Pulse reverse plating can be used to increase the particle deposit concentration by eliminating a fraction of the plated metal if the concentration of sub-micron particles embedded in the deposit by conventional DC plating is not sufficient. The method has recently been demonstrated by Podlaha et al. for the copper c-alumna system, employing long, steady-state pulses, where the particle deposit concentration was improved six times over that found in DC electrical deposition.

Recently, carbon nanotubes, due to their small dimensions, remarkable strength and physical properties, are proven to be a very unique material for a whole range of promising applications, such as nanotube-based field emitters, nanoprobes in metrology and biological and chemical investigations [37], and mechanical reinforcements in high performance composites.

Discovered by Iijima et al in 1991 [38], carbon nanotubes (CNT) displays unique mechanical and electronic properties, which have initiated intensive research on these quasi-one-dimensional structures. Theoretical studies have suggested that SWNTs could have a Young's modulus as high as 1TPa [37,39], although testing experiments on single nanotubes are still in progress. The theoretical estimate for the tensile strength of individual SWNTs is up to 150 Gpa, or over hundreds stronger than steel, which has a tensile strength of 400 Mpa. SWNT shows either metallic or semiconductor electrical conductivity depending on its chirality. The thermal conductivity of CNT depends on the temperature and its chirality [47,48]. Simulation results discovered that (10,10) SWNTs have thermal conductivity around 30000 W/m•K at temperature of 100 K [40]. At room temperature, the thermal conductivity of SWNTs is in the range of 1750 to 5850 W/m•K [41].

The potential applications of CNT so far include the use of nanotubes as electron field emitters for vacuum microelectronic devices, individual MWNTs and SWNTs attached to the end of an Atomic Force Microscope (AFM) tip for using as nanoprobe, MWNTs as efficient supports in heterogeneous catalysis and as microelectrodes in electrochemical reactions, and SWNTs as good media for lithium and hydrogen storage. Because of its high mechanical

strength, SWNTs are used as excellent load-bearing reinforcements in composites. Recently, CNTs or composites based on CNTs draw people's attention, such as in heat transport management in ULSI (ultra-large-scale integration) chips and other miniature device components due to their high thermal conductivity [42].

Carbon nanotubes are perfectly quasi-one-dimensional straight tubes with diameters in nanometer scale. Single-walled nanotubes (SWNT) can be considered as a flat graphene sheet (Figure 5.1) cylindrically rolled into a seamless tube with a constant radius [43,49]. Two atoms in the sheet are selected as the origin, and when the sheet is rolled, the two atoms coincide with one another. The vector OA is known as the "rollup" vector, whose length is equal to that of the circumference of the nanotube. The tube is created so that point *O* touches point *A*, and *B* touches $B^{'}$. The tube axis is perpendicular to the rollup vector. The chiral vector of the nanotube, OA, can be defined by

$$\overrightarrow{OA} = n\overline{a_1} + m\overline{a_2} \qquad (5.1)$$

where $\overline{a_1}$ and $\overline{a_2}$ are unit vectors in the two-dimensional hexagonal lattice, and n and m are integers, which are referred to as chiral indices. The angle θ, which is the angle between OA and $\overline{a_1}$, is called the chiral angle and always less than 30 degree.

Carbon atoms in SWNT can be assigned to a coordinate system (n, m), with m <= n at all times. As chiral vectors change, nanotube properties change from metallic to semi-conducting. The (n, 0) direction is known as zigzag structure, while the n=m s denoted as armchair structure (Figure 5.2).

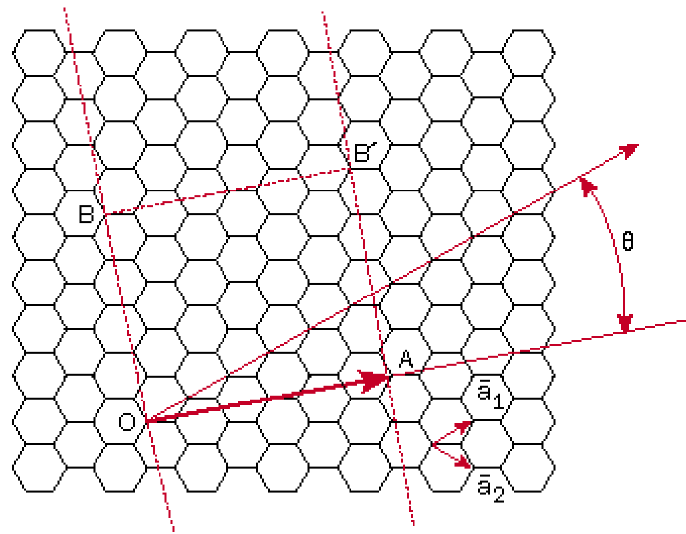

Figure 5.1: Graphene sheet illustrating chiral arrangements

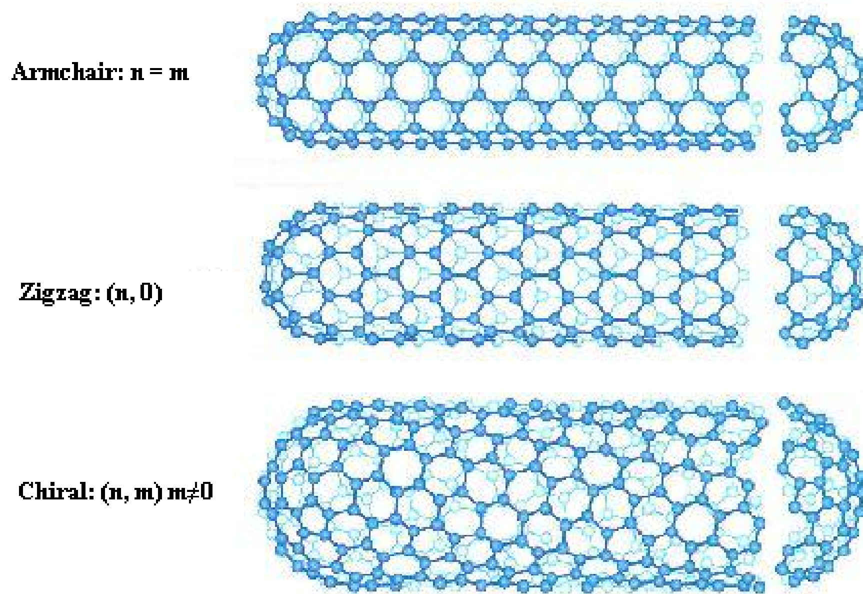

Figure 5.2: Armchair, Zigzag and Chiral Nanotubes

It should be noted that all armchair chiralities of CNT display metallic properties. In addition, chiral vectors with:

$$n - m = 3i \tag{5.2}$$

where i is an integer, yield metallic properties. All other arrangements of (n, m) in CNT display semi-conductor properties. Chirality affects the electrical properties of nanotubes, as well as optical activity, mechanical strength, and various other properties. Deformations and defects in CNT can also have a profound impact on intrinsic properties. Junctions or bends in nanotubes can be introduced by the replacement of a hexagonal carbon ring with a pentagonal or heptagonal ring. Bends, which may be inward or outward, can severely affect the electrical conductivity of nanotubes.

Like graphite and diamond, the thermal conductivity of carbon nanotubes is dominated by; lattice vibrations, which are described as elastic waves moving through the solid with the speed of sound [43]. These waves are described as phonons in the quantum picture and can carry heat through the solid. Phonons can collide with on another in what are called Umklapp or Normal processes due to anharmonicities of the interatomic forces. This phonon scattering leads to a finite thermal conductivity. As the temperature decreases, the probability for such scattering diminishes, and thus the thermal conductivity increases.

The thermal conductivity κ of a solid along a particular direction, taken here as the z axis, is related to the heat flowing down a long rod with a temperature gradient dT/dz by

$$\frac{1}{A}\frac{dQ}{dt} = -k\frac{dT}{dz} \tag{5.3}$$

where dQ is the energy transmitted across the area A in the time interval dt. In solids where the phonon contribution to the heat conductance dominates, κ is proportional to Cvl, the product of the heat capacity per unit volume C, the speed of sound V, and the phonon mean free path l. The latter quantity is limited by scattering from sample boundaries (related to grain sizes), point defects, and by Umklapp processes.

Based on molecular dynamics, S. Berber, et al [40] calculated the thermal conductivity of an isolated (10,10) nanotube along its axial direction, as illustrated in Figure 5.3. The calculations suggest that at T=100 K, carbon nanotubes show an unusually high thermal conductivity value of 37000 W/mK and the room temperature the value is 6600 W/mK.

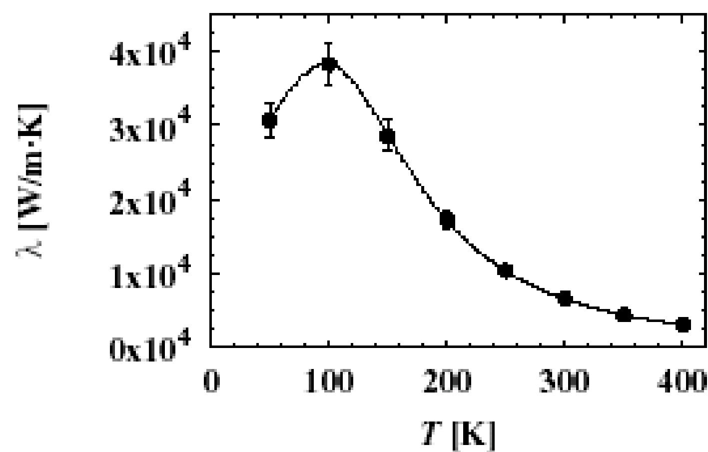

Figure 5.3: Temperature dependence of the thermal conductivity for a (10,10) carbon nanotube for temperatures below 400 K. [40]

Besides thermal conductivity, the coefficient of thermal expansion is extremely important. Since carbon nanotubes consist of sp^2 bonds related to graphite, they are expected to have a negative CTE at moderate temperatures. Based on molecular dynamics, Yong-kyun Kwon, et

al predicted the value of CTE to be as low as –12 x 10^{-6} K^{-1} at 400 K [44]. They also claimed that nanotubes contracts both axially and volumetrically (Figure 5.4). CTE of nanotubes can also be measured by X-ray diffraction [45], where the estimated value of CTE is –1.5 ± 2.0 x 10^{-6} K^{-1} in diameter between room temperature and 900 K.

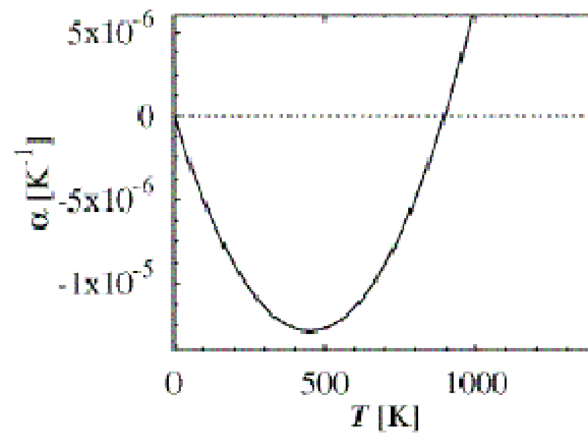

(a)

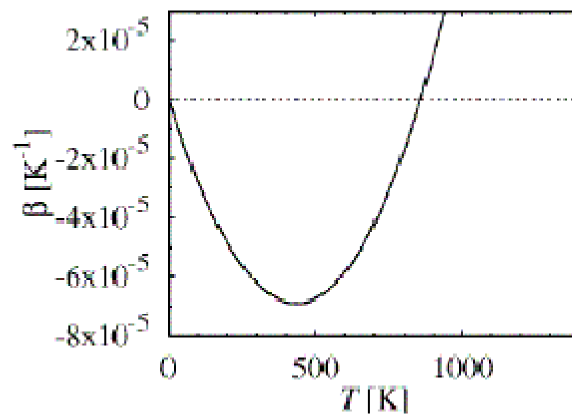

(b)

Figure 5.4: CTE of carbon nanotubes (a) linear (b) volumetric [44]

These properties make carbon nanotubes a potential candidate for reinforcements in composite materials. Nanotubes filled polymer composites are a major material application area, however there have not been many successful experiments showing the advantage of using nanotubes as fillers over traditional carbon fibers. The main problem is caused by the difficulties of creating a good interface between nanotubes and the polymer matrix. Thus, it is difficult to attain good load transfer from the matrix to the nanotubes, during loading. The reason for this is essentially two-fold. First, nanotubes are atomically smooth and have nearly the same diameters and aspect ratios (length/diameter) as polymer chains. Second, nanotubes are almost always organized into aggregates, which behave differently in response to a load, as compared to individual nanotubes.

A promising way to fabricate nanotube-reinforced composites is electrochemically co-depositing nanotubes into metal matrix. In this case, the metal atoms will grow directly on the wall of the nanotubes due to its conductivity, which makes a good interface for load/heat transfer.

5.2 Motivation

The request to reduce the size of electronic devices and integrated MEMS/NEMS faces the challenge of the thermal management problem. It is now widely accepted that the thermal management in nanosize devices become increasingly important as the size of the devices reduces.

One problem arises: how to move heat from AlGaN/GaN high electron mobility transistors grown on SiC substrate dies used in high power radar. As illustrated in Figure 5.5, the active devices generate huge heat up to 10000 W/cm^2, which will spread in SiC and result in an energy density of 100 – 400 W/cm^2. There are two problems need to be solved. First, the excessive heat needs to be moved efficiently, in which a high conductive material will replace the CuMo substrate. Second, to reduce stress in the CuMo-SiC interface. These components have substantially different coefficients of thermal expansion (CTE) resulting in undesirable stress caused by thermal expansion mismatch, which can induce fatigue and fracture-related failures (eg. delimination) at their interface.

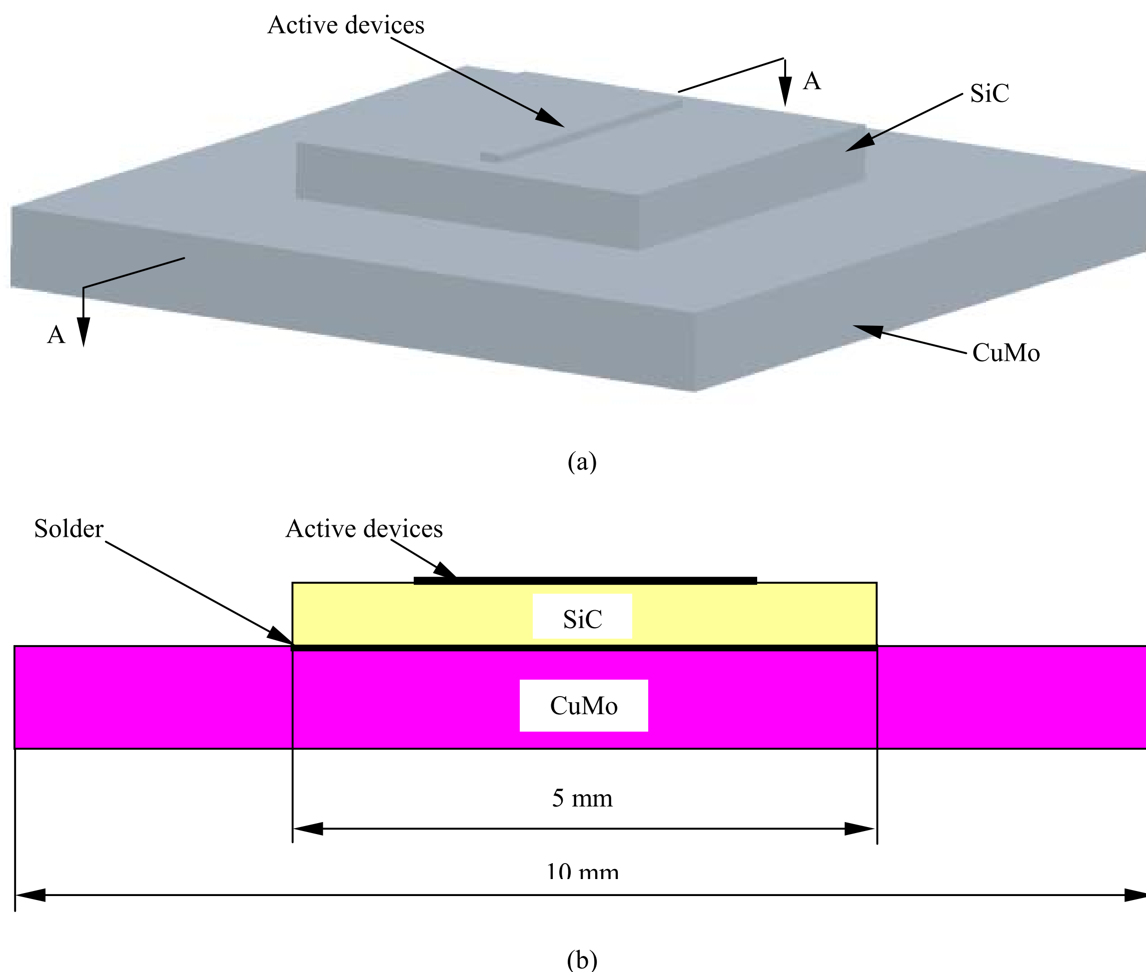

Figure 5.5: Concept scheme of the heat management structure for transistor

The properties of the SiC die and the copper-molly substrate are listed in table 5.1.

Table 5.1: Thermal properties of SiC, CuMo and Sn-3.5Ag at temperature range of 20 to 150 °C

Material	Thermal conductivity (W/m-k)	CTE (10^{-6}/K)
SiC	490	3.8
CuMo	181	5.8
96.5Sn-3.5Ag (solder)	57	17.6-30

It is obvious that the thermal conductivity of the CuMo is low and its CTE doesn't match that of the SiC die with a ratio of 3.5. As a result, the stress in the interface will reach up 40 to 70 Mpa as power goes up, which will delaminate the solder used. A solder of 96.5 Sn-3.5 Ag with a thickness of 50 μm is used to bond the SiC die to the CuMo plate. This solder has a maximum boning strength of around *35 Mpa* at room temperature and will diminish with temperature increasing and aging.

A solution to this problem is to develop a new material to match the CTE of SiC along with a high thermal conductivity. Since carbon nanotube has negative CTE, it is the ideal filler for metal matrix composite to reduce the overall CTE. Electroforming provides a convenient way to fabricate this kind of material. Copper is chosen for the base material for its good thermal conductivity as well as the ease to electroplate. Furthermore, when combining with micromaching technique, we can grow this composite material directly on the SiC and

exclude the use of solder. The bonding strength is assured by choosing proper seed layer and deposition techniques.

5.3 Prediction of Copper/SWNT Properties

Different models exist to calculate the properties of a composite from those of its components. The Rule of Mixture can obtain an approximation. If the components have nearly equal properties, the targeting property can be expressed as:

$$a_c = a_f V_f + a_m (1 - V_f) \qquad (5.4)$$

Where a_c is the property of the composite, a_f is the corresponding property of the reinforcement material, a_m is the that of the matrix and V_f is the volume fraction of the former.

For CTE, because copper and carbon nanotube have different Young’ smodulus, the equation can be adjusted by using the modulus (E) of each component [46]:

$$\alpha_c = \frac{\alpha_f V_f E_f + \alpha_m (1 - V_f) E_m}{V_f E_f + (1 - V_f) E_m} \qquad (5.5)$$

where E_f is the modulus of the reinforcement material and E_m is that of the matrix material.

Using equation 5.5, we can calculate the CTE of the composite approximately (Figure 5.6). The properties involved are listed in table 5.2. Similarly, the estimated thermal conductivity can be obtained by equation 5.4 (Figure 5.7). Because the random dispersion of SWNT in the composite, we assume the property of the composite is isotropic.

Table 5.2: Properties of single-walled carbon nanotube and pure copper

Material	Thermal conductivity (W/m-k)	CTE (10^{-6}/K)	Young'smodulus (Gpa)
SWNT	3000	-1.5	1000
Copper	385	16.4	110

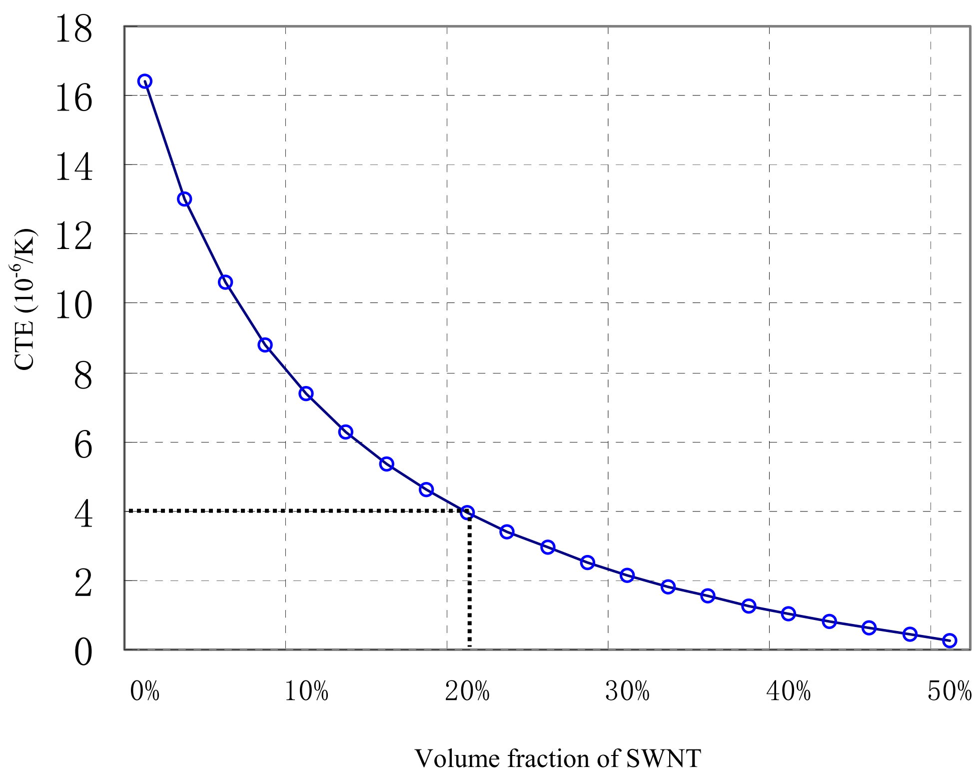

Figure 5.6: CTE estimation for copper/SWNT v.s. SWNT's volume fraction

From Figure 5.6, we discover that the CTE of the composite is 4.0 x 10^{-6} /K at the volume fraction of the 20%, which matches that of SiC (3.8 x 10^{-6} /K). The corresponding thermal conductivity of the composite is 908 W/m-k from Figure 5.7, four times higher than that of

CuMo current used. With a higher thermal conductivity, the composite can remove more heat from the SiC die, which will reduce the temperature of the transistors and that of the SiC-base plate interface, and therefore decrease the interfacial stress. The matched CTE plays an more important role in reducing the stress, especially for dynamic thermal loads.

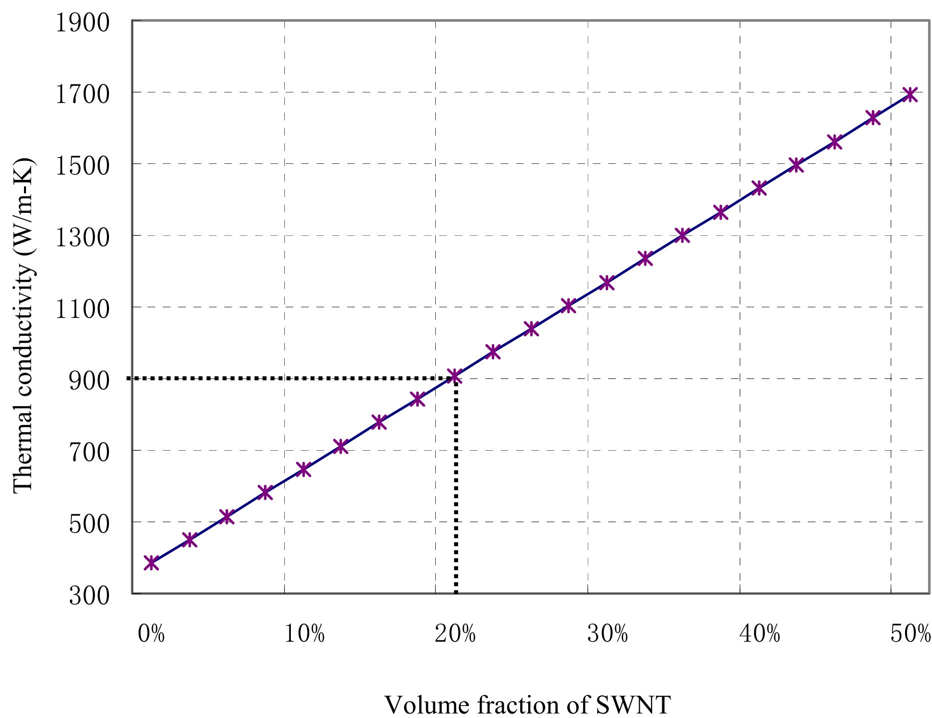

Figure 5.7: Thermal conductivity estimation for copper/SWNT v.s. SWNT's volume fraction

Using these properties, the interfacial temperature and stress were simulated with finite element analysis, showing in Figure 5.8 and 5.9, respectively. Thanks to symmetry, one quarter of the structure was used for simulation. The maximum stress in the interface is 20.6 Mpa, a safe value for the solder (96.5Sn-3.5Ag) and other potential bonding methods.

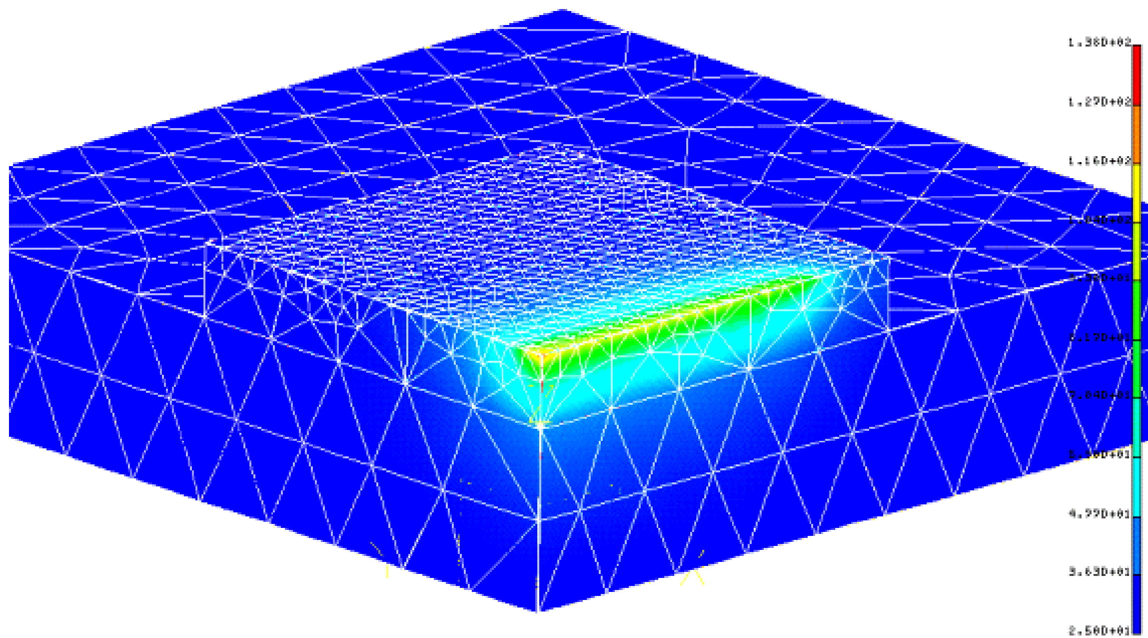

Figure 5.8:Temperature Gradient in SiC and Cu/CNT composite (around 80 °C)

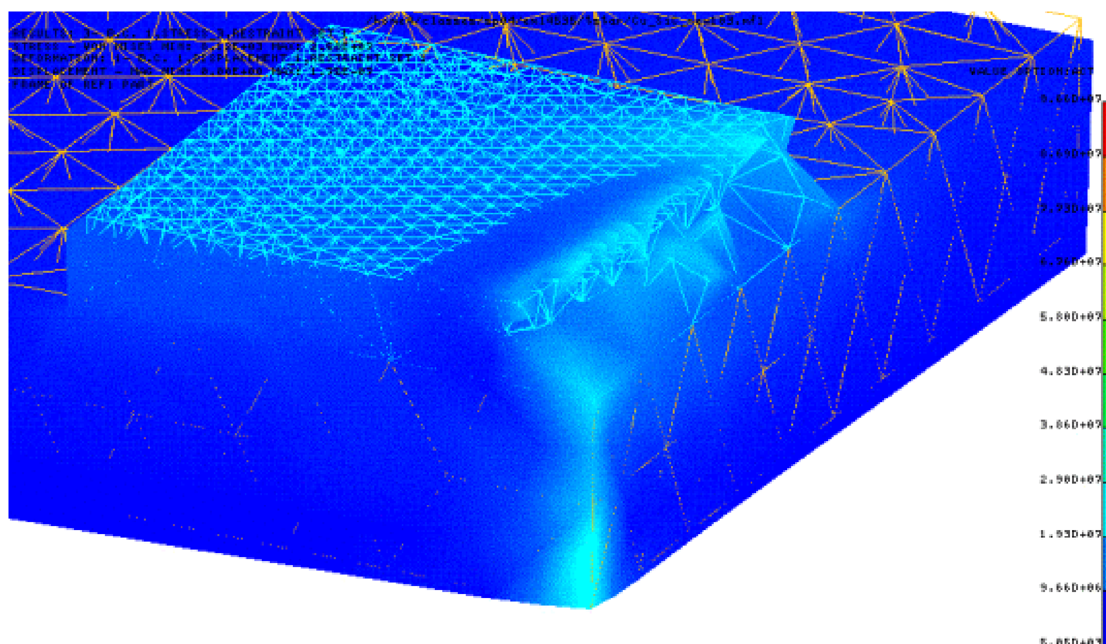

Figure 5.9: Stresses in SiC and Cu/CNT composite, right top edge of SiC plate removed to focus on stresses at interface (Max 20.6 Mpa)

5.4 Fabrication

Electroforming is chosen to fabricate the composite, shown in Figure 5.10. In this case, the SWNTs are dispersed in the copper electrolyte and co-deposited with copper atoms.

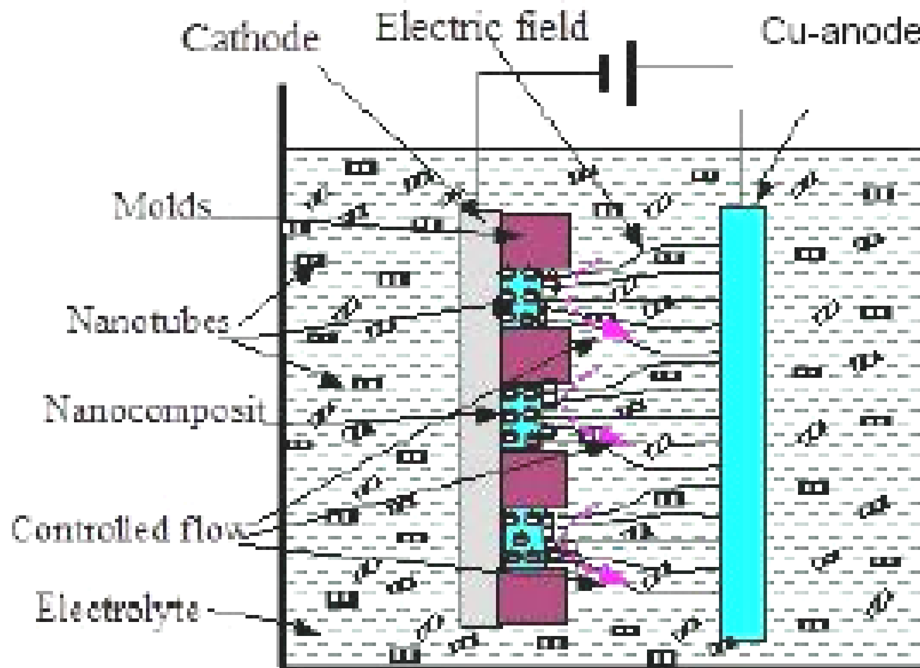

Figure 5.10: Concept scheme of electroforming for the copper/SWNT composite

5.4.1 Starting materials

The electrolyte used in this case is a high-performance acid copper solution with components listed in table 5.3. All the chemicals except "Copper Gleam CLX Start-Up" were purchased from Fisher Scientific Inc. The latter was ordered from Thinktink.com, a major supplier for semiconductor industry. A square-shaped Platinum mesh was used for anode.

The single-walled carbon nanotubes were purchased from Nanostructured and Amorphous Materials Inc. without any further treatment. The purity of the SWNT is extremely important for the quality of the composite; so scanning electron microscopy (SEM) was conducted to characterize its purity (Figure 5.11, 5.12). Looking at the SEM picture carefully, we can find that the purity of the SWNT is very high, without any impurities identified.

Table 5.3:Bulk acid copper electrolyte recipe

Component	To make 100 L, add:
Deionized (or distilled) water	70.9 liters
Copper Sulfate Pentahydrate Crystals ($CuSO_4 \cdot 5H_2O$)	7.5 Kg
35% sulfuric acid (car battery acid)	28.6 liters
Concentrated hydrochloric acid (35% HCl)	13.3 ml
Copper Gleam CLX Start-Up	1.25 liters

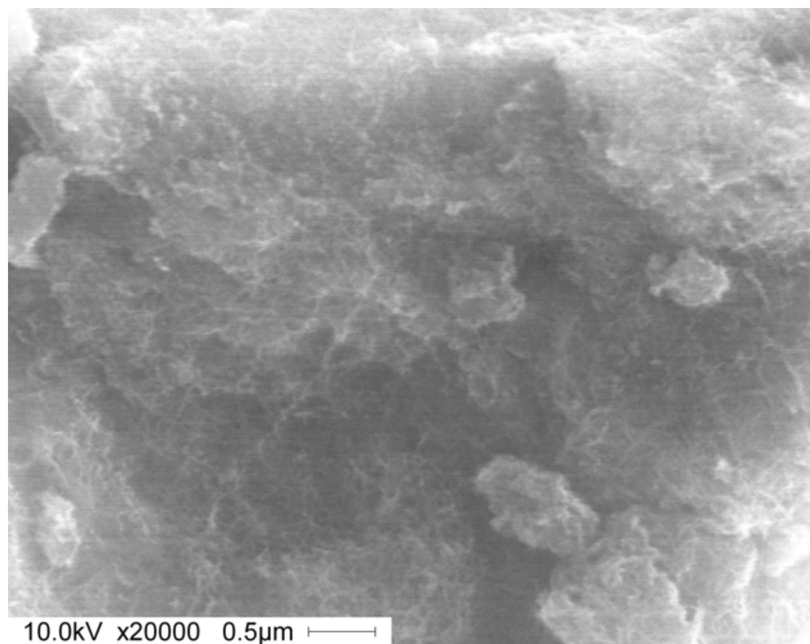

Figure 5.11: SEM picture of the as-purchased purified SWNT soot

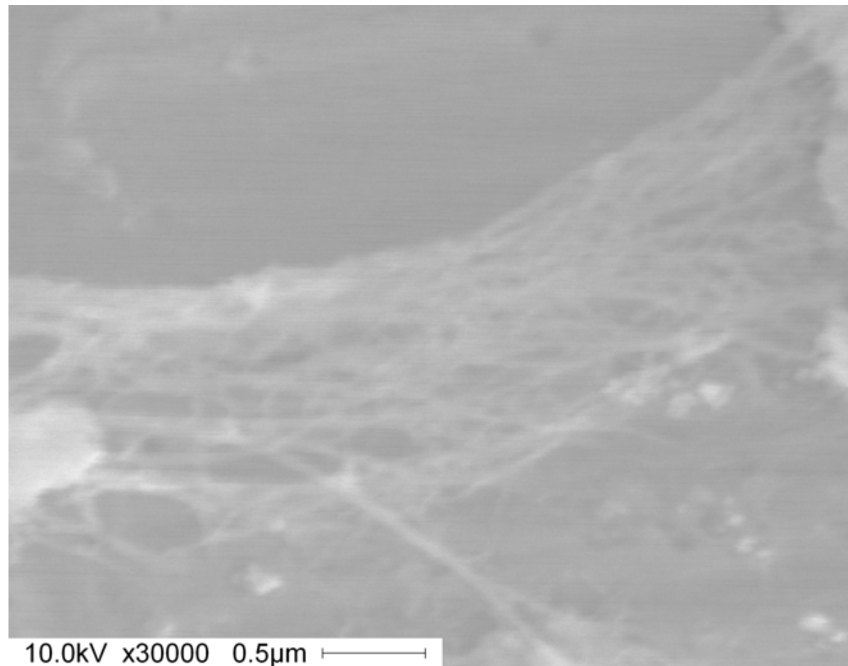

Figure 5.12: SEM picture of the as-purchased purified SWNT soot dissolved by acetone.

5.4.2 Fabrication process

In order to achieve good distribution of SWNTs in the composite, it is very important to disperse the SWNTs in the electrolyte. For this purpose, SWNT dispersion experiments were conducted with the help of surfactants. Three in-house surfactants including Sodium Dodecyl Sulfate (SDS), Triton X-100 and Pointe Scientific Inc Wetting Agent (mainly Triton) were used as dispersants and ultrasonic stirring was employed to break the nanotube aggregates. The dispersion process is shown below:

- Disolve surfactants (1% by weight) in DI water.
- Add nanotube soot to the solution above, ultrasonic stirring for at least 24 hours.
- Mix desired amount SWNT solution with copper bath and sonificate for at least 1 hour.

Uniform black solutions were obtained at this moment. Then these solutions were observed for aggreagating without stirring. Regarding to time, the Pointe Scientific Inc Wetting Agent gives the best results. SWNT solution (Figure 5.13) based on it can survive for serval days without aggregation of the nanotube with maximum concertration of 10g/L.

Figure 5.13: SWNT (1g/L) dispersed in copper bath with Pointe Scientific Inc Wetting Agent

Next, electroforming was conducted to fabricate the composite using the solution obtained above. Current density and SWNT concentration of the solution are adjusted to change the SWNT content in the composite. The plating conditions are listed in table 5.4. This solution was modified from table 5.3. The concentration of copper ions was increased by adding more copper sulfate, because no copper anode was used in the experiment which will drop debris in the process of dissolving and then damage the cathode. Therefore, the copper ions were being consumed in the process. So it is important to get a high initial concentration. The

concentration of the sulfuric acid was reduced because it will be produced in the process of electroplating. The current density was kept low to maximum the SWNT content in the composite.

Table 5.4: Electroforming conditions for the composite

Component	Concentration (/L)
Copper Sulfate ($CuSO_4 \cdot 5H_2O$)	250 g
98% sulfuric acid	40 mL
Hydrochloric acid (35% HCl)	0.13 mL
Copper Gleam CLX Start-Up	1 mL
SWNT	2 g
Temperature	Room temperature
Current density	10 mA/cm^2

At current density of 10 mA/cm^2, the electroforming will take 5 days to get the composite with thickness of 1 mm. Also some thin samples with thickness of 10-20 microns were fabricated for electrical conductivity measurement.

5.5 Characterization

The fabricated samples were then taken for characterization. First, the density was measured to find the overall SWNT content in the composite approximately. And SEM picture was

taken to see the morphology. The electrical conductivity was measured by a four-point probe, from which the thermal conductivity was derived by the Wiedemann-Franz Law.

5.5.1 Morphology

The morphology of the as-fabricated composite was indicated by scanning electron microscopy (SEM), shown in Figure 5.14-5.16.

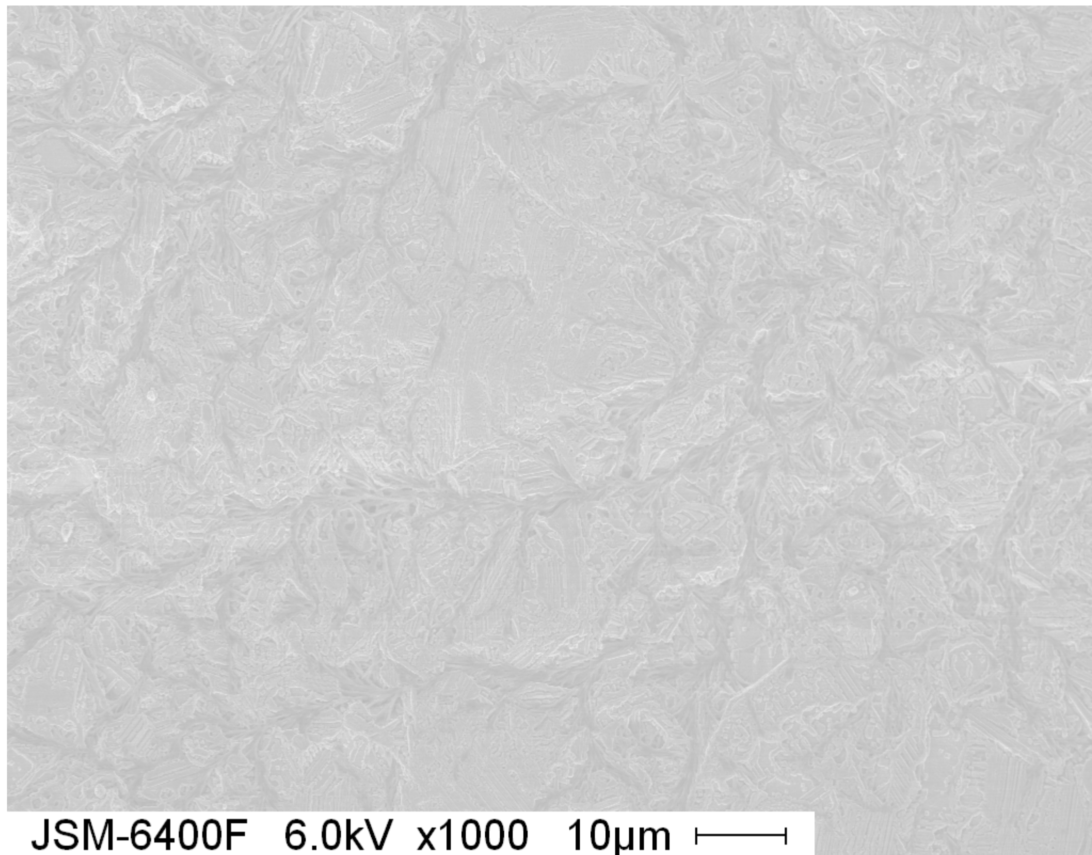

Figure 5.14: SEM picture of the composite surface, magnified by 1000 times.

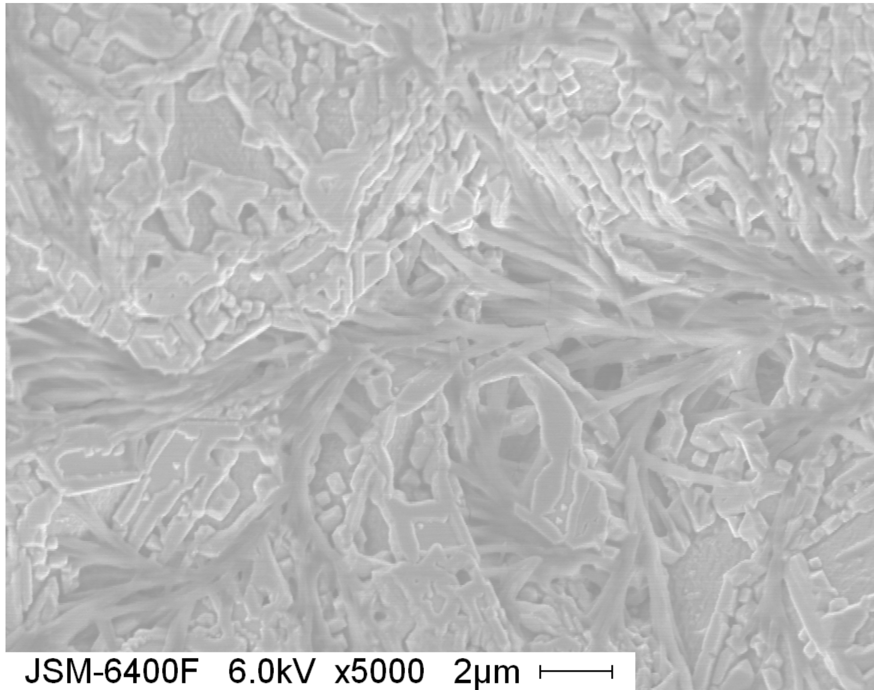

Figure 5.15: SEM picture of the composite surface, magnified by 5000 times.

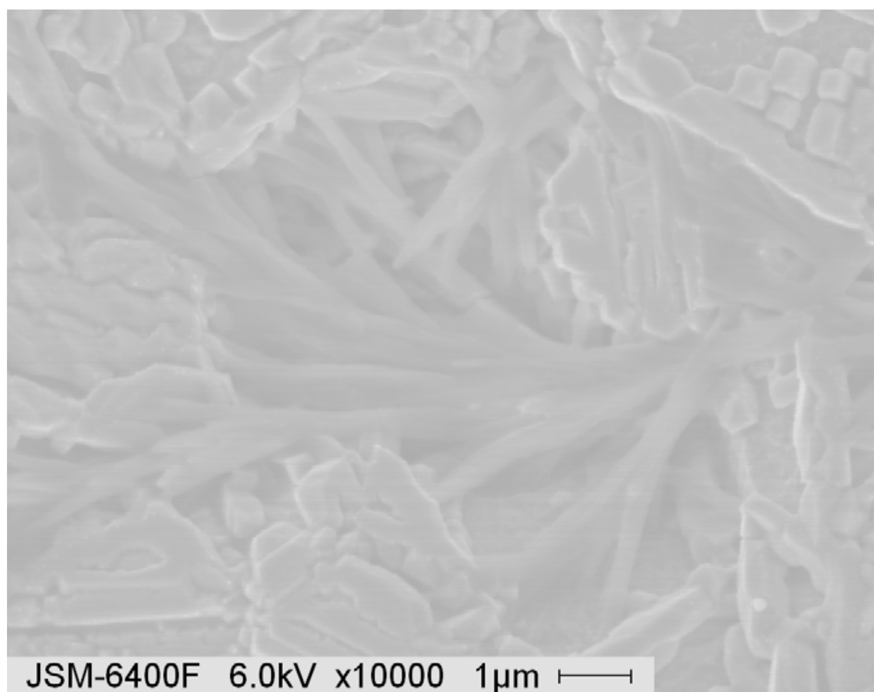

Figure 5.16: SEM picture of the composite surface, magnified by 10000 times.

The worm-shaped structures are copper coated carbon nanotubes. This is obvious when comparing with the SEM picture of pure electrochemical deposited copper (Figure 5.17). Energy Dispersive Spectroscopy (EDS) shows that this worm-shaped structure contains 29.6% (atomic ratio) Carbon atoms (Figure 5.18). The composite material is more condense after polishing (Figure 5.19).

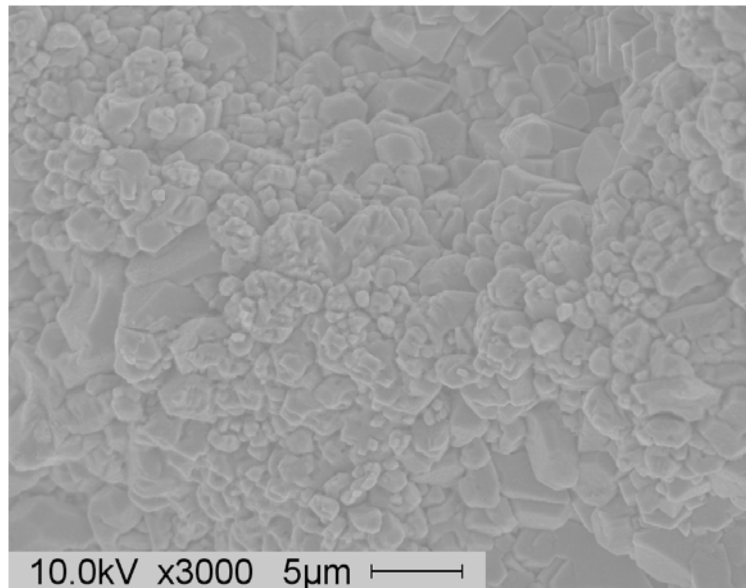

Figure 5.17: SEM picture of the pure copper surface, magnified by 3000 times

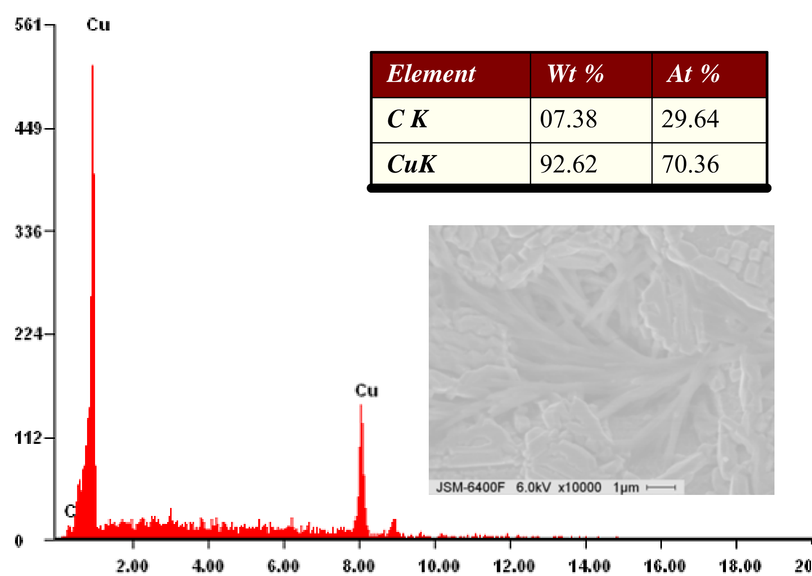

Element	*Wt %*	*At %*
C K	07.38	29.64
CuK	92.62	70.36

Figure 5.18: Energy Dispersive Spectroscopy (EDS) of the composite

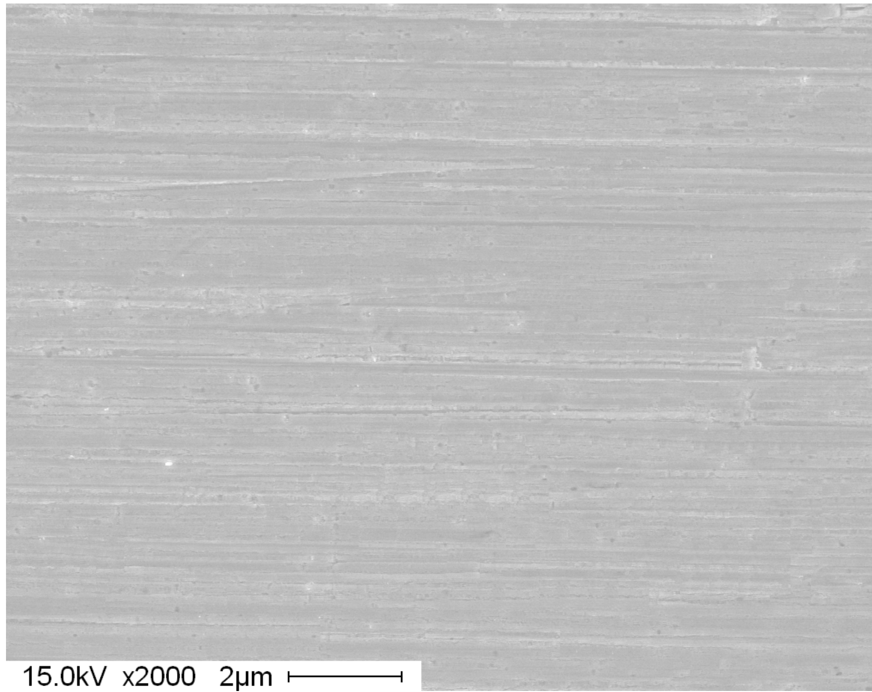

Figure 5.19: SEM picture of the polished composite surface, magnified by 2000 times. The surface was intently left rough for SEM.

5.5.2 Density measurement

Three polished samples (Figure 5.20) were used for density measurement.

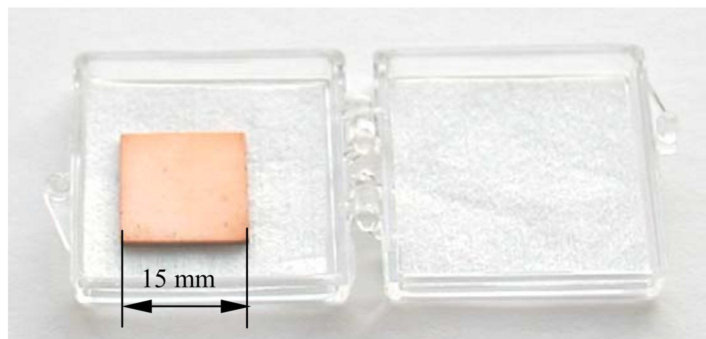

Figure 5.20: Polished composite sample.

A Balance with accuracy of 10^{-4} g was used to measure the mass of the samples, while their volume was measured by immersing them into a cylinder with accuracy of 10^{-2} mL. The results are listed in table 5.5.

Table 5.5: Density measurement of composite samples

Sample	Weight (g)	Volume (cm^3)	Density (g/cm^3)
1	1.869	0.231	8.09
2	1.819	0.252	7.21
3	1.646	0.225	7.32
Average			7.54

The average density of the three samples is 7.54 g/cm^3. When considering the Rule of Mixture (equation 5.4) and the density of carbon nanotube (1.33 g/cm^3) as well as that of pure copper (8.92 g/cm^3), we can find the volume fraction of the carbon nanotube of *18%.*

5.5.3 CTE measurement

To measure the coefficient of thermal expansion (CTE), we used the Thermomechanical Analyzer (TMA), as presented in Figures 5.21. It measures dimensional changes in a material as a function of temperature or time under a controlled atmosphere. Since the nanotubes are randomly oriented and distributed in the composite, it is reasonable to assume that the composite has isotropic properties.

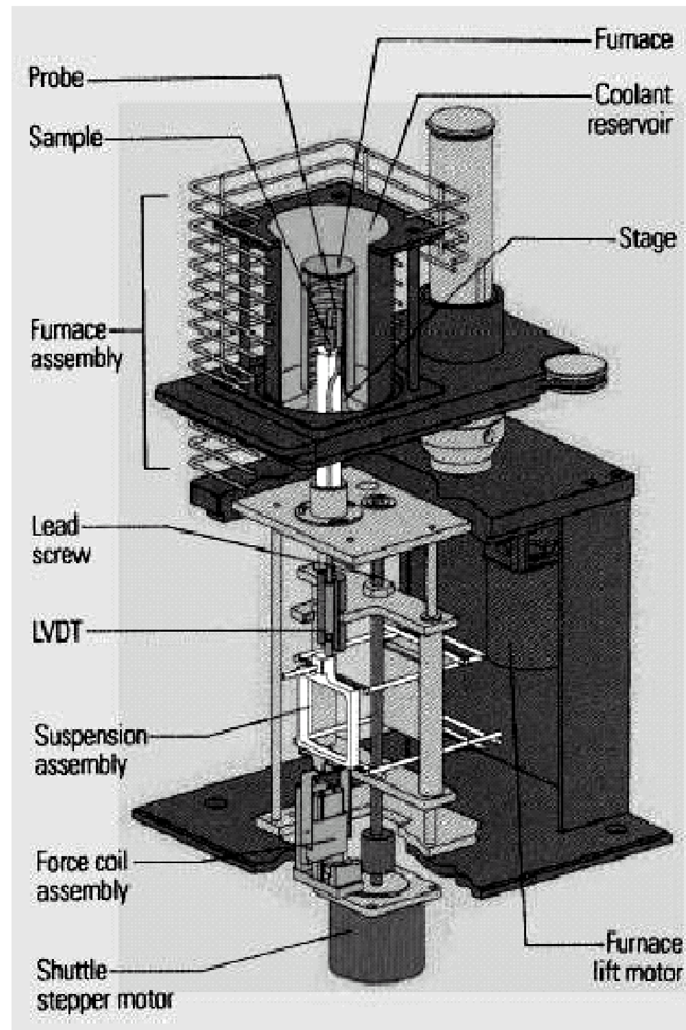

Figure 5.21: TMA thermomechanical system

The measured CTE was presented in Figure 5.22. The average value in the temperature of 30 to 150 °C is 4.70 x 10^{-6}/°C, which is close to the calculated value (4.61 x 10^{-6}/°C) from Figure 5.6 corresponding to the SWNT volume fraction of 18%. The composite has a lowest CTE of 4.22 x 10^{-6}/°C at 88 °C. The CTE decreases first and then increases with temperature

going up from 30 to 150 °C. This may be caused by the interrelation mechanism between SWNT and copper atoms, which needs to study further.

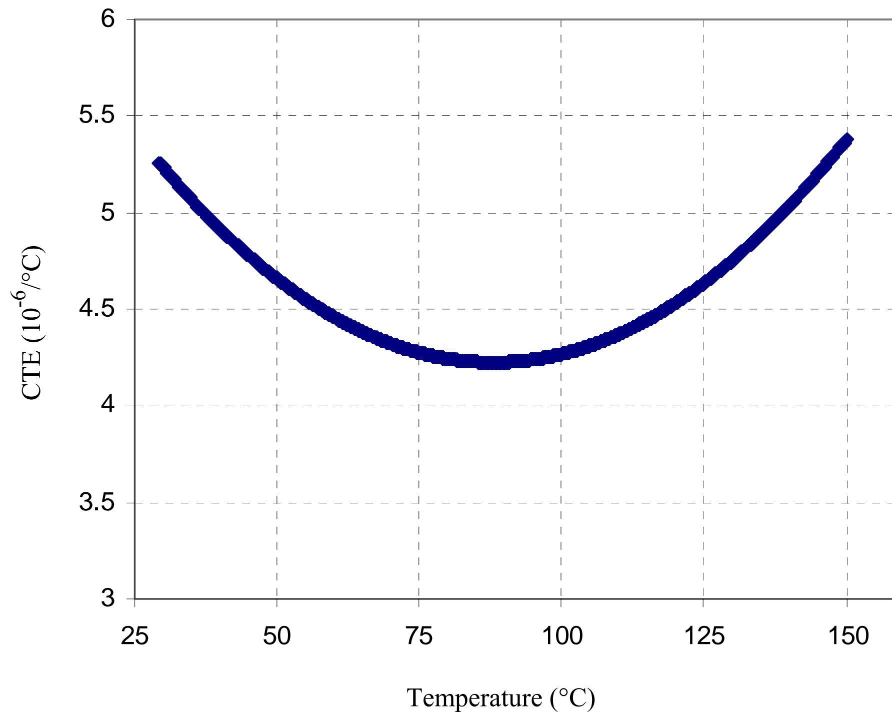

Figure 5.22: Measured CTE of copper/SWNT composite

5.5.4 Electrical conductivity measurement

The electrical conductivity was measured by a four-point probe (Figure 5.23). The purpose of this instrument is to measure the resistivity of any semiconductor or conductive material. The reason of using a second set of probes in addition to the traditional 2-point probe is that it is used for sensing and since negligible current flows in these probes, only the voltage drop across the device under test is measured. As a result, resistance measurement or I-V curve

generation is more accurate. The resistance measured by 2-wire setup includes not only the resistance in question, but also that of leads and contacts.

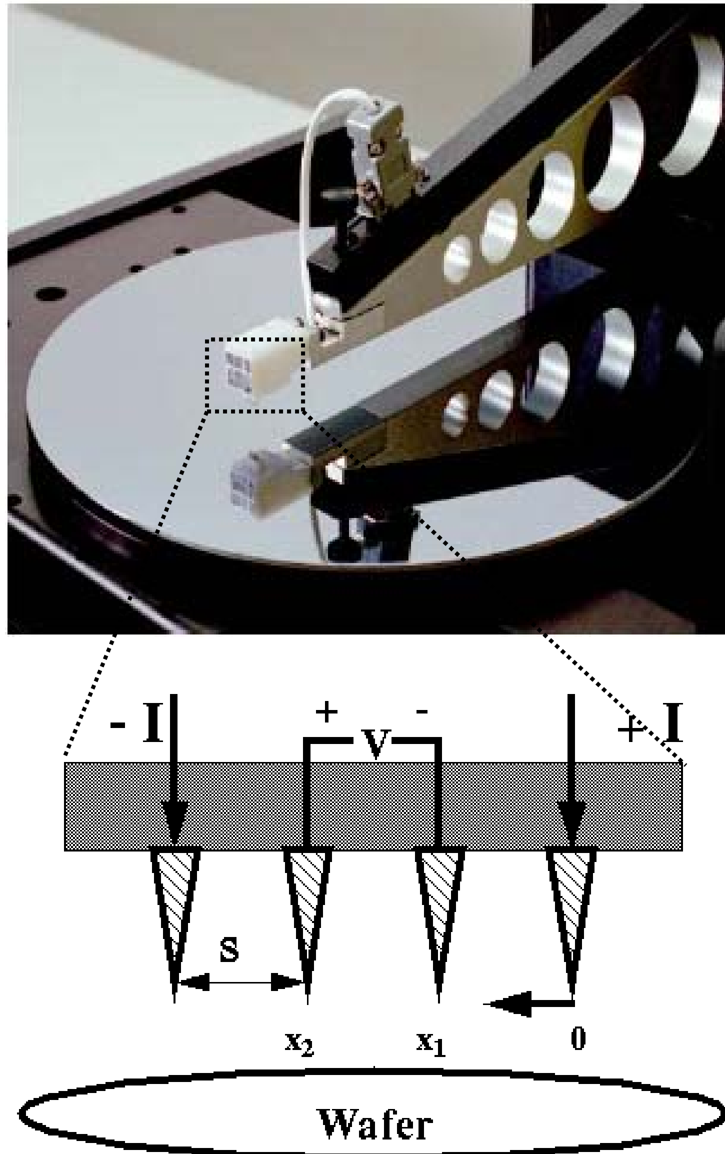

Figure 5.23: 4-point probe configuration

Thin samples were fabricated to fit the requirements. The thickness was measured by a profiler. Electroplated pure copper samples were fabricated and measured for comparative purpose. The results @ 20 °C are list in table 5.6 and 5.7.

Table 5.6: Resistivity measurement of the composite sample

Composite sample (thickness=22 μm)			
Measured point	Restivity (μΩ-cm)	Rs (Ω/□)	V/I (Ω)
Point 1	1.1858	0.000539	0.000118
Point 2	1.2408	0.000564	0.000124
Point 3	1.2342	0.000561	0.000123
Average	*1.2203*	*0.000555*	*0.000122*

Table 5.7: Resistivity measurement of electroplated pure copper sample

Electroplated pure copper sample (thickness=10.5 μm)			
Measured point	Restivity (μΩ-cm)	Rs (Ω/□)	V/I (Ω)
Point 1	1.6695	0.00159	0.000352
Point 2	1.785	0.00170	0.000376
Point 3	1.7115	0.00163	0.000360
Average	*1.7220*	*0.00164*	*0.000363*

The measured resistivity of the pure copper sample is 1.72 μΩ-cm, which validates the accuracy of this measurement because the published one is 1.7 μΩ-cm. The electrical resistivity of composite is 1.22 μΩ-cm, which is 30% better than that of copper. The conductivity is the reverse of resistivity. From this relation, we can obtain the electrical conductivity of composite is 8.2 x $10^7\ \Omega^{-1}m^{-1}$, which is 40% better than that of copper (5.8 x $10^7\ \Omega^{-1}m^{-1}$, Figure 5.24).

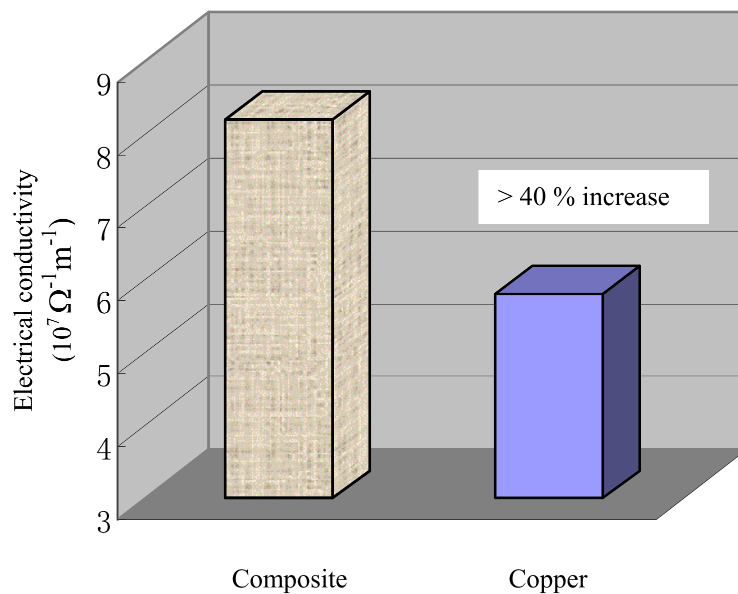

Figure 5.24: Electrical conductivity of composite and copper

5.5.5 Thermal conductivity

For metals, both electrical and thermal conductivities employ free electrons in that metal. Other properties such as electron charge and the number of free electrons per unit volume will also have influence. The thermal conductivity increases with the average particle velocity since it increases the forward transport of energy. However, the electrical

conductivity decreases with particle velocity because the collisions hinder the electrons from transporting charge. Wiedemann-Franz Ratio or the Lorenz constant describes the ratio of thermal to electrical conductivity of metals:

$$L = \frac{\kappa}{\sigma T} = \frac{\pi^2 K_B^2}{3e^2} = 2.45 \bullet 10^{-8} W\Omega / K^2 \tag{5.6}$$

where K_B is Boltzmann constant, e the electron charge, κ is the thermal conductivity and σ is the electrical conductivity. When considering the contribution of phonons, the Lorenz constant will differ slightly from its absolute value. For copper the number is 2.25 x 10^{-8} $W\Omega/K^2$ at 20 °C. From this relation, we obtained that the thermal conductivity of composite is 588 W/m-k at 20 °C (Figure 5.25), 40 percent better than pure copper (385 W/m-k).

From Figure 5.7, the predicted thermal conductivity of the composite is 842 W/m-k at the SWNT volume fraction of 18%. Therefore, there is a big difference between the calculated one and the predicted one. The reasons for this are:

- The Wiedemann-Franz law doesn't consider the contribution of the phonons, which dominated the heat conduction of SWNTs.
- The dispersion of SWNTs is not good enough to mix the carbon nanotube with copper atoms. When using the surfactant to disperse the nanotubes, they are present in the solution as bundles (10-20 nanotube a bundle). There are limited amount of aggregates in the electrolyte and as a result SWNT aggregates exist in the composite (Figure 5.26). This will decrease the conducts between copper atoms and SWNTs and decrease the overall thermal conductivity of the composite.

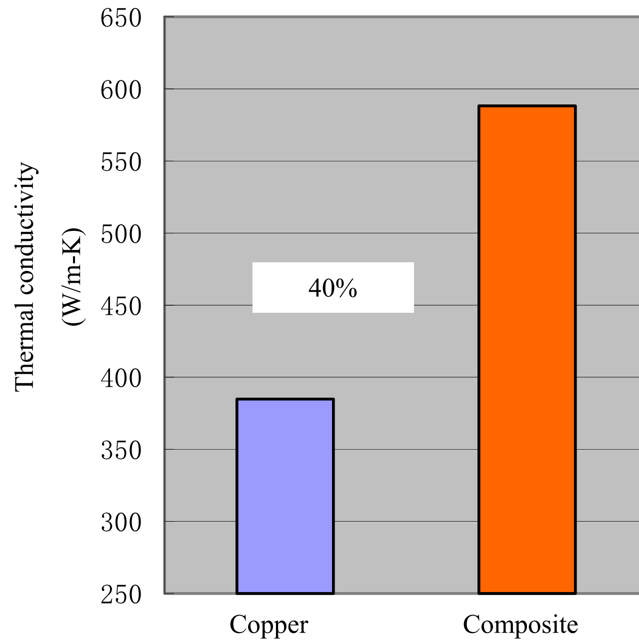

Figure 5.25: Thermal conductivity of composite and copper

5.6 Conclusion

Copper/SWNT nanocomposite was developed by electroforming process, where the SWNTs were co-deposited with copper atoms with applied current. SEM picture shows worm-shaped structures on the composite surface, which are copper coated SWNTs comparing with the morphology with pure copper surface. The density of the composite is 7.54 g/cm^3 indicating a SWNT volume fraction of 18%. This composite has a CTE of 4.7×10^{-6}/°C, agreeing with the value of 4.6×10^{-6}/°C predicted by the Rule of Mixture. The electrical conductivity measured by four point probe is $8.2 \times 10^{7}\ \Omega^{-1}m^{-1}$, suggesting the thermal conductivity is 588 W/m-k using Wiedemann-Franz law.

With a better-matched CTE and much higher thermal conductivity, the composite developed will be a promising substitution for the CuMo base plate used to spread the heat from SiC die for the Radar industry. The thermal conductivity of the composite is two times better than that of CuMo, which allows it to move more heat from the SiC die when same boundary conditions applied. The CTE of the composite is much closer to that of SiC (4.7/3.8=1.2) than that of CuMo (5.8/3.8=1.5). This is extremely important to reduce the stress in the interface between the base plate and the SiC die.

However, there is still room to make improvement to this composite material. First of all, the volume fraction of the SWNT in the composite can be increased to 20% to make a perfect CTE match to the SiC and reduce the interfacial stress to a very low value (20.6 Mpa as simulation results). This will increase the thermal conductivity of the composite too and helps to remove the heat more efficiently. Second, better methods and surfactants need to be researched to disperse the SWNT further in the electrolyte and consequentially better distribution in the composite. A dispersion and distribution to a single SWNT level will increase the thermal conductivity as well as decrease the CTE more efficiently.

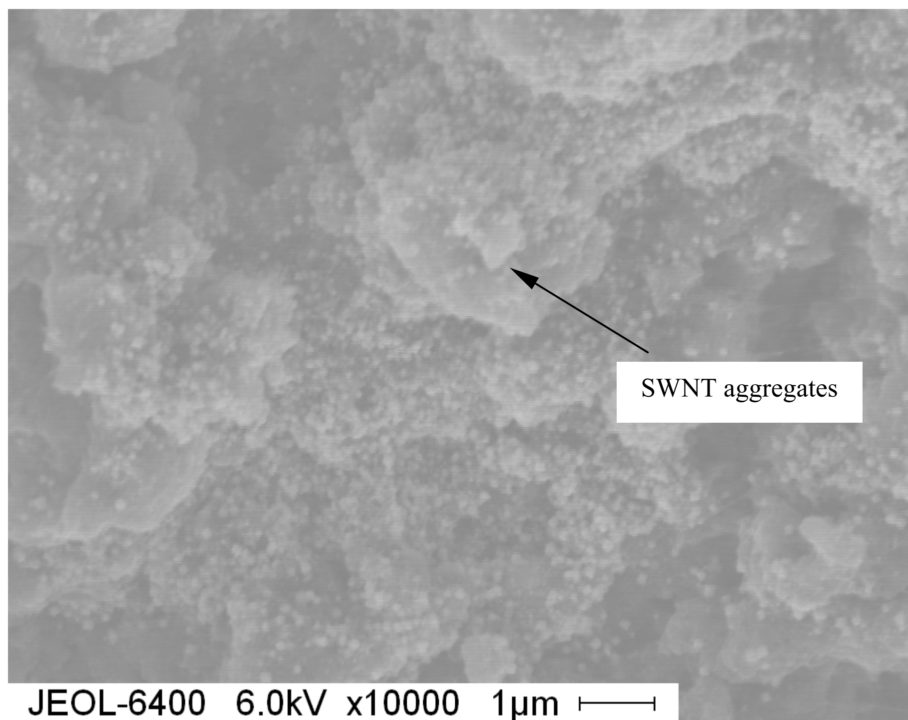

Figure 5.26: SWNT aggregates in the composite

CHAPTER 6 MICRO MECHANICAL TEST OF MICROFABRICATED MEMS MATERIALS

6.1 Introduction

Although MEMS devices come in a wide variety of applications, the amount of different structural parts used in them is rather limited. Most micro devices consist of some basic parts, which re-occur throughout the field: *cantilever beams* (single side clamped, double side clamped), *membranes* (either closed at the sides to another structural member, or as a free floating plate), *springs* (often doubling as cantilever beams), *hinges*, etc. (Fig. 1). These elements often suffer from the same degradation or failure mechanisms, regardless of their application.

Failure of MEMS elements depends on the environmental stressing conditions they are subjected to as well as the material of which they are made. Common degradation/failure mechanisms of MEMS include fracture (overload or fatigue), creep (stress), stiction (capillary forces, van der waals forces, electrostatic forces), wear and degradation of dielectrics [53,54], most of which are classified as mechanical failures. A way to avoid these failure is to avoid high stresses. Design for stresses well below (at least 2 and up to 5 times below) the ultimate strength (material's properties).

However, the material properties of structural parts are not at all well known, especially not in thin film technology, where properties often differ from the macroscopic bulk behavior. Furthermore, different fabrication techniques and conditions will definitely influence the microstructures and surface conditions that change the mechanical properties especially for thin structures. For example, rough surface is more liable to induce cracks. This produces uncertainties in MEMS design and simulation, in which it is usually assumed that the mechanical properties of MEMS materials are the same as those of their bulk materials, because of lack of experimental data on micro machined materials. Therefore it is very important to conductivity mechanical tests on micro machined (thin-filmed) samples to discover the mechanical behavior in the micro scale.

In micro scale, the size of the specimen and the fabrication process definitely have effect on the material behaviors. It is reasonable to expect the similar structures made up thin films and from bulk process will have different mechanical properties. Sharpe *et al.* [88] claim that there is no significant effect of specimen size on *Young's modulus;* however the strength does increase somewhat as the total surface area of the test section decreases, which might reflect the fact that the larger specimens have more surface flaws.

In particular, the successful fabrication and reliable operation of structures with feature sizes in the range 1 μm to 1 mm is strongly contingent on a sufficiently rigorous understanding of their length-scale dependent and process-dependent mechanical properties. In turn, such understanding requires the ability to measure the mechanical properties of microscale structures.

6.2 Literature Review

A set of standard test procedures defined by American Society for Testing Materials (ASTM) is used to identify mechanical properties, such as Young's modulus, Poisson's ration, and fracture strength in macro-scale. However, these standards are not completely appropriate for small MEMES specimens; nevertheless one can get guidance from them and design suitable test methods for micro-scale materials.

Different testing methods have been proposed by researchers from different researches in micro-scale. Basically, we can categorize them into two groups: direct methods and inverse methods. Direct methods refer to those similar to the approaches of ASTM defines. Tensile test is a typical direct test. In inverse methods such as the membrane [50], bending [51] and similar tests, a model is constructed of the test structure. In the following paragraphs, we will go through some typical tests.

6.2.1 Tension Test

Given the dimensions of the beam, it is straightforward to obtain a stress–strain graph, and to extract Young's Modulus, Poisson's ratio and fracture strength in tension test. Axial force is applied to stretch the specimen, from which the stress can be calculated with the dimension of the specimen known. Strain is measured as the force is applied either directly or calculated from the measurements of specimen's overall elongation. Compared to other test methods, tensile test take advantage in its simplicity. The principal difficulty associated with this

technique is the handling and mounting of the test structures. In the case of brittle materials, fracture induced by gripping presents an additional problem. This method is also sensitive to misalignment between the specimen and the set-up.

Figure 6.1 shows one configure of the tension test, where the specimen is fixed to the die at one end and gripped/glued/held at the other end. One end of specimen is fixed to the die, while the other end is gripped with an electrostatic probe [89], or glued to a force/displacement transducer using viscosity Ultraviolet (UV) light curable adhesive [90], or connected with a pin and ring mechanism.

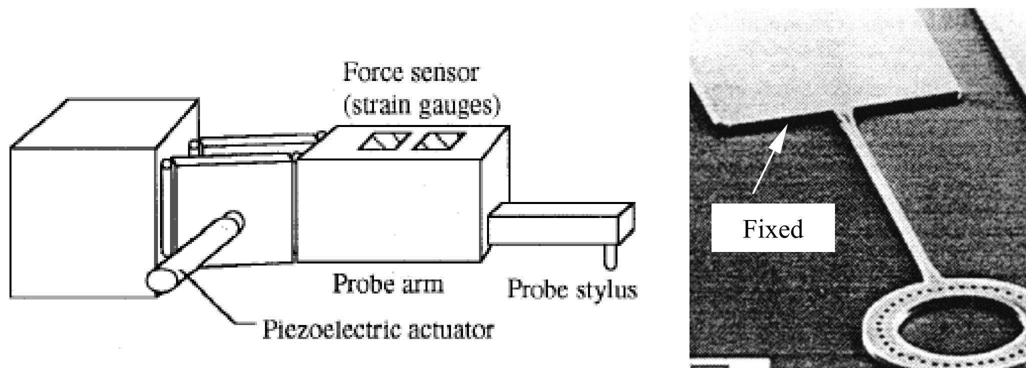

Figure 6.1: One-end-fixing tensile test (ping on the left, and ring on the right)

6.2.2 Bending Test

Compared with the direct tension test, testing by beam bending has the advantage of being simple. Bend test needs a smaller force than the tension test but yields a lateral deformation, which is large enough to be measured using an optical microscopy. Furthermore, this method is not affected by slight misalignment in the loading direction; the loading mechanism

becomes relatively simple and easy to use. For a cantilever beam of length L, width b, and thickness h, the Young's modulus is given by the expression [95]

$$E = \frac{4(1-\upsilon^2)L^3}{bh^3}\frac{P}{\delta}. \tag{6.1}$$

The fracture strength is given as [95]

$$\sigma_F = \frac{6LP_F}{bh^2} \tag{6.2}$$

where P_F is the load at fracture. Figure 6.2 shows a bending test by [91], where the fracture strength of single-crystalline silicon (75–240 μm wide, 8–16 μm thick and 75–500 μm long) was measured. They pushed the silicon micro cantilevers down with a stylus.

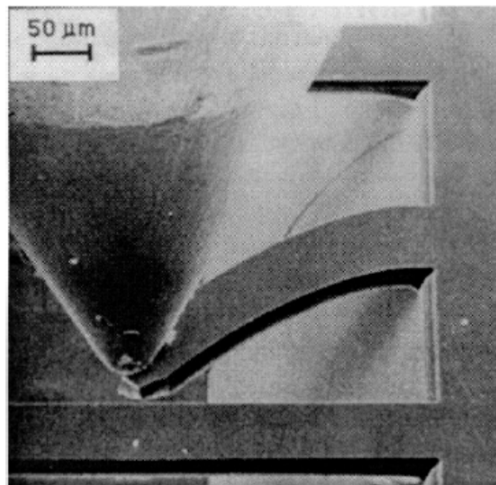

Figure 6.2: Out-of-plane bending test by a stylus

6.2.3 Membrane Test

In membrane test, the membrane is pressurized and the deflection is measured then used to determine the biaxial modulus. An advantage of this approach is that tensile residual stress in

the membrane can be measured. For rectangular membranes (with thickness h and edge length 2a), the pressure–displacement relationship is given as

$$p = C_1 \frac{h\,\sigma_R}{a^2}\delta + C_2(\upsilon)\frac{h\,E}{a^4}\delta^3 \tag{6.3}$$

The constant C_1 and $C_2(\nu)$ are determined using finite element analyses, and have values of 3.45 and 2.48 for $\nu = 0.25$, respectively [96]. In addition, the value of the Poisson's ratio can be estimated by sequentially testing membranes with square and rectangular geometries. Walker et al [92] tested pressurized square membranes with the deflection measured by a stage-mounted microscope, as shown in Figure 6.3, to study the effect of hydrofluoric acid exposure on polysilicon.

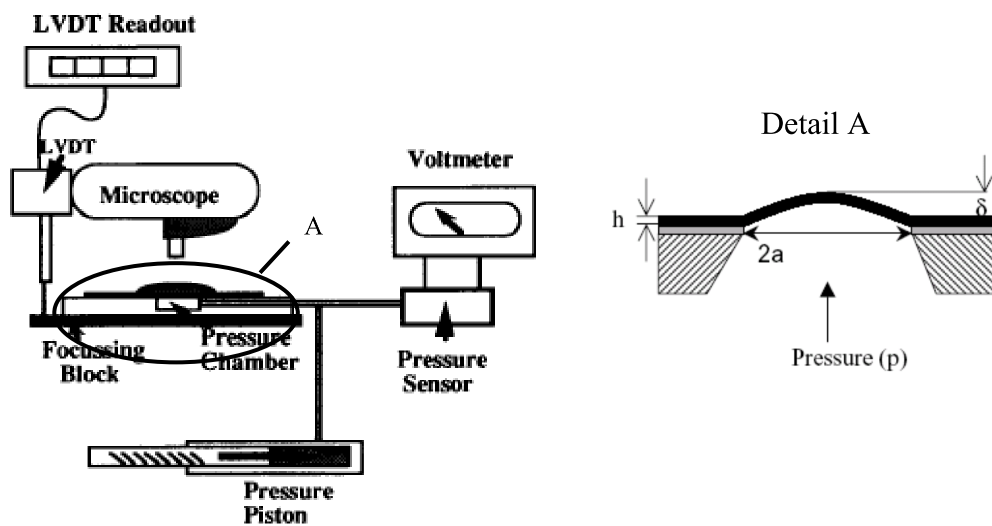

Figure 6.3: Schematic diagram of a membrane test

6.2.4 Resonant Test

Petersen et al [93] fabricated very small cantilever beams from insulating films deposited on silicon by selectively etching the silicon out from under the insulating layer in a very controlling manner. The beams are then vibrated electrostatically, and Young's modulus was determined from the mechanical resonance frequency. Movements of the beam were detected by focusing a He-Ne laser on the tip of beam and positioning an aperture detector near the edge of the deflected beam as shown in Figure 6.4. For a cantilever beam of thickness h and length L, the fundamental resonant frequency is given by

$$f = 0.1\frac{h}{L^2}\sqrt{\frac{E}{\rho}}, \tag{6.4}$$

where ρ is the density.

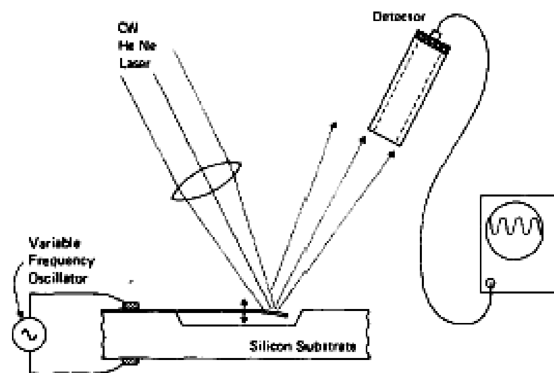

Figure 6.4: Schematic diagram of a resonant test

6.2.5 Wafer Curvature Test

The wafer curvature test has emerged as a popular technique for the evaluation of residual stresses in non-integrated, constrained, thin and thick structures, particularly, continuous films deposited on thick substrates. For small deformations, and when the film thickness (h_f) is much smaller than the thickness of the substrate (h_s), the magnitude of the residual stress in the film is given by the Stoney formula [94]

$$\sigma_R = \frac{1}{6}\left[\frac{E_s}{(1-\upsilon_s)}\right]\frac{h_s^2}{h_f}\kappa = \frac{1}{6}\left[M_s\right]\frac{h_s^2}{h_f}\kappa \tag{6.5}$$

where κ is the curvature of the film–substrate composite (which can be measured using commercially available test stations), M is the biaxial modulus, and the subscript s denotes the substrate. It is important to note that the stress can be evaluated without any knowledge of the mechanical properties of the film. In general, the residual stress has many contributions including intrinsic (growth) stresses and stresses due to thermal mismatch. The identification of the relative importance of the different components requires further knowledge, especially of the coefficients of thermal expansion of the film and the substrate.

6.2.6 Raman Spectroscopy

This is an optical technique for the measurement of residual stresses and stress gradients in diamond-type materials (such as Si, SiC, Ge), which display a Stokes Raman spectrum that is sensitive to mechanical stresses [96]. This method has been extensively applied to silicon microelectronics devices, facilitated by the availability of commercial microprobes. The

sampling volumes can be as small as 1 μm^3, and there is virtually no sample preparation required. Figure 6.5 shows the Raman peak in single-crystal silicon in the absence of stress, and indicates the expected direction of shift for tensile and compressive stresses. The interpretation of such shifts requires that the stress state be simple, and that the form of the stress tensor be known beforehand. For example, a uniaxial stress of 25 MPa in silicon corresponds to a spectral shift of about 0.05 cm^{-1}, which can be detected with high-resolution instrumentation.

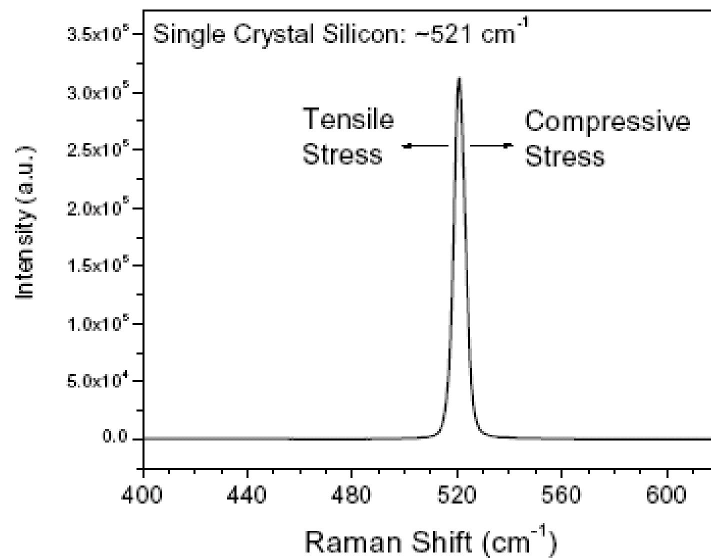

Figure 6.5:Raman spectrum of stress-free single-crystal silicon. The expected shift of the peak with uniaxial compressive and tensile stresses is indicated.

6.2.6 Discussion

Most of the abovementioned methods are indirect methods, whose accuracy may be questionable. Some of these methods like bending method involves an external force applied

to the test structure to induce deformation, which is measured by the specific instrument. Mechanical properties are calculated by using proper equations derived with assumptions and certain boundary conditions. This will definitely influence the accuracy of the testing results, especially for complex structures. Therefore, the direct method (tensile test) with simple boundary conditions and fully understood theories is highly preferred and standardized for measuring mechanical properties of materials.

6.3 Methodology

In this research, a direct (tensile) test for the mechanical properties of the electroplated nickel & SU-8 is used with an innovatively designed specimen. A MST 250 micro force tester (Figure 6.11) is employed to conduct the test, where the forces are applied by the tester and the corresponding displacements are recorded. The stress and strain are calculated out according to the specimen's dimension. Finally, the stress-strain graph is plotted and mechanical properties are extracted.

Some common concerns need to be considered when designing the specimen as well as the specimen holder because it determines the boundary conditions. In order to model the mechanical response of the test structure, it is necessary to determine the boundary (support) conditions, the initial geometric condition, and the dimensions (metrology) of the test structure. Each of these can introduce significant errors into the modeling process.

The *boundary conditions* need to be as simple as possible, which depends on the both the design and the fabrication process. The constraints imposed by the fabrication processe prevent easy characterization of the supports of microscale structures, some of which are related to the release process. *Initial geometric conditions* are also an important concern. MEMS structures are typically designed to be planar. However, residual stresses and stress gradients can lead to bending and buckling. *Metrology* can influence the strength. Depending on the test technique, the mechanical property of interest can be a strong function of the dimensional characteristics of the test structure. In addition to the small feature sizes inherent to MEMS, accurate metrology is complicated by restricted access to important structural features.

The specimen design considered all these parameters and avoided all the errors. The novel design of the specimen coupling with the specially designed specimen holder (Figure 6.6) defines very simple boundary conditions. The fabrication process assures the accuracy of the geometry of the specimen, which is aligned on the MTS 250 by using two axial alignment guiders (Figure 11). This method is suitable to a great variety of materials such as metals, plastics and composites. In this research, micro structured nickel and SU-8 were tested.

The need to test the nickel (used in chapter 2,3,4) is initiated by the disagreement of the reported data. It is reported by many researchers that the Young' smodulus of the electroplated nickel is from 160 GPa to 230 GPa [52,55], however other researchers published the tested value of the electroplated nickel is only about 20 to 30 GPa. For SU-8, the experimental data are sparse. Therefore, it is necessary to test the properties of these

materials in micro scale based on the processing conditions with the testing process developed. However, this method is suitable to a great variety of materials such as metals, plastics and composites.

6.4 Specimen Design

The tensile testing specimen is shown in Figure 6.6. For easy handling while keeping the specimen in micro scale, three micro beams are used in the specimen. The function of the ribs is to reinforce the pads so that allows most of the deformation occurring on the specimens. Finite element simulation shows that a uniform stress distribution (0.5% difference) in the three specimens is achieved when a stretch is applied on the pads and 97.7% of the axial deformation occurs on the specimens (Figure 6.7).

6.5 Specimen Fabrication

The nickel specimen is fabricated by two electroforming steps defined by SU-8 molds (Figure 6.8) in a watts type bath. A pulse current with average current density of 25 mA/cm^2 and duty cycle of 50% is used, which gives a deposition rate of 15 μm/hr. The final fabricated structure is shown in Figure 6.5 with specimens' thickness of 30 μm. The Su-8 molds and specimens (Figure 6.9) were fabricated following the process described in chapter 4.

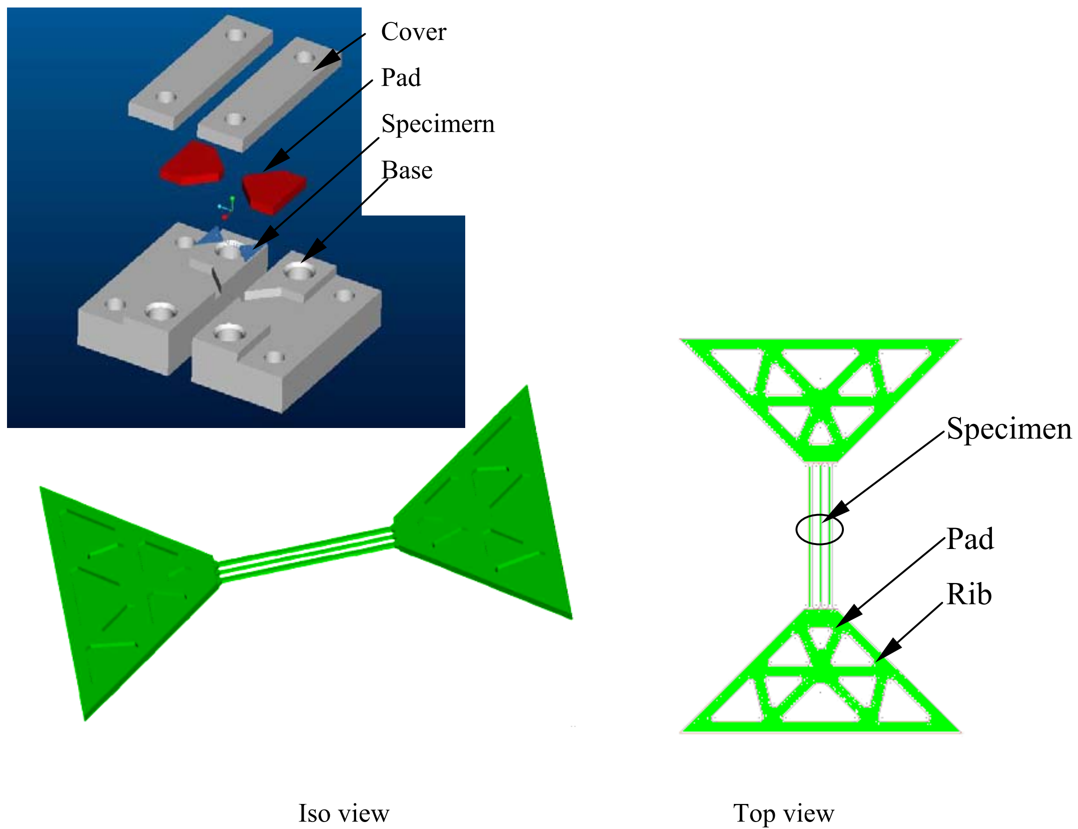

Figure 6.6: Specimen holder and testing specimens with width of 90 μm, 40 μm and 90 μm respectively.

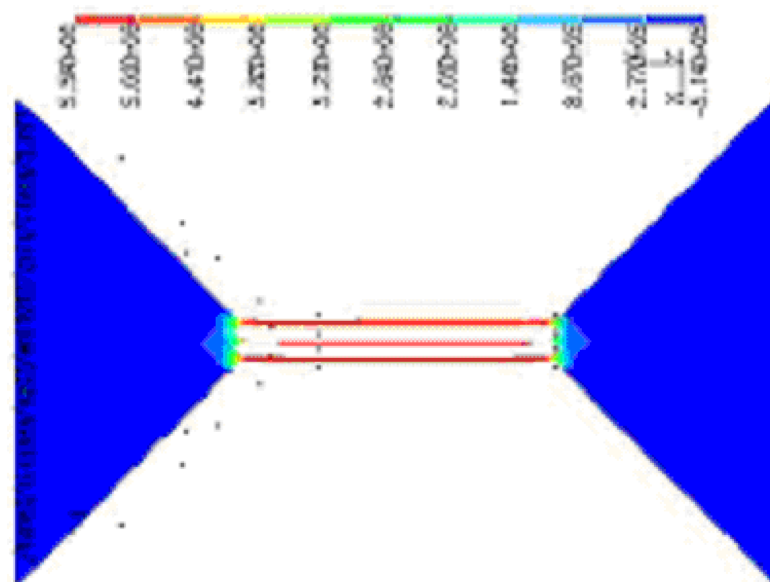

Figure 6.7: FEA simulation results of the deformation

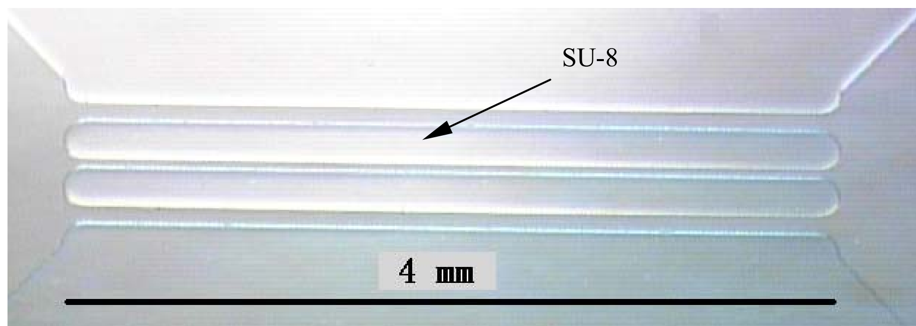

Figure 6.8: SU-8 mold with thickness 75 μm for the fabrication of the testing specimens

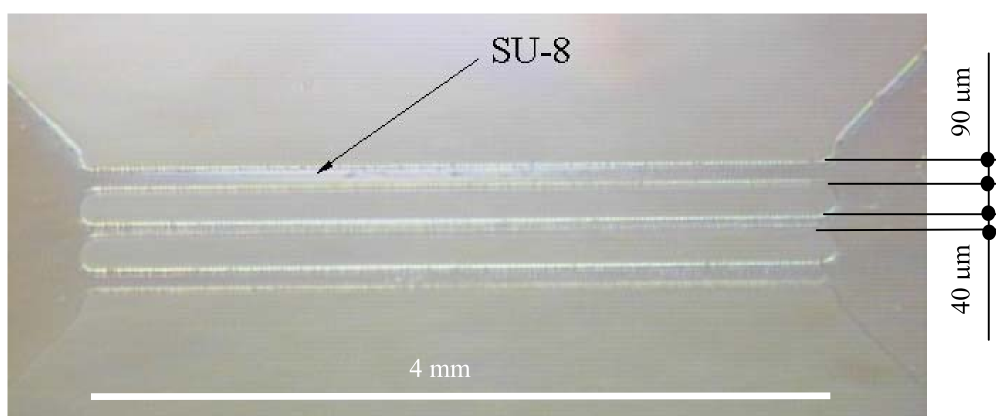

Figure 6.9: SU-8 specimen with thickness 75 μm.

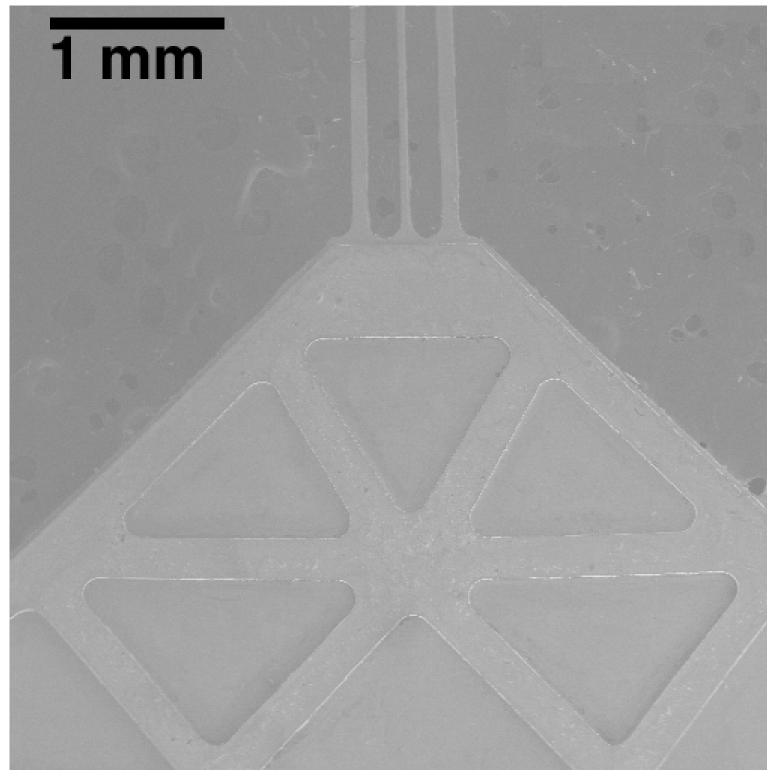

Figure 6.10: SEM picture of nickel specimen

6.6 Testing Setup

When testing, the specimen is held on the MTS Tytron 250 tester with specially designed gripers (Figure 6.11), which is aligned by the alignment guider. An axial force is used to stretch the specimen in different loading rate, which is controlled by a force mode or a displacement mode. The deformations and the axial forces are recorded automatically in data file.

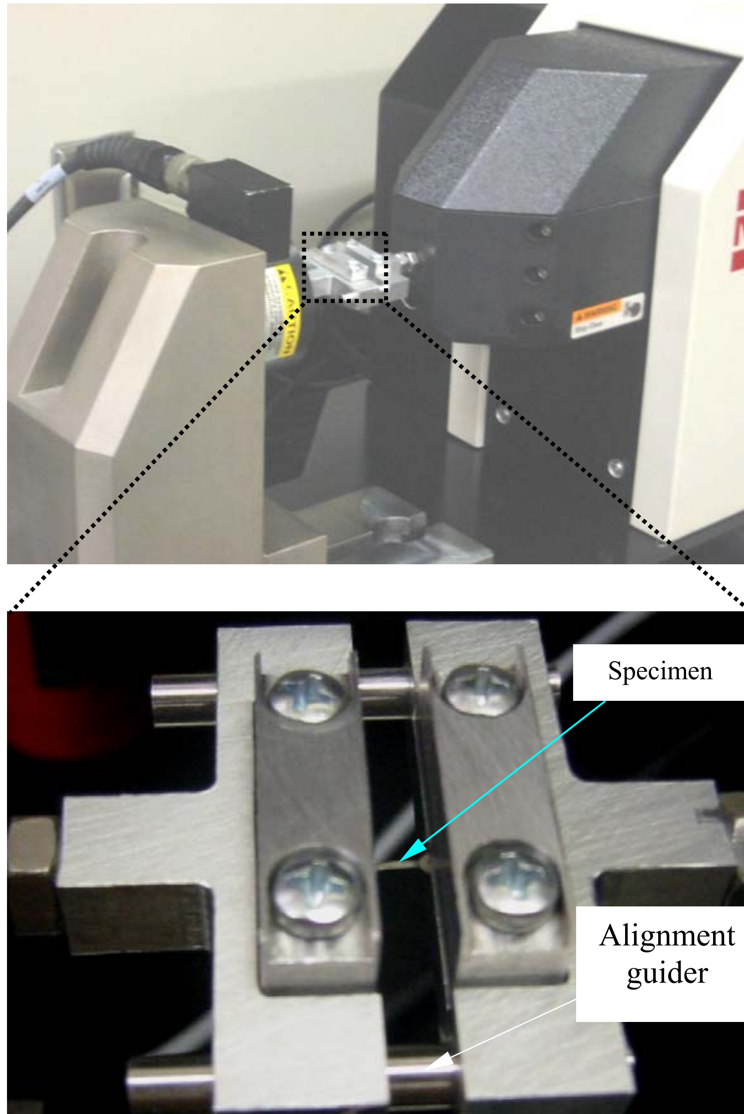

Figure 6.11: Testing system

6.7 Mechanical Testing Results

Then the stress and the strain can be calculated as follows:

$$\sigma = \frac{P}{A} \tag{6.6}$$

$$\varepsilon = \frac{\Delta L}{L} \tag{6.7}$$

where P is the applied axial force, A is the total area of the cross section of the three beams, ΔL is the total elongation of the specimen and L is the initial length of the specimen. The stress-strain graph can be plotted and the Young' smodulus and the tensile strength can be extracted.

6.7.1 Mechanical Properties of Nickel

The testing results of three nickel specimens are shown in Figure 6.12 and the fracture section is shown in Figure 6.13.Testing results of nickel show a typical metal behavior with Young' smodulus of 100 ± 10 GPa and fracture strength of 900±70 MPa. The fracture strain is found

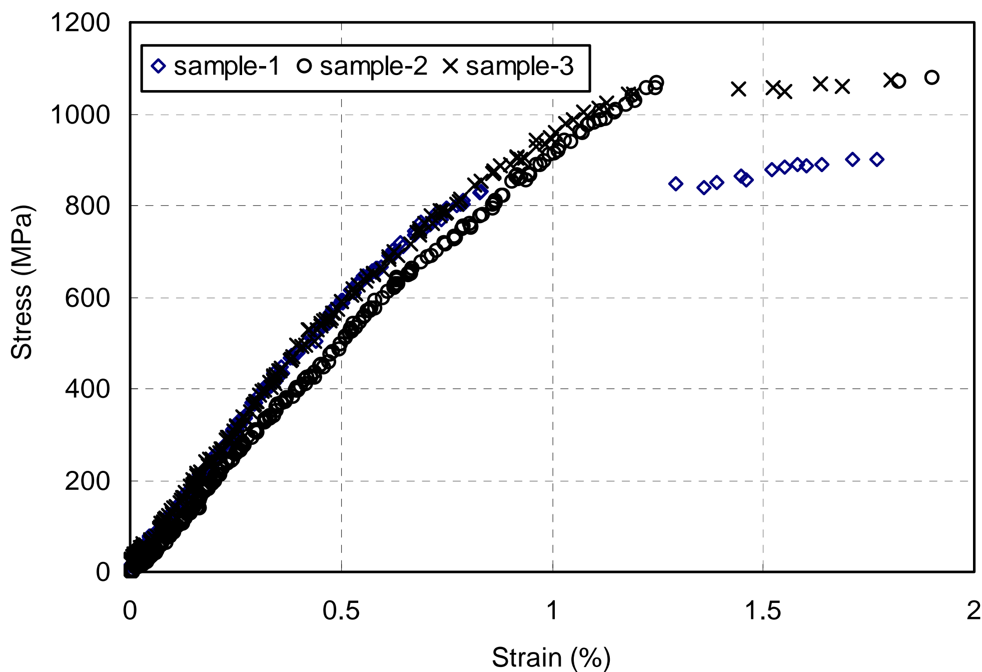

Figure 6.12: Electroformed nickel mechanical testing results

to be 1.5 ± 0.25 percent. The ultimate strength is much higher than the values from the references. This is the design of the specimen avoids any stress concentrations as well as the fabrication technique.

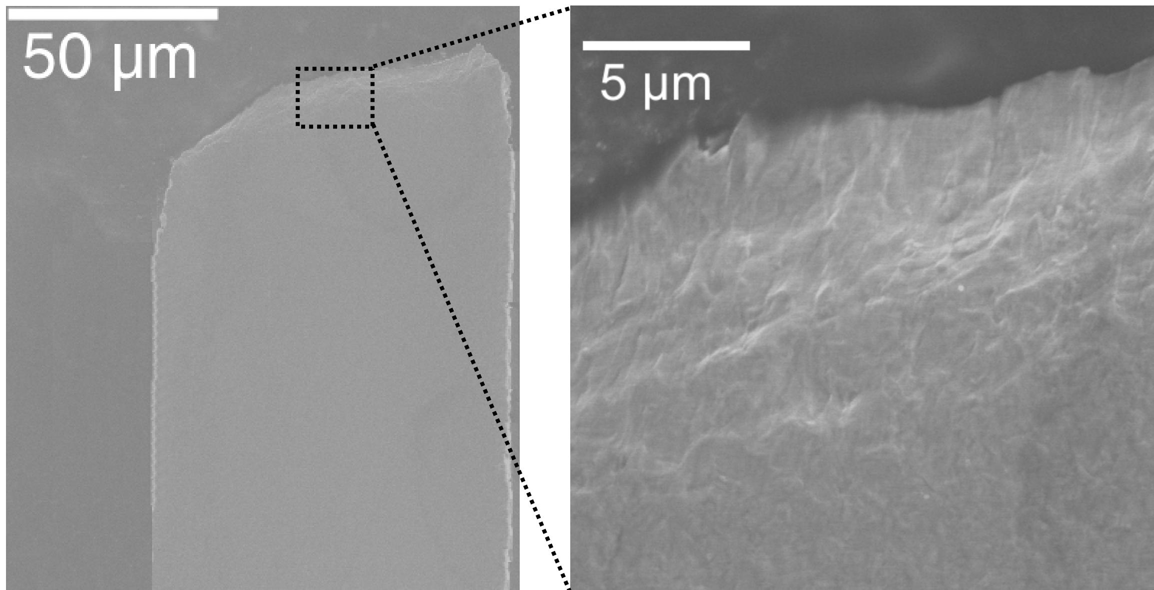

Figure 6.13: SEM picture of the fracture section of nickel specimen

6.7.2 Mechanical properties of SU-8

The testing results of three SU-8 specimens are shown in Figure 6.14 and the fracture section is shown in Figure 6.15. The testing results of the SU-8 show a brittle behavior (Figure 6.15). The average value of Young’ smodulus and fracture strength of SU-8 turn out to be 2.5±0.2 GPa and 48±3 MPa, respectively. The ultimate strength is higher than the published value of 34 Mpa form [56]. The Young’smodulus of 2.5 Gpa suggesting the specimen is more elastic due to no hard bake in the process.

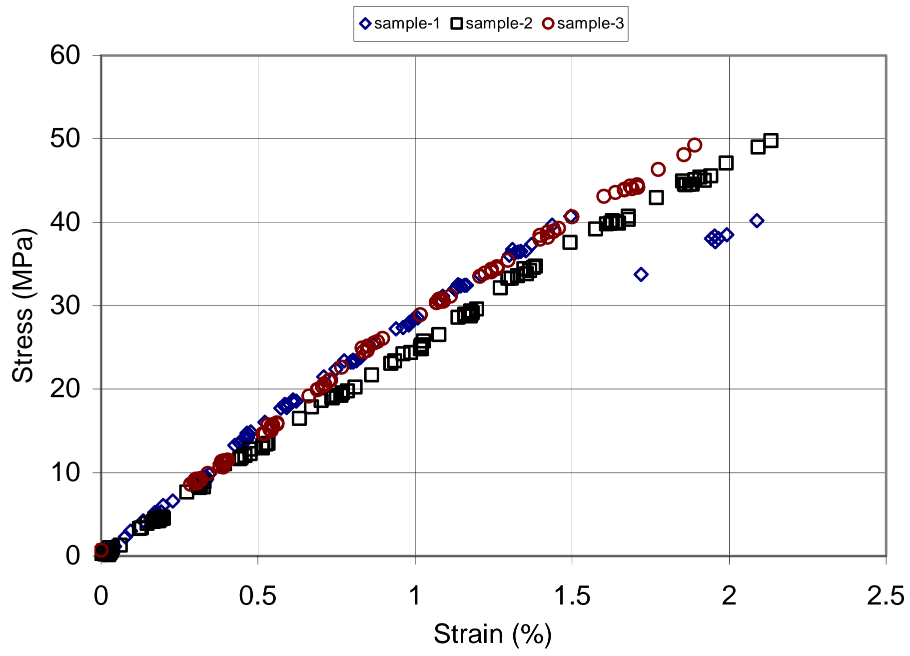

Figure 6.14: SU-8 mechanical testing results

Figure 6.15: SU-8 fracture section

6.8 Conclusion

The mechanical properties of MEMS materials are extremely important for the performance of the MEMS devices. However, people cannot borrow material properties from bulk materials to thin filmed structures because materials behave differently in micro scale. The processing methods also play an important role in the material properties. Therefore, it is necessary to develop an accurate method to measure these properties. Direct (tensile) method is favorable in its simple boundary conditions and is fully understood. For this purpose, a direct mechanical test method for MEMS materials was developed with the cooperation of a MTS Tytron Microforce Tester. The test method has advantages, in terms of direct test of micro samples with standard test frames, easy in micro sample handling with a novel aspcimen and specimen holders, in comparison to other existing direct or indirect methods. The tensile strength of electroformed nickel is about 900MPa, while tensile strength of SU-8 is about 48 MPa. The test results validate the simulation results in Chapter 2, 3, 4.

CHAPTER 7 CONCLUSIONS

UV-LIGA is an important process for the fabrication of micro devices in terms of easy access, cost effectiveness, environmental friendliness, and high precision. High aspect ratio metallic structures can be developed by using UV-LIGA process with high precision and relatively lost cost, which is critical for applications for extreme conditions such as a high-pressure environment. Conventional micro fabrication is either not capable of producing thick layers such as PVD or resulting in a bad sidewall profile such as etching where undercut (lateral etching) will occur. Although LIGA has been used to produce similar or better structures, the high cost both in equipment (such as x-Ray mask aligners) and consumables (such as masks and resists) largely limit its applications.

A low stress defects (crack) free SU-8 process was developed for the UV-LIGA process. Detailed experiments were performed to optimize processing parameters in this dissertational research. UV-LIGA is cost effective, easy in access and safe. Micro mechanical systems with high-aspect-ratio and thick metallic structures have been developed by using UV-LIGA process, and electroformed nano structured nickel and copper/SWNT composite were used as functional materials. The developed micro mechanical devices include large flow rate robust microvales, the laminated micro heat exchanger and the square-shaped copper/SWNT nano composite heat spreader.

Two types of large flow rate robust passive micro check valve arrays have been designed, fabricated and tested for robust hydraulic actuators, which are very important for space applications where payload is a critical concern.

The first set of microvalves was designed to use nano-structured nickel as the valve flap and single crystal silicon as the substrate for the inlet and outlet channels. The nickel valve flap was fabricated using UV-LIGA technology and the micro channels were fabricated using deep reactive ion etching. The fabricated microvalve weighs 0.2 gram, after packing with a novel valve stopper. Simulation showe the valve can support 10 Mpa both at open or closed state. The damped 1st mode frequency is 24.5 KHz, which makes it possible for the flap to work at 10 KHz without resonant damages. Static testing results showed a flow rate of 18 cc/s at a pressure difference of 50 psi, and the flow rate can be increased by increasing the pressure difference as indicated by Poiseuille's law. Dynamic test showed that the micro valve was able to operate at up to 14kHz. This is great advantage in comparison to traditional mechanical valves, whose operations are limited to 500 Hz or less. The advantages of micro machined valves attribute to the scaling laws.

The second set of micro mechanical valves developed is self-assembled solid metallic (nickel) valves, where both valve substrates for inlet and outlet channels and valve flap were made by electroformed nickel through UV-LIGA process. An improved nickel flap was employed in this valve to reduce the stress. Continuous multiple-stepped micro molds fabrication and molding process were conducted. Final micro mechanical valves were received after removing the micro molds trapped. There is no any additional bonding process, such as

cutting and packaging involved. Each fabrication step was aligned under microscope during the fabrication process, thus it is a highly precise self-assembled process. Testing results show the valve has a forward flow rate of 19 cc/s at a pressure difference of 90 psi and a backward flow rate of 0.023 cc/s, which is negligible (0.13%).

Nano-structured nickel has also been used to develop laminated (sandwiched) micro cryogenic heat exchanger fabricated with the UV-LIGA microfabrication process. Micro patterned SU-8 molds and electroformed nickel have been developed to realize the sandwiched heat exchanger. The SU-8 mold (200μm x 200μm x50μm) array was successfully removed after nickel electroforming. The second layer of patterned SU-8 layer (200μm x 200μm x50μm, thermal insulating layer) was patterned and aligned on top of the electroformed nickel structure to form the laminated (sandwiched) micro heat exchanger. The fabricated sandwiched structure can withstand cryogenic temperature (77K) without any damages (cracks or delaminations).

A novel copper/SWNT nano composites has been developed during this dissertational research for the heat spreading for high power electronics (HPE). The SWNTs were successfully dispersed in the copper matrix to form the SWNT/Cu metal-matrix nano composite. The tested composite density is about 7.54 g/cm^3, indicating that the SWNT volumetric fraction is 18%. SEM pictures show copper coated on SWNT (worm-shaped structure) dominates the composite surface. The measured CTE of the nanocomposite is 4.7 x 10^{-6}/°C, perfectly matching that of SiC die (3.8 x 10^{-6}/°C). The thermal conductivity obtained from Wiedemann-Franz law is 588 W/m-K, 40% better than pure copper. These properties

are extremely important for the heat spreader/exchanger to remove the heat from HPE devices (SiC dies). Meanwhile, the matched CTE will reduce the stress in the interface to prevent delaminations. Therefore, the naocomposite developed will be an excellent replacement material for the CuMo currently used in high power radar, and other HPE devices under developing.

A direct (tensile) test method was developed to test the mechanical properties of the materials involved in this research, including nickel and SU-8. Micro machined specimens were fabricated and tested on a MTS Tytron Micro Force Tester with specially designed gripers. The tested fracture strength of nanostructured nickel is 900±70 Mpa, which is much higher than published values.

In summary, the author has successfully developed a low stress and crack free SU-8 process for UV-LIGA process and a direct (tensile) testing method for the testing of mechanical properties in micro scale. Micro mechanical systems such as large flow rate micro valves, micro heat exchangers and copper/SWNT nanocomposite heat spreaders were developed using UV-LIGA process defined by SU-8 micro molds. The performance of these devices was tested and evaluated. To test the mechanical properties of the materials used in the research, micro tensile testing specimens were fabricated and characterized. The tested results validated the design and simulation results. This UV-LIGA compatible electroforming process can be easily applied to the fabrication of other MEMS devices, such as accelerometers and gyroscopes where a large mass is needed.

REFERENCES

1. Marc J. Madou, “Fundamentals of Microfabrication”, second edition
2. A. Thies, G. Shcanz, E. Walch, and J. Konys, “ Chemical Deposition of Metals for the Formation of Microstructures: An Alternative Method to Galvanoforming?”, Electrochimica Acta, Vol. 42, Nos 20-22, pp. 3033-3040, 1997
3. Wenmin Qu, Christian Wenzel, Andreas Jahn and Dieter Zeidler, “UV-LIGA: a Promising and Low-cost Variant for Microsystem Technology”
4. M. Datta a, D. Landolt, “Fundamental aspects and applications of electrochemical microfabrication”, Electrochimica Acta 45 (2000) 2535–2558
5. J. Newman, “Electrochemical Systems”, 2nd Ed., Prentice-Hall, New Jersey, 1991
6. C. Madore, M. Matlosz, and D. Landolt, J. Electrochem. Soc., 143, 3927 (1996).
7. S. Mehdizadeh, J.O. Dukovic, P.C. Andricacos, L.T., Romankiw, H.Y. Cheh, J. Electrochem. Soc., 139 (1992) 78.
8. William L. Benard, Harold Kahn, Arthur H. Heuer, and Michael A. Huff, “Thin-Film Shape-Memory Alloy Actuated Micropumps”, Journal of Microelectromechanical Systems, Vol. 7, No. 2, June 1998
9. I. Chakraboty, W.C. Tang, D.P. Bame, T.K. Tang, MEMSD micro-valve for space applications, Sensors and Actuators 83 (2000) 188-193.
10. A.P. Dorey and J.H. Moore, Advances in Actuators, Institute of Physics Publishing, 1995.

11. G. Kovacs, Micromachined Transducer Sourcebook, WCB/McGraw-Hill, New York, ISBN 0-07-116462-6, 1998.
12. Marc Madou, Fundamentals of Microfabrication, CRC Press, Boca Raton, ISBN 0-8493-0826-7, 2002.
13. W. S. Trimmer, Microrobots and Micromechanical Systems, Sensors and Actuators, vol. 19, 267-287.
14. M. Kohl, D. Dittmann, E. Quandt, B. Winzek, Thin film shape memory microvalves with adjustable operation temperatures, Sensors and Actuators A 83 (2000)214-219
15. Kazuo Hosokawa and Ryutaro Maeda, Low-cost technology for high-density microvalve arrays using polydimethylsiloxane (PDMS), IEEE International Conference of micro-electro-mechanical-systems (MEMS 2001), 531-534.
16. Koji Ikuta, Tadahiro Hasegawa and Takao Adachi, SMA micro pumps and switching valves for biochemical IC family, 2000 International Symposium on Micromechanics and Huamn Science, 169-174.
17. Jun Shinohara, Masayuki Suda, kazuyoshi Furuta, Toshihiko Sakuhara, A high pressure-resistance micropump using active and normally-closed valves, IEEE International Conference of micro-electro-mechancial-systems (MEMS 2000), 86-91.
18. Jan G. Smits, Piezoelectric micropump with microvalves, IEEE International Conference of micro-electro-mechancial-systems (MEMS 1989), 92-94.
19. Donald E. Wroblewski, MEMS micro-valve arrays for fluidic control, 1998 ASME International Mechanical Engineering Congress and Exposition, DSC-vol. 66, 145-151.

20. Krishnan Nandakumar, Allen G. Parr, Geon Hahm, Michael A. Huff, Stephen M. Phillips, A smart shape memory alloy actuated microvalve with feedback control, International Mechanical Engineering Congress and Exposition, DSC-vol. 66, 139-143.

21. W. van der Wijngaart, H. Andersson, P. Enoksson, K. Noren, and G. Stemme, The first self-priming and bi-directional valve-less diffuser micropump for both liquid and gas, IEEE International Conference of micro-electro-mechancial-systems (MEMS 2000), 674-679.

22. Harry A. Hunnicutt, Pilot operated microvalve device, US Patent 6540203

23. Quanfang Chen, Da-Jeng Yao, C-J Kim, and Greg P. Carman, "Mesoscale Actuator Device: Micro Interlocking Mechanism to Transfer Macro Load", Sensors and Actuators, vol. 73 (1999) pp.30-36.

24. P.P. Friedmann and T.A. Millott, Vibration reduction in rotorcraft using active control: a comparison of various approaches, Journal of Guidance, Control, and Dynamics, vol.18, no.4 (1995), 664-73.

25. Torben Lisby, Ole Hansen, and Jens Branebjerg "Fabrication and characterization of Flexible Silicon Substrates with Electroplated Leads" Proceedings of the IEEE Sensors conference, Orlando, FL, USA, June 2002

26. Mordechay Schlesinger, Milan Paunovc, "Modern Electroplating", fourth edition

27. Chien-Hung Ho, Kan-Ping Chin, Chii-Rong Yang, Hsien-Ming Wu, Soon-Lin Chen, Ultrathick SU-8 mold formation and removal, and its application to the fabration of LIGA-like micromotors with embedded roots, Sensors and Actuators A3533 (2002) 1-9.

28. Hyun-Kee Chang, Yong-Kweon Kim, UV-LIGA process for high aspect ratio structure using stress barrier and C-shaped etch hole, Sensors and Actuators 84 (2000) 342-350

29. H. Lorenz, M. Despont, N. Fahrni, J. Brugger, P. Vettiger, P. Renaud, High-aspect-ratio, ultrathick, negative-tone near-UV photoresist and its applications for MEMS, Sensors and actuators A 64 (1998) 33-39

30. M. Despont, H. Lorenz, N. Fahrni, J. Brugger, P. Renaud, P. Vettiger, High-aspect-ratio, ultrathick, negative-tone near-UV photoresist for MEMS applications, IEEE Microelectro Mechanical Systems Workshop, January 1997, pp. 518–522

31. M. Despont, H. Lorenz, N.Fahrni, J. Brugger. P. Renaud, and P. Vettiger, High aspect ratio ultrathick, negative-tone near-UV photoresist for MEMS applications, Proc. MEMS'97, IEEE, Nagoya, (1997), p518-522

32. H. Lorenz, M. Despont, M. Fahrni, N. LaBianca, P. Vettiger, and P. Renaud , SU-8: a low-cost negative resist for MEMS, J. Micromech. Microeng 7(1997): 121-124

33. L. Dellmann, S. Roth, C. Beuret, G. Racine, H. Lorenz, M. Despont, P. Renaud, P. Vettiger, and N. de Rooij, Fabrication process of high aspect ratio elastic structures for piezoelectric motor applications, Proc. Transducers 1997, Chicago, (1997) : 641-644

34. S. Basrour, L. Robert, X-ray characterization of residual stresses in electroplated nickel used in LIGA technique, Materials Science and Engineering A288 (2000) 270-274

35. Quanfang Chen, Bo Li, Jianwei Gong, Min Hu, Robust microvalves for hydraulic actuators, Proc. SPIE Vol. 4981, p. 18-27, MEMS Components and Applications for

Industry, Automobiles, Aerospace, and Communication II; Siegfried W. Janson; Ed., Jan 2003

36. Marco Musiani, “Electrodeposition of composites: an expanding subject inelectrochemical materials science”, Electrochimica Acta 45 (2000) 3397–3402

37. Pulickel M. Ajayan1 and Otto Z. Zhou, “Applications of Carbon Nanotubes”

38. S. Iijima, Nature 354, 56 (1991) 391

39. Kin-Tak Lau, David Hui, “the revolutionary creation of new advanced materials-carbon nanotube composites”, Composites: part B, 33, (2002) 263-277

40. S. Berber, Y.-K. Kwon, D. Tománek, ”Unusually High Thermal Conductivity of Carbon Nanotubes”, Physical Review Letters Vol. 84 Num. 20 15 may 2000, p4613

41. Hone J, Whitney M, Piskoti C and Zettl A, “Thermal conductivity of single-walled carbon nanotubes”, Physical Review Letters Vol. 59, Num. 4, 15 January 1999 R2514

42. Pulicke M. Ajayan and Otto Z. Zhou, “Applications of Carbon Nanotubes”

43. H. Ra&i-Tabar, “Computational modelling of thermo-mechanical and transportproperties of carbon nanotubes”, Physics Reports 390 (2004) 235 – 452

44. Y-K Kwon, S. Berber, D. Tomanek “Thermal contraction of carbon fullerenes and nanotubes”, Physical review letters, Vol. 92, 015901, 2004

45. Y. Maniwa, R. Fujiwara, H. Kira, H. Tou, H. Kataura, S. Suzuki, Y. Achiba, E. Nishibori, M. Takata, M. Sakata, A. Fujiwara, H. Suematsu “Thermal expansion of single-walled carbon nanotube (SWNT) bundles: X-ray diffraction studies” Physical review B, Vol. 64, 241402, 2001

46. Ph. S. Turner, “Thermal-Expansion Stresses in Reinforced Plastics”, Research Paper RP1745, Vol. 37, October 1946

47. Wei Zhang, Zhiyuan Zhu, FengWang, Tingtai Wang, Litao Sun and Zhenxia Wang, "Chirality dependence of the thermal conductivity of carbon nanotubes", Nanotechnology 15 (2004) 936–939

48. M.A. Osman, D. Srivastava "Temperature dependence of the thermal conductivity of single-wall carbon nanotubes" Nanotechnology Vol. 12 pp 21-24

49. http://eoeml-web.gtri.gatech.edu/jready/cntubes.shtml

50. Walker, J. A., Gabriel, K. J., and Mehregany, M., "Mechanical Integrity of Polysilicon Films Exposed to Hydrofluoric Acid Solutions", Jounal of Electronic Materials. 20 (1990) , pp. 665-670.

51. Johansson, S, Schweitz, J-Å, Tenerz, L and Tir´en, J. "Fracture testing of silicon microelements in-situ in a scanning electron microscope", Journal of Applied Physics. 63 (1988), pp 4799–803.

52. J.F. Burger, MC. Van der Wekken, E. Berenschot, H.J.Holland, H.J.M. ter brake, H. Rogalla, J.G.E. Gardeniers and M. Elwenspoek, "High pressure check valve for application in a miniature cryogenic sorption cooler", IEEE. 1999, p 183-188

53. W. Merlijn van Spengen, "MEMS reliability from a failure mechanisms perspective", Microelectronics Reliability 43 (2003) 1049 – 1060

54. MEMS Reliability Newsletter, VOLUME 1, NUMBER 1, SEPTEMBER 2001

55. H. Majjad, S. Basrour, P. Delobelle, M. Schmidt, "Dynamic determination of Young's modulus of electroplated nickel used in LIGA technique", Sensors and Actuators 74 1999 148–151

56. http://aveclafaux.freeservers.com/SU-8.html

57. D. Landolt, "Electrodeposition Science and Technology in the Last Quarter of the Twentieth Century", Journal of The Electrochemical Society, 149 (3) S9-S20 (2002)

58. E. Budevski, G. Staikov, W.J. Lorenz, "Electro crystallization Nucleation and growth phenomena", Electrochimica Acta 45 (2000) 2559–2574

59. Walker, J. A., Gabriel, K. J., and Mehregany, M. (1990), "Mechanical Integrity of Polysilicon Films Exposed to Hydrofluoric Acid Solutions", Jounal of Electronic Materials. 20, pp. 665-670.

60. Johansson, S, Schweitz, J-Å, Tenerz, L and Tir´en, J. (1988) "Fracture testing of silicon microelements in-situ in a scanning electron microscope", Journal of Applied Physics. 63, pp 47

61. M. Despont, H. Lorenz, N. Fahrni, J. Brugger, P. Renaud, P. Vettiger, "High-aspect-ratio, ultrathick, negative-tone near-UV photoresist for MEMS applications", IEEE Microelectro Mechanical Systems Workshop, January 1997, pp. 518–522

62. Chien-Hung Ho, Kan-Ping Chin, Chii-Rong Yang, Hsien-Ming Wu, Soon-Lin Chen, "Ultrathick SU-8 mold formation and removal, and its application to the fabrication of LIGA-like micromotors with embedded roots", Sensors and Actuators A 3533 (2002) 1–9

63. Hyun-Kee Chang), Yong-Kweon Kim, "UV-LIGA process for high aspect ratio structure using stress barrier and C-shaped etch hole", Sensors and Actuators 84 2000 342–350

64. H. Majjad, S. Basrour, P. Delobelle, M. Schmidt, "Dynamic determination of Young's modulus of electroplated nickel used in LIGA technique", Sensors and Actuators 74 1999 148–151

65. I. W. Chiang, B. E. Brinson, R. E. Smalley, J. L. Margrave, and R. H. Hauge, "Purification and Characterization of Single-Wall Carbon Nanotubes", J. Phys. Chem. B 2001, 105, 1157-1161

66. Jie Liu, Andrew G. Rinzler, Hongjie Dai, Jason H. Hafner, R. Kelley Bradley, Peter J. Boul, Adrian Lu, Terry Iverson, Konstantin Shelimov, Chad B. Huffman, Fernando Rodriguez-Macias, Young-Seok Shon, T. Randall Lee, Daniel T. Colbert, Richard E. Smalley," Fullerene Pipes", SCIENCE z VOL. 280 z 22 MAY 1998, pp. 1253-1256

67. Bo Li; Quantang Chen; Dong-Gun Lee; Woolman, J.; Carman, G.P, "Development of robust microvalves for large flow rate robust hydraulic actuators", Micro Electro Mechanical Systems, 2003. MEMS-03 Kyoto. IEEE The Sixteenth Annual International Conference on , Jan. 19-23, 2003, page(s): 96 -99

68. Quanfang Chen, Bo Li, Jianwei Gong, Min Hu, "Robust microvalves for hydraulic actuators", Proc. SPIE Vol. 4981, p. 18-27, MEMS Components and Applications for Industry, Automobiles, Aerospace, and Communication II; Siegfried W. Janson; Ed., Jan 2003

69. Jong Kuk Lim, Wan Soo Yun, Myung-han Yoon, Sun Kyung Lee,

70. Chang Hwan Kim, Kwan Kim1, Seong Keun Kim, "Selective thiolation of single-walled carbon nanotubes", Synthetic Metals (2003)

71. W.H. Safranek, The Properties of Electrodeposited Metals and Alloys, 2nd Edition, American Electroplaters and Surface Finishing Society, Orlando, FL, 1986.

72. L. Romankiw, Electrochim. Acta 42 (1997) 2985.

73. M. Datta, L.T. Romankiw, J. Electrochem. Soc. 136 (1989) 285C.

74. J. Shaw, G. Chiu (Eds.), IBM J. Res. Develop. 41, No 1:2 (January:March) 1997.

75. P. Rai-Choudhury (Ed.), Handbook of Microlithography, Micromachining and Microfabrication, vol. 2, Society of Photo-Optical Instrumentation Engineers, Bellingham, WA, 1997.
76. E. Reichmanis, The chemistry of polymers for microlithographic applications, in: C.P. Wong (Ed.), Polymers for Electronic and Photonic Applications, Academic Press, San Diego, CA, 1993.
77. S. Iwasa, K. Maeda, K. Nakano, T. Ohfuji, E. Hasegawa, J. Photopolym. Sci. Technol. 9 (1996) 447.
78. V.G. Levich, Physicochemical Hydrodynamics, Prentice Hall, Englewood Cliffs, NJ, 1962.
79. C. Kasper, Trans. Electrochem. Soc. 77 (1940) 353, 365; 78 (1940) 131, 147 ; 82 (1942) 153.
80. C. Wagner, J. Electrochem. Soc. 98 (1951) 116. [37] C.W. Tobias, R. Wijsman, J. Electrochem. Soc. 100 (10) (1953) 459.
81. M. Eisenberg, C.W. Tobias, C.R. Wilke, Chem. Engr. Progr. 51 (1955) 1.
82. J.A. Klingert, S. Lynn, C.W. Tobias, Electrochim. Acta 9 (1964) 297.
83. N. Ibl, Proc. 8th Meeting of CITCE, 1958, pp. 174.
84.
85. Adamson A W 1976 Physical Chemistry of Surfaces (New York: Wiley)
86. Wautelet M 1999 Eur. J. Phys. 20 L29
87. Andrews M, Harris I and Turner G 1993 A comparison of squeeze-film theory with measurements on a microstructure Sensors Actuators A 36 79–87

88. Andrews M, Turner G, Harris P and Harris I 1993 A resonant pressure sensor based on a squeeze film of gas, Sensors Actuators A 36 219–26

89. Sharpe, W. N., Jr., Jackson, K., Hemker, K. J. and Zie, Z. (2001) "Effect of Specimen Size on Young's Modulus and Strength of Polysilicon", Jounal of Microelectromechanical Systems, Spetember.

90. Tsuchiya T., Tabato O., Sakata J., and Taga Y. (1998), "Specimen size effect on tensile strength of surface-micromachined polycrystalline silicon thin films", Journal of Microelectromechanical Systems. pp106–113.

91. Chasiotis, I. and Knauss, W.G., (2002) "A New Microtensile Tester for the Study of MEMS Materials with the aid of AFM", Experimental Mechanics, Vo. 42, P51-57.

92. Johansson, S, Schweitz, J-Å, Tenerz, L and Tir´en, J. (1988) "Fracture testing of silicon microelements in-situ in a scanning electron microscope", Journal of Applied Physics. 63, pp 4799–803.

93. Walker, J. A., Gabriel, K. J., and Mehregany, M. (1990), "Mechanical Integrity of Polysilicon Films Exposed to Hydrofluoric Acid Solutions", Jounal of Electronic Materials. 20, pp. 665-670.

94. Petersen, K. and Guarnieri, C. (1979) "Young's modulus measurement of thin films using micromechanics", J. Appl. Phys. 50 6761–6.766

95. 5. Nix, W.D., "Mechanical Properties of Thin Films," Metallurgical Transactions, 20A, 2217–2245 (1989).

96. Weihs, T.P., Hong, S., Bravman, J.C., and Nix, W.D., "Mechanical Deflection of Cantilever Microbeams: A New Technique for Testing the Mechanical Properties of Thin Films," J. Mater. Res., 3 (5), 931–942 (1988).

97. Maier-Schneider, D., Maibach, J., and Obermeier, E., “A New Analytical Solution for the Load–Deflection of Square Membranes,” J. Microelectromech. Syst., 4 (4), 238–241 (1995).

98. De Wolf, I., “Stress Measurements in Si Microelectronics Devices using Raman Spectroscopy,” J. Raman Spectroscopy, 30, 877–883 (1999).

99. V.T. Srikar and S.M. Spearing, “A Critical Review of Microscale Mechanical Testing Methods Used in the Design of Microelectromechanical Systems”, Experimental mechanics, Vol. 43, No. 3, September 2003, p238-247

100. S.C. Tjong, Haydn Chen, “Nanocrystalline materials and coatings”, Materials Science and Engineering R 45 (2004) 1–88

101. W.H. Safranek, The Properties of Electrodeposited Metals and Alloys, 2nd Edition, American Electroplaters and Surface Finishing Society, Orlando, FL, 1986.

102. L. Romankiw, Electrochim. Acta 42 (1997) 2985.

103. M. Datta, L.T. Romankiw, J. Electrochem. Soc. 136 (1989) 285C.

104. J. Shaw, G. Chiu (Eds.), IBM J. Res. Develop. 41, No 1:2 (January:March) 1997.

105. P. Rai-Choudhury (Ed.), Handbook of Microlithography, Micromachining and Microfabrication, vol. 2, Society of Photo-Optical Instrumentation Engineers, Bellingham, WA, 1997.

106. E. Reichmanis, The chemistry of polymers for microlithographic applications, in: C.P. Wong (Ed.), Polymers for Electronic and Photonic Applications, Academic Press, San Diego, CA, 1993.

107. S. Iwasa, K. Maeda, K. Nakano, T. Ohfuji, E. Hasegawa, J. Photopolym. Sci. Technol. 9 (1996) 447.

108. V.G. Levich, Physicochemical Hydrodynamics, Prentice Hall, Englewood Cliffs, NJ, 1962.

109. C. Kasper, Trans. Electrochem. Soc. 77 (1940) 353, 365; 78 (1940) 131, 147 ; 82 (1942) 153.

110. C. Wagner, J. Electrochem. Soc. 98 (1951) 116.

111. C.W. Tobias, R. Wijsman, J. Electrochem. Soc. 100 (10) (1953) 459.

112. M. Eisenberg, C.W. Tobias, C.R. Wilke, Chem. Engr. Progr. 51 (1955) 1.

113. J.A. Klingert, S. Lynn, C.W. Tobias, Electrochim. Acta 9 (1964) 297.

114. N. Ibl, Proc. 8th Meeting of CITCE, 1958, pp. 174.

115. N. Ibl, R.H. My¨ller, J. Electrochem. Soc. 105 (1958) 346.

116. N. Ibl, Electrochim. Acta 1 (1959) 117.

117. O. Kardos, D.O. Foulke, in: P. Delahay, C.W: Tobias (Eds.), Advances in Electrochemistry and Electrochemical Engineering, vol. 2, John Wiley, New York, 1962, p. 146.

118. J. Newman, Electrochemical Systems, Prentice Hall, Englewood Cliffs, NJ, 1973, p. 431.

119. N. Ibl, in: E. Yeager, J. Bockris, B. Conway (Eds.), Comprehensive Treatise of Electrochemistry, vol. 6, Plenum Press, New York, 1982, p. 1.

120. N. Ibl, O. Dossenbach, in: E. Yeager, J. Bockris, B. Conway (Eds.), Comprehensive Treatise of Electrochemistry, vol. 6, Plenum Press, New York, 1982, p. 133.

121. R. Selman, C.W. Tobias, in: T.A. Drew (Ed.), Advances in Chemical Engineering, vol. 10, Academic Press, New York, 1978, p. 211.

122. N. Ibl, in: E. Yeager, J. Bockris, B. Conway (Eds.), Comprehensive Treatise of Electrochemistry, vol. 6,
123. Plenum Press, New York, 1982, p. 239.
124. A.C. West, J. Newman, in: B.E. Conway, J. O'M Bockris,
125. R.E. White (Eds.), Modern Aspects of Electrochemistry
126. No 23, Plenum Press, New York, 1992, p. 101.
127. S. Mehdizadeh, J.O. Dukovic, P.C. Andricacos, L.T. Romankiw, H.Y. Cheh, J. Electrochem. Soc. 139 (1992) 78.
128. A.C. West, M. Matlosz, D. Landolt, J. Electrochem. Soc. 138 (1991) 728.
129. J.O. Dukovic, IBM J. Res. Dev. 37 (1993) 125.
130. D. Landolt, Proc. Symp. Electrochem. Technology, in: L.T. Romankiw, T. Osaka (Eds.), Electronics, Electrochem. Society Inc, Princeton, NJ, 1988, p. 573.
131. A.C. West, C. Madore, M. Matlosz, D. Landolt, J. Electrochem. Soc. 139 (1992) 499.
132. R. Alkire, R. Varjian, J. Electrochem. Soc. 121 (1974) 622 124 (1977) 388.
133. M. Matlosz, P.H. Vallotton, A.C. West, D. Landolt, J. Electrochem. Soc. 139 (1992) 752.
134. R.E. White, J. Newman, J. Electroanal. Chem. 82 (1977) 173.
135. D. Landolt, Electrochim. Acta 39 (1994) 1075.
136. N. Ibl, Surf. Technol. 10 (1980) 81.
137. D. Landolt, in: N. Masuko, T. Osaka, Y. Ito (Eds.), New Trends and Approaches in Electrochemical Technology, vol. 2, Kodansha, Tokyo, 1996, p. 115.
138. J.O. Dukovic, in: H. Gerischer, C.W. Tobias (Eds.), Advances in Electrochemical Science and Engineering, vol. 3, VCH, Weinheim, 1994, p. 117.

139. S. Mehdizadeh, J. Dukovic, P.C. Andricacos, L.T. Romankiw, H.Y. Cheh, J. Electrochem. Soc. 137 (1990) 110.

140. E. Rosset, M. Datta, D. Landolt, Plat. Surf. Finish. 72 (1985) 60.

141. O. Kardos, Plating 61 (1974) 129; 229; 316.

142. S.S. Kruglikov, N.T. Kudriavtsev, G.F. Vorobiova, A. Ya. Antonov, Electrochim. Acta 10 (1965) 253.

143. S.S. Kruglikov, N.T. Kudryavtsev and R.P. Sobolev, Electrochim. Acta 12 (1967) 1263, 404. S. Iwasa, K. Maeda, K. Nakano, T. Ohfuji, and E. Hasegawa, J. Photopolym. Sci. Technol. 9 (1996) 447.

144. J. Dukovic, C.W. Tobias, J. Electrochem.

145. K. Kondo, K. Fukui, K. Uno, K Shinohara, J. Electrochem. Soc. 143 (1880) 1996.

146. K. Kondo, K. Fukui, M. Yokoyama, K. Shinihara, J. Electrochem. Soc. 144 (1997) 466.

147. K. Kondo, K. Fukui, J. Electrochem. Soc. 145 (1998) 3007.

148. P.C. Andricacos, C. Uzoh, J. Horkans, H. Deglianni, IBM J. Res. Develop. 42 (1998) 567.

149. R. Sautebin, H. Froidevaux, D. Landolt, J. Electrochem. Soc. 127 (1980) 1096.

150. C. Clerc, D. Landolt, Electrochim. Acta 32 (1987) 1435.

151. M. Matlosz, D. Landolt, J. Electrochem. Soc. 136 (1989) 919.

152. J. Deconnick, G. Magnetto, J. Vereecken, J. Electrochem. Soc. 132 (1985) 2960.

153. C. Madore, O. Piotrowski, D. Landolt, J. Electrochem. Soc. 146 (1999) 2526.

154. R.V. Shenoy, M. Datta, J. Electrochem. Soc. 143 (1996) 544.

155. R.V. Shenoy, M. Datta, L.T. Romankiw, J. Electrochem. Soc. 143 (1996) 2305.

156. F. D'Amico, M.A. DeAngelo, F.R. McLarnon, J. Electrochem. Soc. 132 (1985) 2330.

157. R. Alkire, J. Electrochem. Soc. 118 (1935) 1971.

158. R. Alkire, R. Varjian, J. Electrochem. Soc. 124 (1977) 388.

159. P.H. Vallotton, M. Matlosz, D. Landolt, J. Appl. Electrochem. 23 (1993) 927.

160. J.C. Puippe, F. Leaman (Eds.), Theory and Practice of Pulse-Plating, AESF, Orlando, FL, 1986.

161. O. Dossenbach, in: J.C. Puippe, F. Leaman (Eds.), Theory and Practice of Pulse-Plating, AESF, Orlando, FL, 1986, p. 73.

162. O. Chene, M. Datta, D. Landolt, Oberflache:Surface 26 (1985) 45.

163. H.Y. Cheh, J.Electrochem. Soc. 118 (1971) 1132.

164. K. Viswanathan, H.Y. Cheh, J. Electrochem. Soc. 126 (1979) 398.

165. H.Y. Cheh, J. Electrochem. Soc. 118 (1971) 551.

166. D-T. Chin, J. Electrochem.Soc. 103 (1983) 1657.

167. M. Datta, D. Landolt, Surf. Technol. 25 (1985) 97.

168. D. Landolt, in: J.C. Puippe, F. Leaman (Eds.), Theory and Practice of Pulseplating, AESF 1986, Orlando, FL, 1986, p. 55.

169. H.H. Wan, H.Y. Cheh, J. Electrochem. Soc. 135 (1988) 643.

170. O. Chene, D. Landolt, J. Appl. Electrochem. 19 (1989) 188.

171. A. Ruffoni, D. Landolt, Electrochim. Acta 33 (1988) 1281.

172. K.M. Jeong, K.C. Lee, H.J. Sohn, J. Electrochem. Soc. 139 (1992) 1927.

173. A.M. Pesco, H.Y. Cheh, J. Electrochem. Soc. 136 (1989) 408.

174. H.H. Wan, R.Y. Chang, W.L. Yang, J. Electrochem. Soc. 140 (1993) 1380.

175. E.K. Yung, L.T. Romankiw, R.C. Alkire, J. Electrochem. Soc. 136 (1989) 206.